The Dissertation Committee for Woochul Song Certifies that this is the approved version of the following Dissertation:

Bioinspired Membrane Design, Synthesis, and Characterization to Control Microstructure and Enable Efficient Molecular Separations

Committee:

Manish Kumar, Supervisor

Benny D. Freeman, Co-Supervisor

Gyeong S. Hwang

Nathaniel Lynd

Bioinspired Membrane Design, Synthesis, and Characterization to Control Microstructure and Enable Efficient Molecular Separations

by

Woochul Song

Dissertation

Presented to the Faculty of the Graduate School of

The University of Texas at Austin

in Partial Fulfillment

of the Requirements

for the Degree of

Doctor of Philosophy

The University of Texas at Austin

May 2021

Dedication

To my family

Acknowledgements

Looking back at my journey of earning Ph.D. degree, I was truly fortunate to make many lasting relationships with friends, colleagues, and scholars, who generously encouraged and supported my maturity as a graduate student. It has been a great journey full of moments that inspired me to make decisions be everyday choices or life-changing ones. Every person mentioned below has always guided me toward the right direction and without their valued support I would never have made it to this far and earned this rewarding degree.

First and foremost, I am greatly indebted to my "first" dissertation advisor Professor Manish Kumar. Since I first met him at Penn State as a doctoral student, Manish has wholeheartedly supported me every single day of my Ph.D. life, including the opportunity to move to UT Austin. Individually, I consider Manish as an outstanding example of a scientist as well as an educator. His advice and example have inspired me to grow as a self-standing researcher with a strong sense of collaboration. I am heartfully grateful for all the moments and memories we shared during the last five years as a supervisor-and-student, research scholars, and good friends!

I would also like to express my deepest thank to my advisor Professor Benny D. Freeman. He generously supported me during and after my transition to the University of Texas at Austin for the second half of my Ph.D. studies. His invaluable insights into my research and the clarity towards membrane research broadened my scientific perspective. I believe that the experience and opportunities I gained over the last two years under the guidance of Prof. Freeman will be priceless assets moving forward and enable me to be a

better scientist. My transition to UT Austin offered me more benefits than I ever imagined because of Prof. Freeman.

In addition to my advisors, I greatly appreciate my dissertation committee members, Professors Gyeong S. Hwang and Nathaniel Lynd at UT Austin and Professors Andrew Zydney, Xueyi Zhang, and Robert J. Hickey at Penn State. I believe that their help and guidance over the years improved the quality of research immensely.

I can tell with confidence that one of the best things that happened during my Ph.D. life was meeting Dr. Jaesung Park who is a valuable friend. I will always remember how generous he was helping me settle down in a new place and how patiently he trained me to be proficient in gas membrane research, which was an entirely new world for me when I started at UT. He absolutely amplified my research as well as my quality of life at Austin. One day, I aspire to be an amazing mentor and a friend to new researchers just like you.

I would like to thank all of current and past members of Prof. Kumar's and Prof. Freeman's research groups for their support that helped me safely finish this journey. I want to especially thank the group members and alumni who joined before me, Prof. Yue-xiao Shen, Prof. Boya Xiong, Prof. Chao Lang, Dr. Ratul Chowdhury, Dr. Hee Wook Yoon, Dr. Hasin Feroz, Dr. Tingwei Ren, Dr. Tyler Culp, and Dr. Kristopher Gleason, for setting an example with all of your successful stories and hard work. You acted as the source of inspiration that helped me set my academic goals as a graduate student. I also want to thank all the contemporaries and younger group members, Yu-Ming Tu, Laxmicharan Samineni, Brielle Hohne, Hyeonji Oh, Dr. Harekrushna Behera, Matthew Skiles, Sophie De Respino, Horacio Lopez Marques, Weiliang Bai, Aida Afica, Mekayla Depaolis, Alec Bridge, Matt Davenport, JC Davila, Mostafa Nassr, Kevin Reimund, Julian Richardson, Marshall Allen, Yu-Heng Cheng, TJ Dilenschneider, Freddy Rivers, Rahul Sujanani, William Sullivan, Edwin Torres Cuevas, and Everett Zofchak, for your

friendships and kindnesses. The support and kinship you presented me was beyond expectations. I will never forget how lucky I am to have worked in such a warm and professional environment.

I know that many parts of my dissertation work could never have been achieved without the dedication of many collaborators. In particular, I would like to thank Prof. Aleksei Aksimentiev and Dr. Himanshu Joshi for pushing the quality of our artificial water channel research to the next level, with your insightful collaboration and support with computer simulations. Also, I greatly appreciate the efforts of Prof. Stephen A. Sarles and Prof. Joseph S. Najem to study ion transport throughout our bioinspired membranes. The passionate attitude you showed me during our scientific discussions became invaluable lessons to me.

Finally, yet most importantly, I want to thank my beloved mother and father. I strongly believe that I can never express my enough gratitude to you, but I sincerely appreciate your life-long support and encouragement for my academic journey. You always have told me that you are proud of having me, but I am even more proud of having you as parents in my life. Also, Minduk and Wootak, I am truly blessed to have you as my brothers. I always feel reassured when I think of the fact that all of you will be there to support me as my family.

Abstract

Bioinspired Membrane Design, Synthesis, and Characterization to Control Microstructure and Enable Efficient Molecular Separations

Woochul Song, Ph.D.

The University of Texas at Austin, 2021

Supervisors: Manish Kumar, Benny D. Freeman

Natural resources are limited, and the failure to capture, store, and re-supply such resources can cause global economic, political, and humanitarian crises such as water scarcity. To mitigate these global risks, membrane separations have been an attractive technology due to their energy efficient and environment-friendly nature compared to other separation technologies such as distillation or chromatography. However, the development of new membranes with good separation properties and processability have been an ongoing challenge. One example is biomimetic membranes. Due to the unexpectedly fast transport and selective separation performances observed in nature, biological membrane components have been attempted for integration into scalable membranes. But maintaining the coherence of their nanoscale transport property at practice-relevant scales have been critically challenging.

Bioinspired synthetic membranes have emerged as a good alternative to help resolve these roadblocks faced by biomimetic membranes. Molecular designs of synthetic membranes components enable precise control of microstructures and improve the nanoscale homogeneity of the membranes, both of which are critical for improving

membrane separation properties, while increasing reproducibility, cost-efficiency, and processability of the membranes.

This dissertation research aims to provide scientific details needed for the developments of bioinspired membranes, spanning the broad considerations from nano- to macroscopic perspectives. First, a new type of artificial water channels (AWCs) is presented as a transport element of bioinspired membranes. A new water permeation mechanism, water-wire networks formed by these AWCs, was shown to achieve fast and selective water transport that exceeds current polymer membranes' permeability-selectivity limit. Next, a strategy of integrating such bioinspired membrane components, AWCs and amphiphilic block copolymers as transport and barrier elements respectively, into scalable membranes are studied. A series of analyses on transport experiments and computer simulations indicated a strong coherence between nanoscale and membrane scale transport properties, demonstrating successful channel integration for molecular separations. Lastly, further insights on transforming the AWC structures to viable membranes for large-scale applications are presented, specifically targeting gas separations. Leveraging these studies, this dissertation intends to provide guidance to researchers on development of new bioinspired membranes.

Table of Contents

List of Tables

List of Figures

INTRODUCTION

Separations of mixed compounds into purified forms are indispensable for modern society but are highly energy intensive processes. These processes primarily depend on thermal separations such as distillation, adsorption, and drying, which account for 10 – 15 % of global energy consumption [1, 2], and 40 – 70 % of capital and operational costs of chemical industries [3, 4]. Research into the implementation of non-thermal and sustainable separation technologies has therefore gained traction for various applications such as petroleum refining, water treatment, seawater desalination, carbon capture and storage, and other chemical and environmental processes.

Membrane-based separations are an important technology due to their high energy efficiency and low environmental footprint. Successful replacement of thermal distillation with membrane processes in the petroleum industry, for example, is expected to bring about a four-billion US$ annual cost saving and reduction of 100 million tons of CO_2 emission in the US alone [1].

Currently, primary materials for use in commercially viable molecular separation membranes are nonporous polymers such as cellulose acetate, polyimides, polyamides and their derivatives, where molecular transport occurs through diffusion between adjacent fractional free volume elements. Polymer membranes have suffered from both limited number of fractional free voids and, more importantly, the lack of rigid micro- or ultramicropore structures that limits separation properties [5]. The key to solving this problem is to design new polymer membranes with controlled and stable microstructures with good membrane processability.

Biological membranes have emerged as a prospective membrane model to address such a challenge [6]. These membranes enable molecular translocation across cellular

membranes with unexpectedly high permeability and selectivity for maintaining metabolic cycles, which have been unmatched in conventional polymer membranes. This is primarily possible due to the presence of membrane proteins that function as membrane transport elements. For example, aquaporin membrane proteins allow billions of water molecules to permeate per second, while preventing any molecules from passing through the pores [7]. In addition, the transport elements can be aligned inside the membranes with high packing density via self-assembly, which could be an ideal membrane structure for efficient molecular separations [8, 9]. However, biological components are costly to reproduce and have many uncertainties regarding direct application for practical separations. Therefore, bioinspired synthetic membrane designs could be an alternate approach to resolve this challenge [10].

Dissertation Goals and Outlines

The goal of this dissertation research is to translate the functional and structural features of biological membrane components into synthetic membrane platforms, specifically targeting aqueous separations. It consists of understanding the mechanism of water transport in aquaporin membrane proteins, implementing and engineering this mechanistic model in artificial water channels, and scaling them up for practical membrane separations. Also, further insights on the development of commercially viable gas separation membranes are provided, inspired by the molecular structures of artificial water channels.

SECTION 1 reports on a new type of artificial water channels, peptide-appended hybrid[4]arenes (PAH[4]s) [11], covering some introduction to the background and theory of water transport in biological membranes. Based on this knowledge, the proposed PAH[4] water channel was designed to provide a fast and selective transmembrane water

permeation pathway through the formation of water-wire networks within membrane matrices. This is a new mechanism that preserve the characteristic water transport feature of aquaporins but synergistically improve the permeability by cooperative intermolecular interactions. Fluorescence experiments and simulations indicate the potential of the channel-based membranes for advanced molecular separations, demonstrating that the water permeability and water-to-salt selectivity exceeds current polymer membranes' trade-off curve by a factor of ~10^4.

SECTION 2 demonstrates an integration strategy of artificial water channels into scalable membranes [12]. This method exploits the self-assembly property of the channels and membrane matrix molecules, amphiphilic block copolymers, to prepare 2D channel-polymer nanosheets with high packing density. Then, a modified layer-by-layer deposition was introduced to prepare the channel-polymer composite membranes for the separation applications. These membranes showed the preserved separation property of the channels implying successful channel integration into the membranes. Also, compared to other similarly rated commercial nanofiltration membranes, the channel-based membranes showed a sharp selectivity profile with improved permeability.

SECTION 3 expands the discussions of bioinspired membranes to large-scale applications. To simplify the structural complexity while maintaining the advantages of channel-based membranes, molecular selective filter of the artificial water channels, pillar[5]arenes, was taken into the fabrication of thin-film composite (TFC) membranes. The analysis of pure-gas transport data and materials characterization indicated that incorporating the pillar[5]arenes into TFC membranes improved molecular sieving effects. I propose that the incorporated pillar[5]arenes improved the nanoscale homogeneity of the membranes and resulted in the increased size-sieving ability. As TFC membranes are one of the most successful membrane platforms in the market, the research of this section seeks

to bridge the gaps between nanoscale transport study and commercially viable membrane development.

REFERENCES

[1] Sholl, D.S., Lively, R.P., Seven chemical separations to change the world, Nature 532 (2016) 435-437.

[2] Humphrey, J.L., Keller, G.E., Separation process technology, (1997).

[3] Marchetti, P., Jimenez Solomon, M.F., Szekely, G., Livingston, A.G., Molecular Separation with Organic Solvent Nanofiltration: A Critical Review, Chemical Reviews 114(21) (2014) 10735-10806.

[4] Adler, S., Technologies, A.I.o.C.E.C.f.W.R., Efficiency, U.S.D.o.E.O.o.E., Technologies, R.E.O.o.I., Vision 2020: 2000 Separations Roadmap, Center2000.

[5] Koros, W.J., Zhang, C., Materials for next-generation molecularly selective synthetic membranes, Nature Materials 16(3) (2017) 289-297.

[6] Shen, Y.-x., Saboe, P.O., Sines, I.T., Erbakan, M., Kumar, M., Biomimetic membranes: A review, Journal of Membrane Science 454 (2014) 359-381.

[7] Song, W., Kumar, M., Artificial water channels: toward and beyond desalination, Current Opinion in Chemical Engineering 25 (2019) 9-17.

[8] Kumar, M., Habel, J.E.O., Shen, Y.-x., Meier, W.P., Walz, T., High-Density Reconstitution of Functional Water Channels into Vesicular and Planar Block Copolymer Membranes, Journal of the American Chemical Society 134(45) (2012) 18631-18637.

[9] Song, W., Tu, Y.-M., Oh, H., Samineni, L., Kumar, M., Hierarchical Optimization of High-Performance Biomimetic and Bioinspired Membranes, Langmuir 35(3) (2019) 589-607.

[10] Song, W., Lang, C., Shen, Y.-x., Kumar, M., Design Considerations for Artificial Water Channel–Based Membranes, Annual Review of Materials Research 48(1) (2018) 57-82.

[11] Song, W., Joshi, H., Chowdhury, R., Najem, J.S., Shen, Y.-x., Lang, C., Henderson, C.B., Tu, Y.-M., Farell, M., Pitz, M.E., Maranas, C.D., Cremer, P.S., Hickey, R.J., Sarles, S.A., Hou, J.-l., Aksimentiev, A., Kumar, M., Artificial water channels enable fast and selective water permeation through water-wire networks, Nature Nanotechnology 15(1) (2020) 73-79.

[12] Shen, Y.-x., Song, W., Barden, D.R., Ren, T., Lang, C., Feroz, H., Henderson, C.B., Saboe, P.O., Tsai, D., Yan, H., Butler, P.J., Bazan, G.C., Phillip, W.A., Hickey, R.J., Cremer, P.S., Vashisth, H., Kumar, M., Achieving high permeability and enhanced selectivity for Angstrom-scale separations using artificial water channel membranes, Nature Communications 9(1) (2018) 2294.

SECTION 1: BIOINSPIRED ARTIFICIAL WATER CHANNELS[1]

Chapter 1.1: Abstract

Artificial water channels are synthetic molecules that aim to mimic the structural and functional features of biological water channels (aquaporins). This section focusses on a cluster-forming organic nanoarchitecture, peptide-appended hybrid[4]arene (PAH[4]), as a new class of artificial water channels. Fluorescence experiments and simulations demonstrated that PAH[4]s can form, through lateral diffusion, clusters in lipid membranes that provide synergistic membrane-spanning paths for a rapid and selective water permeation through water-wire networks. Quantitative transport studies revealed that PAH[4]s can transport $>10^9$ water molecules per second per channel, which is comparable to aquaporin water channels. The performance of these channels exceeds the upper bound limit of current desalination membranes by a factor of $\sim10^4$, as illustrated by the water/NaCl permeability–selectivity trade-off curve. PAH[4]'s unique properties of a high water/solute permselectivity via cooperative water-wire formation could usher in an alternative design paradigm for permeable membrane materials in separations, energy production and barrier applications.

---

[1] This section has been adapted from:
Song, W. Joshi, H. Chowdhury, R. Najem, J.S. Shen, Y.-x. Lang, C. Henderson, C.B. Tu, Y.-M. Farell, M. Pitz, M.E. Maranas, C.D. Cremer, P.S. Hickey, R.J. Sarles, S.A. Hou, J.-l. Aksimentiev, A. and Kumar, M. Artificial water channels enable fast and selective water permeation through water-wire networks *Nature Nanotechnology* 15, 73-79 (2020).

Song, W. and Kumar, M. Artificial water channels: toward and beyond desalination *Current Opinion in Chemical Engineering* 25, 9-17 (2019).

Woochul Song (W.S.) conceived and designed the research. W.S. performed the experiments of water and ion transport through the PAH[4] channels. W.S. analyzed the data. W.S. wrote the paper.

Chapter 1.2: Introduction and Background

Artificial water channels (AWCs) are transmembrane synthetic molecules that can provide rapid and selective water permeation paths spanning biomimetic membranes and attempt to mimic the function of biological water channel proteins, aquaporins (AQPs). Representative features of AQPs that highlight their potential for high-performance membrane development include (1) self-assembly property with membrane matrices that leads to properly aligned channels, and (2) single-file water permeation through channels. Cylinder-like channel structure with hydrophobic outer surfaces enables spontaneous insertion into hydrophobic compartment of biomimetic membranes and can result in highly aligned channel configurations (Figure 1A). Also, a continuous but molecularly confined water wire profile inside channels provides unexpectedly fast and selective water permeation across membranes (Figure 1B). These are desirable for high performance membrane development as they allow fast and selective molecular permeation across membranes. Motivated by the performance of transmembrane biological channel proteins, synthetic channel studies were launched a couple of decades ago but mostly focused on ion channel development as a subset of the area of synthetic supramolecular chemistry. In 2012, Barboiu observed that certain synthetic molecules could have abovementioned AQP-like features (continuous transmembrane water wire formation via self-insertion into membrane matrix) and coined the term ‘artificial water channel’ [1]. This field has grown rapidly since, with increasing interest in developing new membranes for desalination and other solute separation applications [2, 3, 4].

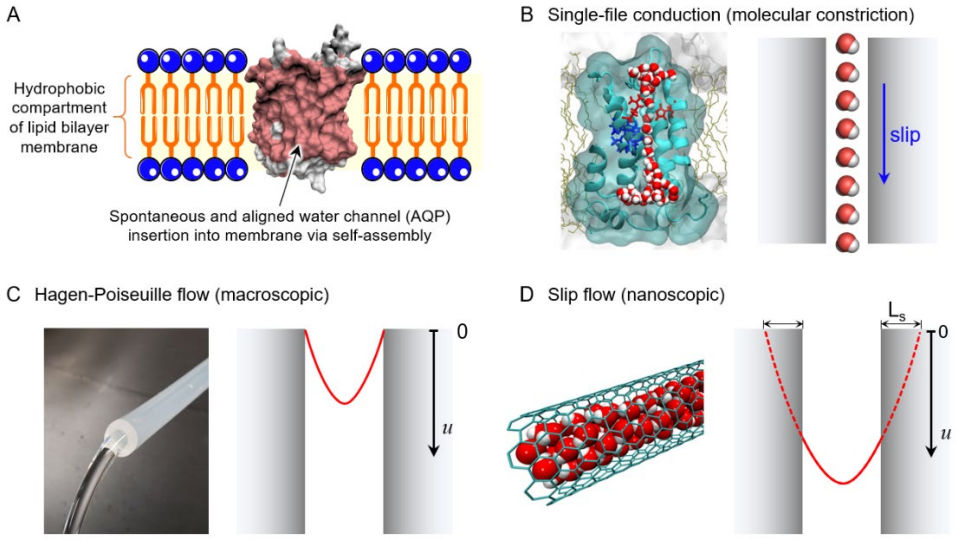

Figure 1. Schematic illustration of (A) water channel insertion into lipid bilayer biomimetic membranes via self-assembly and water permeation inside (B) water channel, (C) macroscopic, and (D) nanoscopic pores (or pipes). Left side of each panel represent examples of corresponding water flow (conduction) in (B) AQP1, (C) macroscopic tube, and (D) CNTs, respectively. Red lines represent parabolic water flow velocity (u) profiles inside pores. For nanoscopic flow that usually takes place inside nanochannels with diameters less than 100 nm such as CNT pores, frictionless flow dynamics have been illustrated using the slip-length (L_s) of velocity profiles. Inside the water channels where water molecules are confined into angstrom scale and aligned as single file configuration, continuum hydrodynamics completely breaks down (no shear flow) and water molecules permeate through via almost perfect molecular slippage along the pore lumen surfaces.

1.2.1. ARTIFICIAL WATER CHANNELS: DEFINITION AND GENERAL CONCEPTS

AQPs are biological water channel proteins that facilitate fast water transport at the rate of billions of water molecule per second (per unit osmotic driving force) with almost perfect selectivity (reported to be $>10^9$ water over monovalent ion selectivity) [5, 6]. This observation motivated the development of AQPs as a next generation desalination membrane platform starting in the last decade. Several limitations of protein channels as membrane materials, such as stability and limited processability, have resulted in

introduction of AWCs as alternatives to biological protein channels, with the goal of realizing functional features of AQPs in more tractable synthetic systems. The following subsections describe some foundational biophysical concepts that have been in focus recently and their relationship to membrane engineering.

1.2.2. Single-file water permeation

Angstrom-scale confinement of water molecules and formation of continuous single-file water wires inside channels are one of the key features that enable AQPs to achieve fast and selective water permeation [6, 7, 8]. Insights into this rapid water conduction can be obtained from consideration of slip flow of water within carbon nanotubes (CNTs, Figure 1). Since unexpectedly fast water permeation was first observed through CNT pores at the nanometer scale, slip-flow boundary conditions at the inner pore walls of CNTs have been introduced to illustrate frictionless fluid dynamics within CNTs [9, 10, 11, 12]. Slip-lengths depend on the pore radius, exponentially increasing with smaller radii under nanoscale confinement, reaching up to ~300 nm within 15 nm radius CNTs [13]. This flow behavior is also intricately related with solid surface properties of nanotubes, as exemplified recent reports on no-slip water flow inside boron nitride nanotubes (BNNT) that have equivalent physical pore configurations with same crystallography with CNTs but different combined electrochemical and pressure driven flow properties [13]. As shown in Figure 1B, at the coarse-grained level, water conduction inside AQPs takes place in a similar manner but under even more highly confined conditions; water molecules are forced into ~3 Å scale constriction regions and permeation take place through ‘almost perfect slippage of water molecules’ along inner pore surfaces of the channels in addition to several hydrogen bonding and water re-orientation steps [6, 7]. To the best of our knowledge, no single explanation has been established to describe

this permeation phenomena. However, several phenomena related to structural features have been reported to play important roles in enabling such high permeability including a hydrophobic environment [14] and hour-glass shaped pore entrance geometry [15], which contribute to enhancing permeability by reducing flow impeding-interactions between permeating waters and inner pore walls and viscous dissipation at the channel entrance, respectively.

1.2.3. Energetic correlation between low activation energy and rapid water permeation inside water channels

Rapid water permeation through water channels can be correlated with the observed low activation energy of water permeation of ~5 kcal/mol. This low activation energy is regarded as the hallmark of single-file water conduction inside nanoscale channels [16]. This value is comparable to the activation energy of self-diffusion of water (~4.2 kcal/mol) [17], reflecting that rapid water permeation is possible due to low energy barrier to transport within the channel pores.

Horner and Pohl recently proposed a relationship between activation energy of water permeation and observable water permeability of channel by invoking transition state theory. This relation utilizes the characteristic configuration of water molecules in such channels, with water molecules aligned in a molecular column and each molecule moving from one position to subsequent one by a 'hopping' mechanism (Figure 1B). This relationship is shown in Equation (1.1) [16].

$$P_f = \frac{v_0 V_w}{N_A} exp\left(\frac{-\Delta E_a}{k_B T}\right) \quad (1.1)$$

where P_f is permeability of channel ($cm^3 \cdot s^{-1}$), v_0 is the universal transition state theory attempt frequency ($\approx 10^{13}$ s^{-1}), V_w is the molar volume of water, ΔE_a is the activation energy ($kcal \cdot mol^{-1}$), k_B is the Boltzmann constant and T is the temperature (K). This energetic relationship has been shown to be well supported by experimental data on various pore-forming membrane protein channels including AQP1, AqpZ, KcsA, and Gramicidin A [16].

In a broad sense, CNT porins with a sub-nm pore diameter (~8 Å) could be considered as AWCs, since they also show favorable insertion into biomimetic membrane matrices and provide single-file water permeation paths. Tunuguntla *et al.* recently reported that these CNT porins have water permeability values of 2.3×10^{10} $H_2O \cdot s^{-1} \cdot channel^{-1}$ that exceeds AQP1's permeability by six-folds [18]. However, the activation energy of water permeation through CNT pore was observed to be at 24.1 kcal/mol and this value showed significant disagreement with Equation (1.1) by a factor of $\sim 10^{15}$. Regarding this result, Horner and Pohl have argued that the observed permeability of CNT porins may be a result of water translocation across the membranes via sliding over the outer surface of CNT walls, rather than permeation through the inner pore [16], indicating that several questions regarding flows at this scale are still unresolved. With regard to the ongoing controversy about water permeation through CNT pores, an open discussion was recently held at the Artificial Water Channels Faraday Discussions conducted under the aegis of the Royal Society of Chemistry and a detailed description of the science cited by both sides regarding this controversy was documented [19].

1.2.4. Biomimetic membrane permeability values: their origin, use, and parallels between the biophysics and membrane engineering communities

In the biophysics literature, single channel water permeabilities are frequently reported using the unit of volumetric water permeation rate ($cm^3 \cdot s^{-1}$) or number of H_2O molecules per second (e.g., ~10^9 $H_2O \cdot s^{-1}$). These values are measured under osmosis or, in membrane engineering parlance, forward or direct osmosis conditions as shown in Equation (1.2).

$$j_w = P_f \Delta C_{osm} \tag{1.2}$$

where j_w is molar flux of water ($mole \cdot s^{-1}$), P_f is osmotic permeability coefficient ($m^3 \cdot s^{-1}$), and ΔC_{osm} is molar concentration of osmolytes (in terms of $osmol \cdot m^{-3}$). Notably, osmotic permeability (P_f, $cm^3 \cdot s^{-1}$ or $H_2O \cdot s^{-1}$) is a value of water permeation rate normalized by one molar osmolyte concentration as driving force factor which is equivalent to ~25 bar or ~360 psi (a value seldom mentioned when discussing these values).

Nonetheless, in membrane-related literature, P_f value is often misunderstood as water permeation rate normalized by hydrostatic pressure (1 bar) and sometimes it has led to overestimation of water permeability of channel-based membranes, such as 1.6×10^6 $L \cdot m^{-2} \cdot hour^{-1} \cdot bar^{-1}$ (LMH/bar) assuming that membranes solely consist of AQPs [20]. To avoid this misconception, accurate evaluation should be carried out adopting the van't Hoff equation ($\Delta\pi = \Delta C_{osm} RT$) into Equation (1.2), as shown in Equations (1.3) and (1.4).

$$J_w = j_w V_w = \frac{P_f V_w}{RT} \Delta\pi \tag{1.3}$$

$$\frac{J_w}{\Delta\pi} = \frac{P_f \, v_w}{RT} \tag{1.4}$$

where J_w is volumetric water flux ($L \cdot s^{-1}$) of single channel, V_w is the molar volume of water, R is the ideal gas constant, T is the temperature (K), and $\Delta\pi$ is osmotic pressure. The left side term of Equation (1.4) describes pressure-normalized single channel water permeance ($L \cdot s^{-1} \cdot bar^{-1}$). Considering the cross-sectional channel area (e.g., ~9 nm^2 in case of AQP1), ideal channel-based membrane permeability with a unit of LMH/bar can be obtained, which is widely adopted in the synthetic membrane research field to express membrane productivity. As an example, using the historically reported osmotic permeability value of AQP1 (4.0×10^9 $H_2O \cdot s^{-1}$) [6] or the reportedly more accurate value of 1.8×10^{10} $H2O \cdot s^{-1}$ [14], ideal water permeability would be between ~35 LMH/bar and ~155 LMH/bar, which is far below than some of recently reported values [20]. For the *Rhodobacter sphaeroides* Aquaporin (RsAqpZ) that is reported to have the highest single channel permeability (~4.1×10^{10} $H_2O \cdot s^{-1}$) [21], ideal water permeability would be ~360 LMH/bar. Note that this calculation was carried out without considering any effects of operating conditions (e.g., concentration polarization) to provide theoretical permeability limits of biomimetic membranes. More relevant calculations and in-depth evaluations of AQP-based desalination membranes were recently reported by Werber and Elimelech [22].

1.2.5. ARTIFICIAL WATER CHANNEL ARCHITECTURES

Currently, AWCs are mainly classified into two types: self-assembled channels and unimolecular channels (Figure 2). Even though different synthetic strategies have been adapted to construct AWC nanoarchitectures for each type of channel, they primarily aim to achieve specific molecular configurations that have been proposed for efficient water channel development, including (1) constriction of water molecules into a single-wire

configuration through ~3 Å diameter pores for fast and selective water permeation and (2) physical (length of ~4 nm) and chemical (hydrophobic outer surface) compatibility of water channels for favorable insertion into hydrophobic compartment of lamellar membrane matrices.

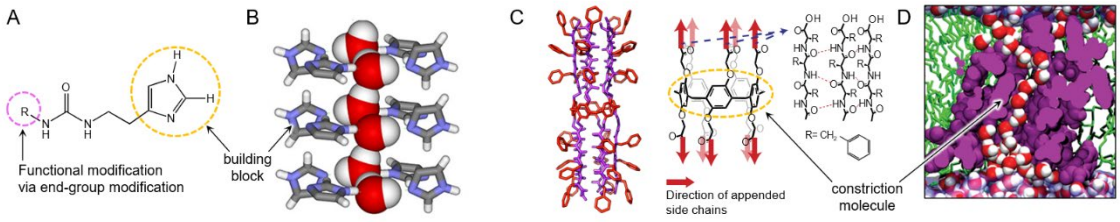

Figure 2. Structural comparison between self-assembled and unimolecular AWCs. (A) Chemical structure of representative self-assembled imidazole-quartet (I-quartet) channels. (b) Molecular modeling of columnar assembly of I-quartet channel building blocks and water molecules. Hydrogen bonds between central water molecules and building blocks are key interactions to stabilize the entire channel structures, forming continuous water wires spanning the membranes. (C) Chemical structure of representative unimolecular AWC, PAP[5]. (D) Snapshot of molecular dynamics simulation of PAP[5] inside biomimetic membrane shows the single-file water wire formation inside the channels, owing to molecularly confined inner pore environment (~5 A°).

1.2.5.1. Self-assembled channels

Self-assembled channels are based on supramolecular chemistry and utilize intermolecular organization between small organic building blocks and water molecules (Figure 2A) to construct water channel configurations [23, 24, 25, 26, 27, 28, 29, 30, 31]. They are capable of spontaneously inserting into biomimetic matrices and constructing cylinder-like columnar assemblies within the hydrophobic blocks of these matrices. Dynamically assembled structures are mainly stabilized by hydrogen bonds between building blocks and central water molecules that span the membranes (Figure 2B) and,

thereby, form continuous water wires connecting compartments (e.g., feed and permeate sides) separated by impermeable membrane matrices.

1.2.5.2. Unimolecular channels

Unimolecular channels consist of single organic macromolecules where all structural backbones are covalently linked together (Figure 2C) [32, 33, 34, 35]. They have central constriction molecules, such as pillar[n]arenes that have angstrom scale internal cavities, which act as molecularly selective filters [36]. Side chains or other supporting structural backbones are appended on these macrocycle molecule templates to achieve cylinder-like and pore-forming transmembrane nanoarchitectures (Figure 2D).

Each type of channel has pros and cons in terms of channel performance and processability, respectively (Table 1). Self-assembled channels are composed of simple structured organic building blocks that can be readily synthesized through conventional synthesis techniques, and are thus favorable for scale-up and large-scale development of channel-based membranes. However, insertion efficiency of channels into membrane matrices is relatively limited due to the precise nature of the assembly required for supramolecular organization and, even upon successful channel formation inside membranes, water permeability per channel configuration is few orders lower (~10^6 $H_2O \cdot s^{-1}$) than AQPs. This lower permeability can be attributed to the large number of hydrogen bonds between water wires and channel building blocks. In contrast, even though unimolecular channels have more complicated molecular structures which necessitates onerous synthesis processes, they have shown few orders of higher water permeability (~10^8 $H_2O \cdot s^{-1}$) than self-assembled channels bringing their performance into the permeability range of AQPs (~10^8 to 10^9 $H2O \cdot s^{-1}$). Notably, a unimolecular channel, peptide-appended pillar[5]arene, was recently integrated into full synthetic biomimetic

polymeric membranes with practical scalability and pore packing density of ~4.2 × 10^5 mm^2, of which value is two orders higher than other iso-porous membranes such as CNT-based or block copolymer (BCP) templated nanopore membranes [37].

Channels	Type	Channel permeability ($H_2O \cdot s^{-1}$)	Pore diameter (Å)	Note
Dendritic dipeptide	Self-assembled	NA	~14.5	No measurable Li^+, Na^+, and Cl^- permeation from multinuclear NMR spectroscopy. Low ion permeation rates are attributed to hydrophobic entrance effect not steric exclusion.
I-quartet		~1.5 X 10^6	~2.6	Reported to reject NaCl based on HPTS assay. Chiral water wire formation via H-bonds between water and building blocks.
Triazole		NA	~5 (average)	No water over ion selectivity property is available. Fast small cation (C^+) transport due to lubrication effect.
m-PE		NA	~6.4	No measurable Na^+ an Li^+ permeation under biased voltages.
Aquafoldamer		NA	~2.8	No water over ion selectivity property is available. Chiral and helical folding conformation.
HAP	Unimolecular	~40	~4.7	Pillar[5]arene as a central constriction molecule Hydrazide side chains Truncated water wire results in H^+ rejection.
PAP[5]		3.5 X 10^8	~4.7	Pillar[5]arene as a central constriction molecule Peptide side chains Tunable chiral selectivity via side-chain modification.
CNTPs		2.8 X 10^{10}	8	No water over ion selectivity property is available. Tunable K^+/Cl^- selectivity via pore rim modification.

Table 1. Summary of characteristic features of different AWC structures.

1.2.6. A NEW TYPE OF ARTIFICIAL WATER CHANNELS: FAST AND SELECTIVE WATER PERMEATION THROUGH WATER-WIRE NETWORKS

Insights from the wealth of structure–function relationships obtained from studies with AQPs have been used to suggest several biological channel traits as design criteria for AWCs, which include sub-nanometer unitary pore shape and a hydrophobic pore environment [2, 14]. However, achieving both AQP-like single channel water permeability and selectivity of AWCs remains a challenge that limits the development of AWC-based desalination membranes, and a new design of AWCs has been urged to be developed.

To address such a challenge, a new class of unimolecular transmembrane AWCs, peptide-appended hybrid[4]arenes (PAH[4]s) was developed. PAH[4] AWCs exhibit $>10^9$ $H_2O \cdot s^{-1} \cdot channel^{-1}$ water permeability that is comparable to AQPs (Figure 3A - D). This transport was achieved through channel cluster formation within the lipid bilayer membranes, which provided cooperatively enhanced membrane-spanning water permeation paths (Figure 3E–J). The structural design of PAH[4] originated from the attempts to synthesize AWCs with a pore size of ~3 Å (Figure 4), which is considered an ideal size for selective water permeation based on the pore geometries of AQPs. However, transport studies revealed that PAH[4]s mediated water conduction through entirely different mechanisms to those of traditional channel configurations that possess one (for example, AQPs) or less than one (for example, gramicidin A) vertical permeation path per channel molecule [38, 39]. PAH[4]s conducted water through a previously unreported mechanism owing to their unique structural and functional features (Figure 3E and F).

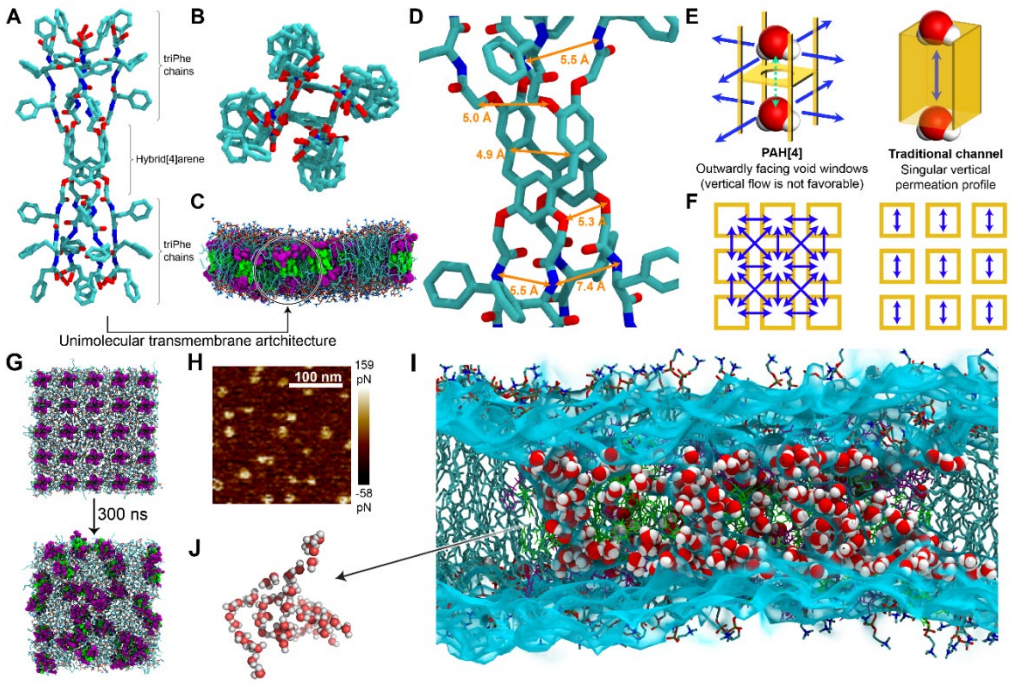

Figure 3. Cluster-forming PAH[4] channels. (A) Side and (B) top views of molecular models of PAH[4] indicate cylinder-like transmembrane structures. (C) MD simulation snapshots of PAH[4]s that span lipid bilayer membranes. (D) Tilted top view of energy-minimized PAH[4] structure shows outwardly facing void windows. Schematic comparison of the proposed water permeation paths (blue arrows) between (E) PAH[4] (left) and (F) traditional channel (right) configurations and paths through nine channel aggregates (yellow boxes), seen from the top view, for PAH[4] (left) and traditional channel (right) configurations. (G) Snapshots from an MD simulation showing lateral aggregation of PAH[4]s in lipid bilayer membrane patches. (H) The AFM image (adhesion force) of PAH[4]-reconstituted supported lipid membranes shows aggregated domains of PAH[4] channels. (I) Cross-sectional MD simulation snapshot of water permeation through a PAH[4] cluster embedded in a lipid bilayer patch, showing multiple water wires. (J) A single illustrative water-wire network (of many) connecting the water compartments across the membrane. In the MD simulation panels, molecules are represented by the colours purple and green (PAH[4]), turquoise (lipid) and red and white (water).

Chapter 1.3: Materials and Experimental Methods

1.3.1. SYNTHESIS OF PEPTIDE-APPENDED HYBRID[4]ARENE (PAH[4]) CHANNELS

PAH[4]s were synthesized in two steps: synthesis of hybrid[4]arene macrocycles followed by appending of phenylalanine tripeptide (D-Phe-L-Phe-D-Phe-COOH, triPhe) side chains on hybrid[4]arene macrocycles, respectively (Figure 4). Each step followed reported procedures which were first proposed by Boinski *et al.* [40] and Chen *et al.* [34], respectively. Hybrid[4]arenes were employed as building templates due to following structural features. First, hybrid[4]arene macromolecule has a central cavity structure with desirable size dimensions around ~3Å to ~5Å (Figure 4). Second, they have eight aromatic hydroxide reactive groups of which four face one direction (say upward) and others face downward. This bidirectional feature is important to form cylinder-like transmembrane structures when triPhe chains are extended on these reactive groups. Lastly, hybrid[4]arenes have asymmetric and slightly kinked conformation that is advantageous in terms of possibly conferring additional free void fractions in the membranes and thereby enhancing structural flexibility of PAH[4]s and water permeability. The triPhe chains were selected as a scaffold to construct cylinder-like channel backbones, based on our previous study on peptide-appended pillar[5]arene (PAP[5]), an AWC which is structurally analogous to PAH[4] (Figure 5) [37, 41]. Proton nuclear magnetic resonance spectroscopy (^{1}H-NMR) and inductively coupled plasma mass spectrometry (ICP-MS) spectra of prepared PAH[4]s are shown in Figure 6 and Figure 7, respectively.

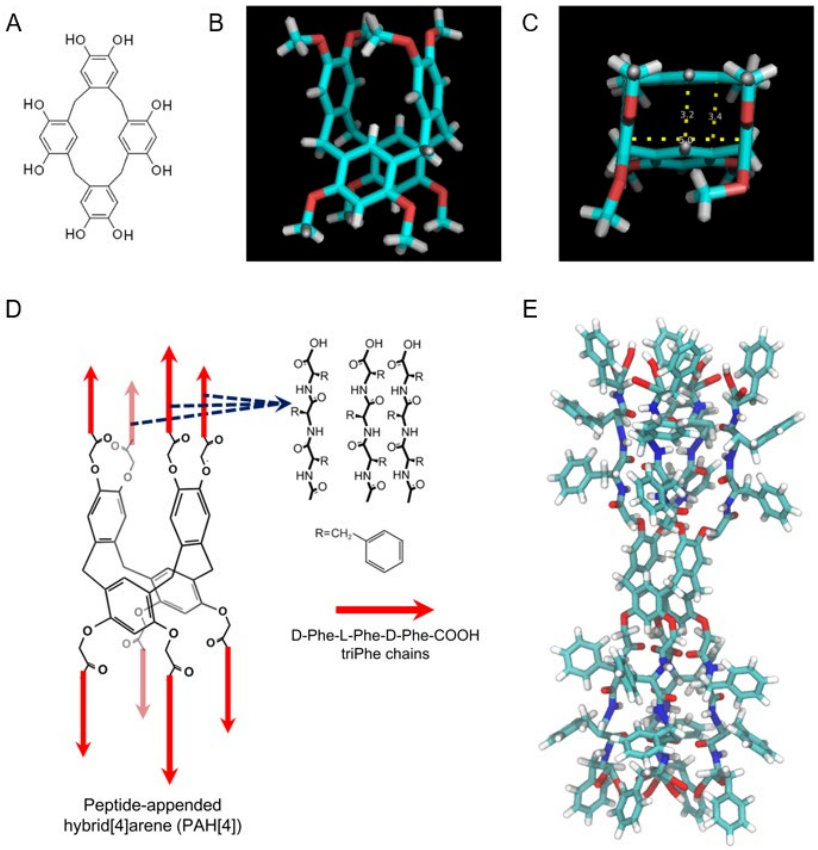

Figure 4. Molecular structure details of PAH[4] channel. (A) Chemical structure of hybrid[4]arene macrocycle molecule. (B) Crystal structure of hybrid[4]arene with methyl group substitution on hydroxide groups of hybrid[4]arenes. (C) Top-view of crystal structure of methyl-group substituted hybrid[4]arene, showing rectangular shaped central cavity with dimensions of ~3 Å × ~5 Å. (D) Schematic illustration of molecular construction strategy of PAH[4] channel. Red arrows indicate directions of extended triPhe chains on hybrid[4]arene building template. (E) Molecular modeling of prepared hybrid[4]arene channel.

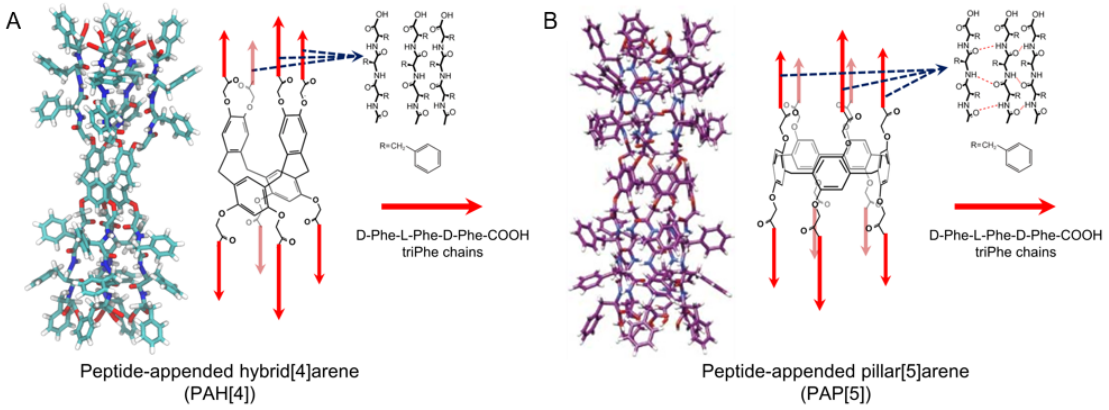

Figure 5. Structural comparison between (A) PAH[4] and (B) PAP[5] unimolecular artificial water channels. These two channels are structurally analogous except for that two different macromolecules, hybrid[4]arene and pillar[5]arene, are used as building templates for each channel, respectively. Pillar[5]arene has circular-shaped internal cavity (pore) with ~5 Å diameter which allowed both water and salt permeation . Panel (B) figure is reproduced from the reference [42].

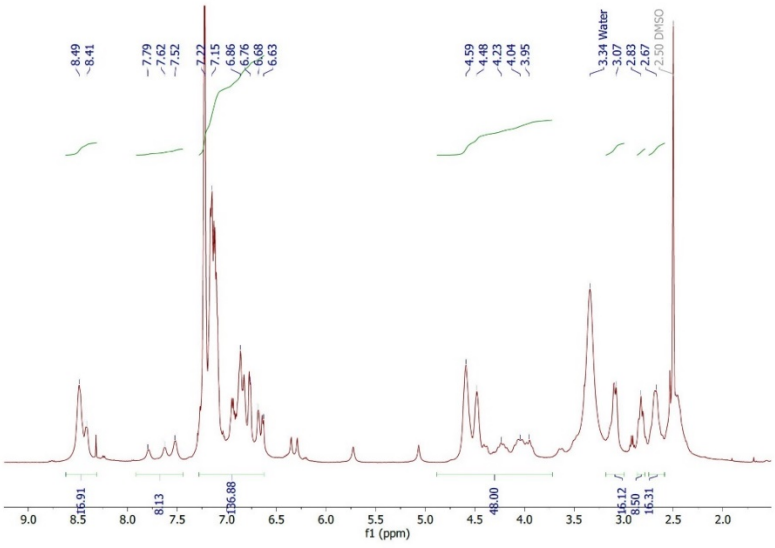

Figure 6. ^{1}H-NMR (DMSO-d_6) peaks of PAH[4]: δ 8.49-8.41 (m, 16 H), 7.79-7.52 (m, 8 H), 7.22-6.63 (m, 144 H), 4.59-3.95 (m, 48 H), 3.07 (m, 16 H), 2.83 (m, 8 H), 2.67 (m, 16 H).

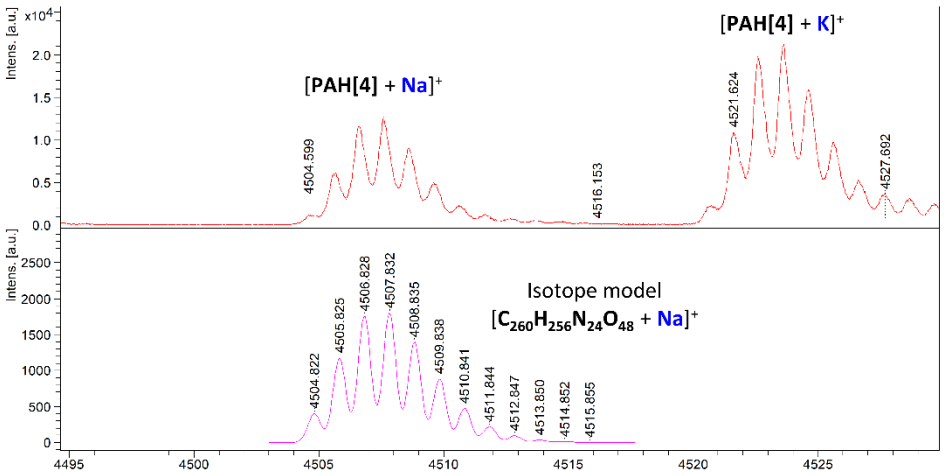

Figure 7. ICP-MS spectrum of PAH[4] channels (upper panel). Lower panel is a spectrum of PAH[4] isotope model ($C_{260}H_{256}N_{24}O_{48}$) of which peaks correspond with peaks of PAH[4] spectrum.

1.3.2. PAH[4] RECONSTITUTION INTO LIPID VESICULAR MEMBRANES

Both control lipid and PAH[4]-reconstituted lipid vesicular membranes were prepared by the film rehydration method [43]. 3 mg total of phosphatidylcholine (PC) and phosphatidylserine (PS) lipid mixture with molar ratio of 4:1 (mol/mol) was dissolved in chloroform ($CHCl_3$). Needed amounts of PAH[4]s depending on desired molar ratios of channels to lipids (mCLRs) were calculated and dissolved in lipid chloroform solutions. The solutions were transferred into 50 ml round bottomed flasks and gently dried using a rotary evaporator to form lipid films on the bottom of flasks. Any residual solvent ($CHCl_3$) was removed by placing the flasks in a high vacuum chamber for 16 hours. Completely dried films were rehydrated with 1 ml of rehydration buffer (10 mM HEPES, 100 mM PEG_{600} as osmolytes, and 0.01% (w/v) NaN_3 at pH 7.0) and extruded 15 times through 0.2

μm polycarbonate track-etched membranes to obtain uniformly sized lipid vesicles with ~200 nm diameter, which were confirmed by Zetasizer Nano-ZS90 (Malvern Panalytical).

1.3.3. WATER PERMEABILITY MEASUREMENT OF VESICULAR MEMBRANES.

Water permeability (P_f, $m \cdot s^{-1}$) of lipid vesicular membranes were measured using SF-300X stopped-flow instrument (KinTek) using a procedure extensively used in recent years for biological and artificial channel permeability measurements. Vesicles were abruptly exposed to hypotonic solution (10 mM HEPES and 0.01% (w/v) NaN_3 at pH 7.0) by mixing in the stopped flow cell. The hypotonic solution did not contain osmolytes (PEG_{600}) that were present within the vesicles and therefore imposed an inwardly directed osmotic pressure across the vesicular membranes, and the membrane permeabilities were calculated based on the amount of water influx into the vesicles driven by the osmotic gradient (Figure 8). Size change of vesicles due to water influx was monitored through side-scattering (detection angle of 90° against to incident light of 600 nm wavelength) intensity change with less than 10 milliseconds of dead-time after mixing, in order to obtain accurate kinetic information [44]. Kinetic coefficients (k) of size change of vesicles were obtained by fitting scattering traces into double-exponential functions and used to calculate osmotic permeability (P_f, $m \cdot s^{-1}$) of vesicular membranes, using the following Equation (1.5) [45].

$$P_f(m \cdot s^{-1}) = \frac{k}{(S/V_0) \times v_w \times \Delta C_{osm}} \tag{1.5}$$

where k is a larger exponential coefficient of fitted double-exponential function, S is initial surface area of vesicles, V_0 is initial volume of vesicles, v_w is the molar volume of water, and Δ_{osmol} is imposed difference of osmolarity across vesicular membranes.

Note that, for single channel permeability measurements from mCLR 0.00001 vesicles, smaller exponential coefficient (k) of fitted double-exponential function was used, because no apparent permeability increase was seen between control vesicles and mCLR 0.00001 vesicles from the first exponent. This approach was previously demonstrated and used to characterize water channels that have low water permeability [42]. Accurate ΔC_{osm} values were measured using a freezing point osmometer (Model 3300, Advanced Instruments) for all tested solutions.

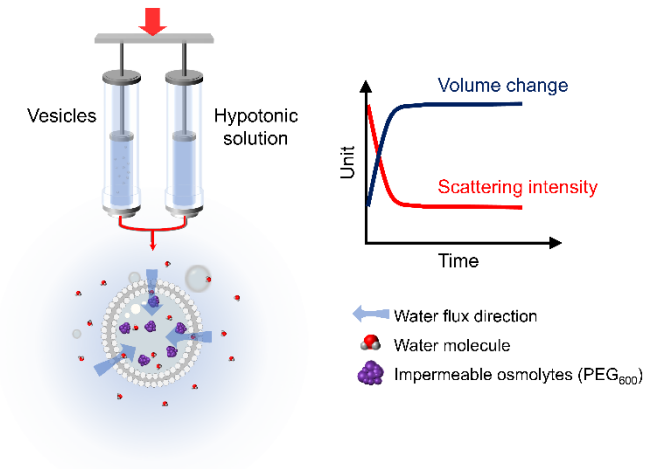

Figure 8. Schematic illustration of basic principle of measuring water permeability of vesicular membranes using stopped-flow instrument. Water influx driven by osmotic pressure induces swelling of vesicles and this kinetic information is related with membranes' permeability as described in supplementary text. The seemingly inversed trends between size change of vesicles and scattering intensity is attributed to destructive interferences of light scattering caused by several factors such as detection angle (90°) and comparable vesicle size (~200 nm) to the wavelength (600 nm) of incident light (e.g., vesicle sizes > 1/10 of the wavelength) [44].

1.3.4. FLUORESCENCE CORRELATION SPECTROSCOPY (FCS) FOR EVALUATING SINGLE PAH[4] CHANNEL WATER PERMEABILITY

To calculate single PAH[4] channel permeability, actual number of PAH[4]s embedded in reconstituted lipid vesicles was counted using fluorescence correlation spectroscopy (FCS). For FCS analysis, PAH[4]s were first labeled with (5-(and-6)-((N-(5-aminopentyl)amino)carbonyl)tetramethylrhodamine) (Invitrogen) dyes using dicyclohexylcarbodiimide (DCC) chemical cross linkers (Thermo Fisher Scientific). Molar ratio of 1:8:8 of PAH[4]s, dyes, and DCCs were dissolved in dimethyl sulfoxide (DMSO) and reacted for 16 hours by stirring at room temperature. Unreacted dyes were removed via dialysis using Slide-A-Lyzer™ MINI device (Thermo Fisher Scientific) for five days, changing fresh DMSO every 12 hours. After free dye removal by dialysis, labeled PAH[4] channels were harvested by fully evaporating DMSO solvent inside high vacuum chamber for two days, and used for both FCS and fluorescence recovery after photobleaching (FRAP) experiments. Dye-labeled PAH[4]s were reconstituted into lipid vesicles using the same film rehydration method as described earlier and the reconstituted vesicles were subsequently subjected to FCS analysis. Fluorescence intensity fluctuation of vesicles ($\delta F(t)$) in a small confocal volume was monitored using a confocal microscope equipped with a time-resolved single-photon counting module (Becker-Hickl GmbH) and autocorrelation function ($G(t)$) was obtained based on following Equation (1.6).

$$G(\tau) = \frac{\langle \delta F(t) \rangle \langle \delta F(t+\tau) \rangle}{\langle F(t) \rangle^2} \tag{1.6}$$

where t is time and τ is time lag. $G(\tau)$ is specifically related with several parameters as Equation (1.7).

$$G(\tau) = \frac{1}{N}\sum_{i=1}^{M} f_i \left[\frac{1}{1+\tau/\tau_{D_i}}\right]\left[\frac{1}{1+(r/z)^2\left(\tau/\tau_{D_i}\right)}\right]^{1/2} \quad (1.7)$$

where r and z are radius and half height of confocal volume, τ_{D_i} is lateral diffusion time of fluorescence species i, and N is total number of fluorescent species in a confocal volume which is the number of reconstituted vesicles (N_{ves}) in this case. N_{ves} could be simply obtained from y-axis intercept of autocorrelation function ($G(0) = 1/N_{ves}$). After that, vesicles were completely micellized by adding 10 % (w/v) of nonionic detergent octyl-β, D-glucoside (OG) and the number of channels (N_{chan}) were obtained using same procedure of obtaining N_{ves} (Figure 9 and Figure 10). Average number of channels per vesicles (N_{chan}/N_{ves}) was used to calculate both channel densities in lipid membranes and single channel PAH[4] permeability.

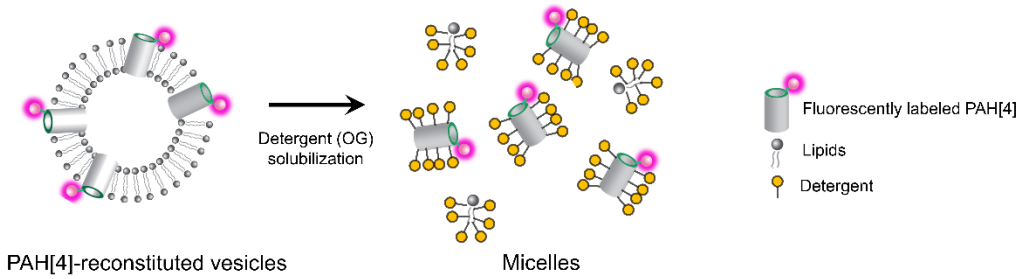

Figure 9. Schematic illustration of counting channel numbers per vesicles using FCS technique. Using FCS, the number of "fluorescent particles" in the system could be counted from the autocorrelation function. These numbers correspond with the number of reconstituted vesicles (N_{chan}) and the number of PAH[4] channels (N_{chan}), before and after detergent solubilization, respectively.

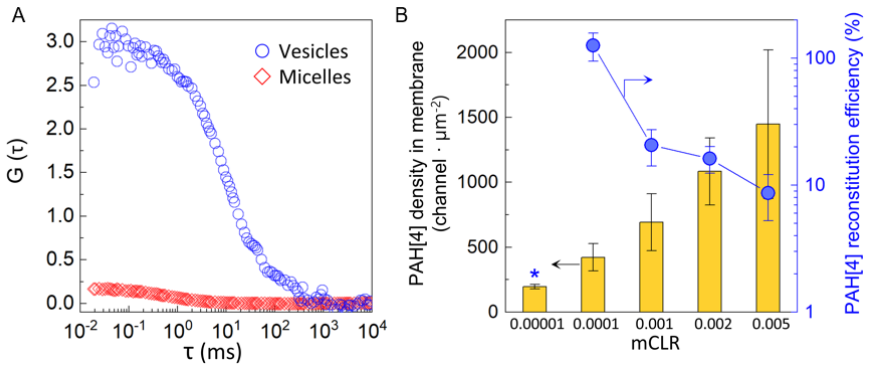

Figure 10. FCS analyses for obtaining PAH[4] channel insertion efficiency (channel density) in lipid membranes. (A) Representative autocorrelation functions, G(τ), of PAH[4]-reconstituted vesicles (mCLR 0.005) and labeled PAH[4] micelles, before (blue circles) and after (red diamonds) detergent solubilization with 2.5% OG, respectively. (B) PAH[4] channel densities in reconstituted lipid membranes (channel numbers per μm^2 membrane area) at different mCLRs. These values were used to calculate single channel water and ion permeabilities. Theoretical PAH[4] channel reconstitution efficiency was calculated and presented with blue circles. The cross sectional area of single lipid molecules was estimated as ~60 $Å^2$. *The very low number of inserted channels lead to inconsistent measurements over several cycles which are hence not shown here due to the lack of reliability of the data. This might be attributed to challenges with maintaining consistency in the lipid vesicle preparation and channel insertion process (particularly the difficulty of accounting for loss of lipid during self-assembly and extrusion steps) at low channel concentrations.

1.3.5. ATOMIC FORCE MICROSCOPY (AFM) IMAGING OF PAH[4] CLUSTERS IN SUPPORTED LIPID BILAYER MEMBRANES

AFM analyses were performed to observe PAH[4] channel clusters in lipid bilayer membranes. Control and PAH[4]-reconstituted (mCLR 0.005) PC/PS vesicles were prepared as described above with additional buffer composition of 3mM $CaCl_2$. Supported bilayer membranes were prepared by rupturing vesicles (suspending diluted vesicle solutions) on freshly cleaved mica. After 1.5 hours of incubation time, membranes were

gently washed with water and subjected to AFM imaging in liquid (water) on a Bruker BioScope Resolve AFM. These liquid AFM measurements were conducted in PeakForce tapping mode using a ScanAsyst Fluid+ tip with a spring constant of 0.7 N/m. The force used for both the control and PAH[4] channel samples was 750 pN or less, and the images contained a minimum of 384 pixels per line. The acquired images were plane-fit to the first order to account for sample tilt. Multiple line scans were utilized throughout the scan containing PAH[4] channels to determine the size of their domains. For PAH[4]-reconstituted membranes, island domains with ~30 nm diameters (in adhesion mode) were identified spreading over the entire membrane which was not seen in control lipid membranes (Figure 11).

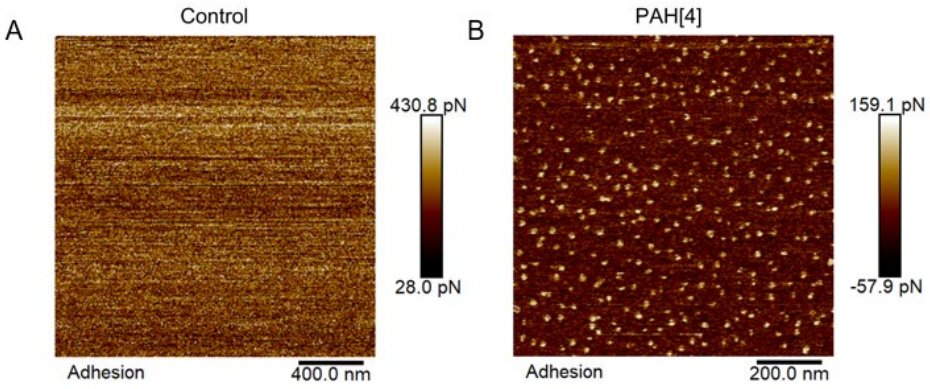

Figure 11. AFM images of (a) control and (b) PAH[4]-reconstituted supported lipid bilayer membranes on mica.

1.3.6. Fluorescence Recovery After Photobleaching (FRAP) analysis to observe lateral diffusion of PAH[4]s in lipid bilayer membranes

Two PC/PS vesicles were prepared; one is PC/PS vesicles with dye-labeled PAH[4]s (mCLR 0.005) and the other (control vesicle) is PC/PS with PAH[4]s (unlabeled, mCLR 0.005) and additional 0.5 mol% of Texas Red 1,2-Dihexadecanoly-sn-Glycero-e-

Phosphoethanolamine (TR-DHPE) lipids. TR-DHPE containing control vesicles were used to confirm bilayer formation and obtain membrane viscosity as described later. The vesicle solutions were combined with a buffer solution to create a vesicle environment with a final concentration of 2 mM $CaCl_2$, 100 mM NaCl, and 10 mM HEPES at pH 7. Supported bilayers were made by rupturing vesicles on a cleaned glass coverslip in a polydimethylsiloxane (PDMS) well. After a fusion time of 10 minutes, the formed bilayers were rinsed with buffer (100 mM NaCl, 10 mM HEPES at pH 7.0), scratched with tweezers to remove a small section of bilayer, and rinsing with the same buffer a second time. The FRAP experiments were conducted on a Nikon Eclipse TE-2000-U inverted microscope through a 10X objective lens. A 532 nm laser (Spectra Physics) was used to bleach the labeled channel or the TR-DHPE. The bleach spot diameter was approximately 16 μm. Fluorescence intensity was monitored every three seconds for the initial 75 seconds, then every 30 seconds for the remainder of the experiments (Figure 12). The fluorescent recovery curves were used to determine the diffusion coefficients of the labeled PAH[4] channel and TR-DHPE, respectively. The fluorescence intensity of the bleached spot at a given time was divided by the intensity of a non-bleached region to correct for differences in light intensity and photobleaching. The normalized fluorescence recovery, $f(t)$, was calculated using the following Equation (1.8).

$$f(t) = \frac{I_t - I_0}{I_i - I_0} \tag{1.8}$$

where I_t is the normalized spot intensity at time t, I_0 is the normalized spot intensity immediately following bleaching, and I_i is the average spot intensity prior to bleaching.

The recovery as a function of time was fit to an exponential equation to obtain the mobile fraction, A, as well as the time of half recovery, $\tau_{1/2}$, shown in Equation (1.9) and (1.10).

$$f(t) = A(1 - e^{-\tau t}) \tag{1.9}$$

$$\tau_{1/2} = \frac{\ln 2}{\tau} \tag{1.10}$$

The lateral diffusion coefficient, D_{lat}, was calculated as follows, where ω is the half-width of the Gaussian laser beam, Equation (1.11).

$$D_{lat} = \frac{0.88 \times \omega^2}{4 \times \tau_{1/2}} \tag{1.11}$$

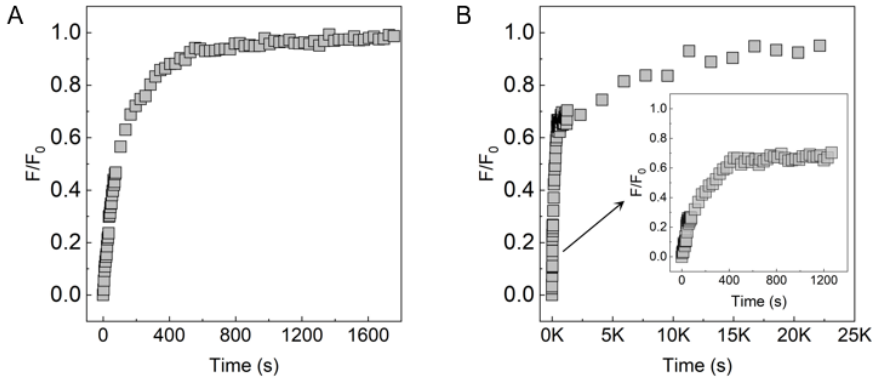

Figure 12. Representative FRAP curves for (a) TR-DHPE lipids and (b) labeled-PAH[4] embedded planar PC/PS lipid membranes.

1.3.7. MEASUREMENT OF ACTIVATION ENERGY OF WATER PERMEATION THROUGH PAH[4] CHANNELS.

Water permeability measurements of both control and channel-reconstituted lipid membranes were repeated at different temperatures (between 5 and 25 °C), in order to measure activation energy (E_a) of water permeation through channels as well as lipid membrane matrix (Figure 13). Channel-mediated water permeabilities at each temperature were obtained by subtracting control lipid membranes' permeability from channel-reconstituted membranes' permeability. Water permeability (P_f, μm·s^{-1}) and E_a of water permeation is related by the Arrhenius Equation (1.12) [5, 16, 18].

$$P_f(\mu m \cdot s^{-1}) = Ae^{\frac{-E_a}{RT}} \tag{1.12}$$

where A is pre-exponential constant, R is ideal gas constant, and T is temperature (K). E_a can be simply extracted from a slope of the Arrhenius plot as shown in Equation (1.13).

$$\ln P_f(\mu m \cdot s^{-1}) = \ln A - \frac{E_a}{R}\frac{1}{T} \tag{1.13}$$

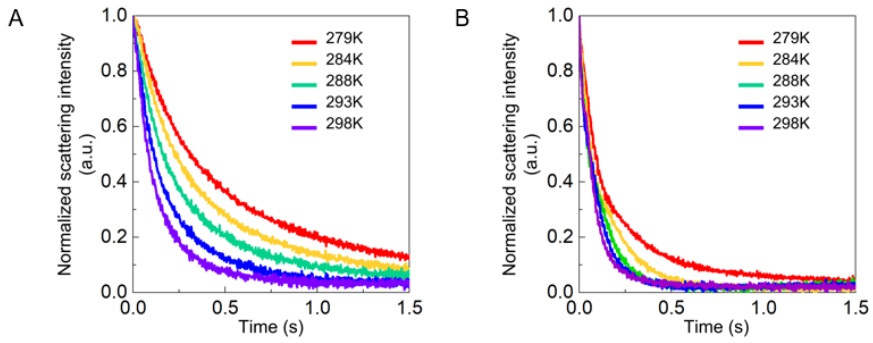

Figure 13. Stopped-flow scattering traces of (A) bare lipid vesicles and (B) PAH[4]-reconstituted vesicles (mCLR 0.002) at different temperatures (K) to calculate the activation energy of water permeation.

1.3.8. Cl^- ION PERMEABILITY MEASUREMENT

Measurements of Cl^- permeability of both control and PAH[4]-reconstituted lipid vesicular membranes were performed using stopped-flow fluorescence experiments. Excitation wavelength was set as 455 nm using a monochromator and PMT module was equipped with BrightLine® fluorescence 534/30 emission filter. Lucigenin-encapsulating vesicles prepared with Cl^- free buffer (10 mM HEPES, 100 mM KNO_3, 10 µM valinomycin and 0.01% (w/v) NaN_3 at pH 7.0) were abruptly exposed to different Cl^- gradients in the stopped-flow measurement cell (e.g., in order to impose 20 mM Cl^- gradient, same volumetric amount of Cl^- containing buffer (10 mM HEPES, 40 mM KCl, 60 mM KNO_3, 10 µM valinomycin and 0.01% (w/v) NaN_3 at pH 7.0) to vesicle solution was mixed in the measurement cell), and fluorescence intensity change was monitored. Note that potassium ionophore valinomycin was added to the vesicles beforehand to mitigate charge imbalance across the membrane, and therefore prevent underestimation of Cl^- permeability due to electrical potential developed as a consequence. Initial fluorescence kinetic information ($dF/dt|_{t=0}$) is quite important for accurate evaluation of Cl^- permeability and stopped-flow traces (Figure 14). More than 10 traces of fluorescence intensity change were recorded

for each measurement and the averaged trace was used for analysis. Vesicular membranes' mole flux of Cl^- ion (j_{Cl}) at each tested Cl^- concentration condition was calculated by Equation (1.14).

$$j_{Cl} = \frac{d(mole)}{S \times dt} = \frac{V}{S}\frac{d[Cl^-]}{dt}\Big|_{t=0} = \frac{-V}{S \times K_{sv} \times F_0}\frac{dF}{dt}\Big|_{t=0} \quad (1.14)$$

where S and V are surface area and volume of vesicles, $[Cl^-]$ is molar concentration of Cl^- ions inside vesicles, K_{sv} is the determined Stern-Volmer constant of lucigenin dyes inside vesicles (~95 M^{-1}), F_0 is fluorescence intensity under Cl^- free condition (fluorescence intensity at t = 0). Cl^- permeability coefficient (B_{Cl}, $cm \cdot s^{-1}$) of membranes was obtained from slope of j_{Cl} plot as a function of Cl^- concentration gradients, Equation (1.15).

$$B_{Cl} = \frac{dj_{Cl}}{d[Cl^-]} \quad (1.15)$$

Single PAH[4] channel Cl^- permeability coefficient ($B_{Cl,PAH}$, $cm^3 \cdot s^{-1}$) was calculated based on channel density in lipid membranes obtained from FCS analyses as shown in Equation (1.16).

$$B_{Cl,PAH} = \frac{d(j_{Cl,PAH,lipid} - j_{Cl,lipid})}{d[Cl^-]} \times \frac{1}{\sigma_{PAH}} \quad (1.16)$$

where $j_{Cl,PAH,lipid}$ is PAH-reconstituted membranes' Cl^- mole flux, $j_{Cl,lipid}$ is bare lipid membranes' Cl^- mole flux, and σ_{PAH} is number of PAH[4] channels per unit membrane area.

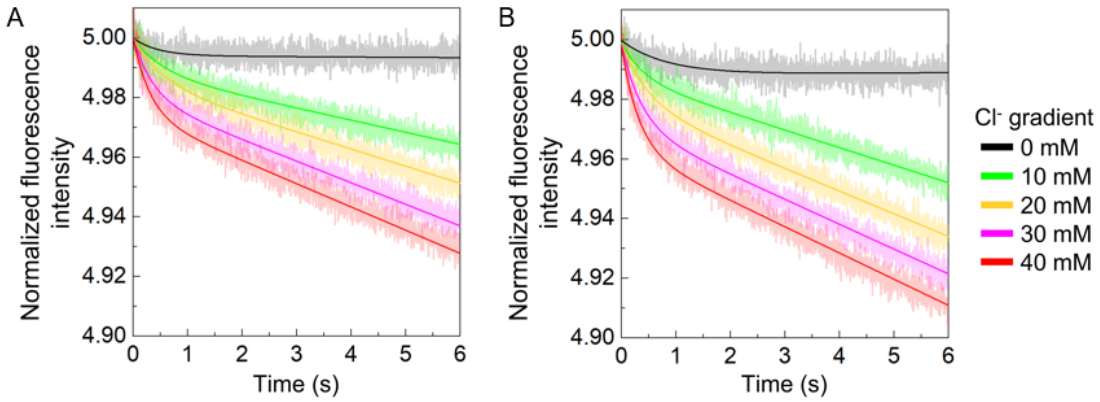

Figure 14. Representative fluorescence traces of (a) control PC/PS vesicles and (b) PAH[4]-reconstituted vesicles (mCLR 0.005) for Cl^- permeability test with lucigenin dyes. Translucent backgrounds are raw signals obtained from stopped-flow experiments and solid lines are fitted equations. Slightly enhanced Cl^- permeability (rapid quenching of fluorescence intensity due to fast Cl^- influx into vesicles) of PAH[4]-vesicles can be seen when traces are compared between control and channel vesicles.

1.3.9. 8-HYDROXYPYRENE-1,3,6-TRISULFONIC ACID (HPTS) DYE ASSAY FOR Na^+ PERMEATION TEST

HPTS dyes have been widely used to study molecular transport of ions through vesicles in a qualitative manner. Lipid vesicles were prepared with HPTS-containing rehydration buffer (10 mM HEPES, 1 mM HPTS, 100 mM NaCl, 0.01% (w/v) NaN_3 at pH 7.0). After vesicle extrusion, HPTS-encapsulating vesicles were purified using Sephadex G-50 resin columns to remove free HPTS dyes. 50 µL of vesicle solutions was rapidly mixed with 1.95 mL of buffer (10 mM HEPES, 1 mM HPTS, 100 mM NaCl, 0.01% (w/v) NaN_3 at pH 8.0) and fluoresce intensity change was monitored for five minutes using SpectraMax M5 microplate reader (Molecular Devices). After five minutes of measurements, 25 µL of 20 % (v/v) Triton X-100 was added to completely lyse lipid vesicles and release entrapped HPTS dyes into buffer solution. For PAH[4] channels,

mCLR 0.005 vesicles were used for the HPTS assay. Gramicidin A (gA), which is well known cation transport pore-forming peptide channel, was used as a positive control of cation (Na^+) transport. The same molar amount of gAs with tested PAH[4]s was dissolved in buffer before vesicle solution addition, followed by same procedure of measuring fluorescence intensity change.

1.3.10. CURRENT-TO-VOLTAGE MEASUREMENT OF PAH[4] RECONSTITUTED LIPID MEMBRANES USING DIB SYSTEM

A droplet-interface bilayer (DIB) setup was used to characterize the ionic transport properties of PAH[4] and PAP[5] channels (as a control) in lipid bilayer membranes. The lipid membranes were formed between two aqueous droplets anchored to wire-type electrodes in a transparent reservoir filled with oil, as described elsewhere [46, 47]. In brief, the setup consisted of two lipid-encased aqueous droplets hanging from silver/silver chloride (Ag/AgCl) wires (Goodfellow) in oil (1:2 mixture of hexadecane (≥ 99%, Sigma) and decane (≥ 95%, Sigma). When the droplets were brought into contact, the lipid tails from each droplet interacted with each other at the interface to expel oil and form an oil-depleted hydrophobic center (i.e., a thinned lipid bilayer). To help the droplets anchor to Ag/AgCl wires, the ball-ended tips were coated with a 1% agarose gel solution.

To confirm lipid bilayer formation, which is reflected as an increase in membrane capacitance, a 10 Hz, 10 mV triangular wave was supplied to the electrodes using a function generator (Hewlett-Packard 3314A). Due to the capacitive nature of the membrane, the resulting current response is square-like. As the area of the thinned lipid membrane grows, the peak-to-peak current amplitude increases until reaching a steady state. To generate the I-V relationships, a 0.01 Hz, 50 mV sinusoidal voltage waveform was supplied and the induced current was recorded. In parallel, to monitor the changes in

the membrane, images of the droplets from below through a 4X objective lens of an Olympus IX51 inverted microscope were acquired using a QI Click CCD. All current recordings were made using an Axopatch 200B patch clamp amplifier and Digidata 1440 data acquisition system (Molecular Devices). For all measurements, droplets and measurement probes were placed under a lab-made Faraday cage to minimize noise from the environment.

1.3.11. MOLECULAR DYNAMICS (MD) SIMULATIONS

All atom MD simulations were performed using the molecular dynamics program NAMD2 [48]. To create the atomistic model of PAH[4] molecule, eight phenylalanine tripeptides chains were added to the pdb of hybrid[4]arene molecule using the VMD software. The parameters for the non-standard hybrid[4]molecule connected with one phenylalanine peptide to each of the eight arms were generated using the CHARMM general force fields (CGenFF) webserver [49]. CHARMM36 force-field was used to describe the remaining phenylalanine side chains [50]. Twenty five PAH[4] channels were arranged in a 5 × 5 array and embedded into a 14.4 × 14.4 nm^2 patch of a pre-equilibrated POPC lipid bilayer membrane. The lipid patch was generated from the CHARMM-GUI membrane builder [51] and equilibrated for approximately 400 ns. Lipid molecules overlapping with the channels were removed. The system was then solvated with the TIP3 water [52] using the Solvate plugin of VMD. Sodium and chloride ions were added using the Autoionize plugin of VMD to produce an electrically neutral solution of 0.6 M salt concentration. The resulting system measured 14.4 × 14.4 × 10 nm^3 and contained approximately 170,000 atoms. Next, three conformations of PAH[4] dimers, namely lateral, orthogonal, and inverted, were generated each comprised of two units of single PAH[4] channels. 25 PAH[4] dimers in a regular 5 × 5 array were embedded into a 20 ×

20 nm^2 patch of pre-equilibrated POPC lipid bilayer membrane. the structure was solvated and ions were added to create a charge-neutral 0.6 M solution of NaCl in each system. The resulting system measured 20 × 20 × 10 nm^3 and contained approximately 353,000 atoms. Four such systems were created, three containing dimer arrays with different conformations and one where water molecules were placed inside an array of orthogonal PAH[4] dimers. Choosing the most conductive dimer conformation from these simulations, a pre-assembled cluster structures was created. Three different conformation of PAH[4] clusters were generated and embedded into a 14.4 × 14.4 nm^2 patch of pre-equilibrated POPC lipid bilayer membrane. Each structure was solvated by a 0.6 M NaCl solution. Each system measured 14.4 × 14.4 × 10 nm^3 and contained approximately 172,000 atoms.

The assembled systems were subjected to energy minimization using the conjugate gradient method that removed steric clashes between the solute and solvent atoms. Following the energy minimization, the systems were subjected to short equilibration at constant number of atoms (N), constant pressure (P = 1 bar) and constant temperature (T = 303 K), i.e., an *NPT* ensemble with harmonic restraints to all the non-hydrogen atoms of PAH[4] channels with respect to their initial positions (with the spring constants of 1 kcal/mol $Å^{-2}$). Subsequently, the harmonic restraints were released completely, and the system was equilibrated free of any restraints.

The initial all-atom configuration of the AQP1 system was built starting from the all-atom structure of bovine aquaporin-1, Protein Data Bank entry 1j4n [53]. The structure was embedded into a POPE lipid bilayer membrane as described in our previous study [8]. For the sake of comparison, the AQP1 system was simulated using the exactly same simulation protocols as the PAH[4] systems.

All MD simulations were performed using periodic boundary conditions and particle mesh Ewald (PME) method to calculate the long range electrostatic interactions in NAMD2 [54]. The Nose-Hoover Langevin piston [55, 56] and Langevin thermostat were used to maintain the constant pressure and temperature in the system [57]. CHARMM36 force field parameters [50, 58] described the bonded and non-bonded interactions of among PAH[4] channels, lipid bilayer membranes, water and ions along with NBFIX corrections for non-bonded interaction [59, 60, 61, 62]. A 8-10-12 Å cutoff scheme was used to calculate van der Waals and short range electrostatics forces. All simulations were performed using 1 femtosecond time steps for integrating the equation of motion. SETTLE algorithm [63] was applied to keep water molecules rigid whereas RATTLE algorithm [64] constrained all other covalent bonds involving hydrogen atoms. 300 - 400 ns equilibrium MD simulations were performed for each system which give rise to transmembrane water permeation through irregular dendritic paths in between the PAH[4] structures. The coordinates of the system were saved at the interval of 4.8 ps simulation. The analysis and post processing the simulation trajectories were performed using VMD and CPPTRAJ [48, 65]. Appendix A provides more details about the methods of structural optimization and MD simulations.

Chapter 1.4: Results and Discussions

1.4.1. Rapid water permeation via channel cluster formation

PAH[4]s were synthesized by attaching eight d-l-d phenylalanine tripeptides (triPhe) chains on hybrid[4]arene macrocycle molecules (Figure 3A and Figures 4 – 7). Hybrid[4]arenes were employed as building templates primarily due to their desirable narrow internal cavity dimensions (~3 Å × ~5 Å) for selective water permeation (Figure 4). The dynamic structure of PAH[4] within lipid bilayers, however, provided multiple

water permeation paths that were preferred more than a single permeation path that vertically penetrates through each central cavity. As seen in the energy-minimized model of the PAH[4] molecule (Figure 3D), triPhe chains are not rigidly held to each other by any specific interactions and form transient void windows that face outward with dimensions of around 5–7 Å, which are sterically and energetically more favorable for water permeation than the central pore cavity (Figure 15). This dynamic structure resulted in some interesting outcomes. When PAH[4]s clustered with each other within membranes, each void window could be interconnected with others from neighboring channels to provide cooperatively interconnected membrane-spanning paths for water permeation through water-wire networks (Figure 3E - J).

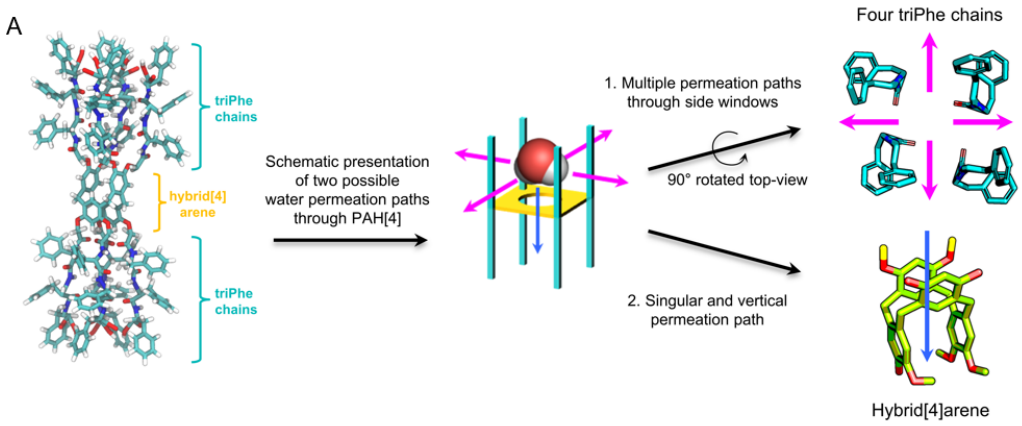

B

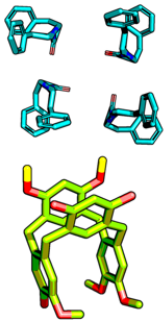

Region	Smiles ID	$\log P_{oct/wat}$
triPhe	O=C(CCc1ccccc1)N2#CC2Cc3ccccc3	3.85

Region	Smiles ID	$\log P_{oct/wat}$
Hybrid[4] arene	COc1c(O)cc2Cc3cc(c(OCC=O)cc3OCC=O)Cc4cc(c(OC)cc4Cc5cc(c(OCC=O)cc5OCC=O)Cc2c1)OC	4.99

Figure 15. Evaluation of energetically favorable water permeation paths through the PAH[4] channel. (A) Schematic presentations of two possible water permeation paths through PAH[4] channels; one is permeating through triPhe chains (magenta arrows) and the other is permeating vertically through hybrid[4]arene (blue arrow). (B) Hydrophobicity of each triPhe chains and hybrid[4]arene was evaluated using $\log P_{oct/wat}$ value; $P_{oct/wat}$ is the partition coefficient between octane and water. Lower $\log P_{oct/wat}$ value of triPhe chains indicates that triPhe chains are relatively hydrophilic compared to the hybrid[4]arene central ring. This implies that water molecules sitting inside the channel would be more favorable to pass through triPhe chains rather than hybrid[4]arene if such a path was feasible.

Water permeability of PAH[4]s in lipid bilayer membranes was investigated using stopped-flow light-scattering experiments. PAH[4]s were reconstituted into PC/PS lipid vesicles (~200 nm in diameter) with different molar ratios of channels to lipids (mCLRs) and the vesicles were exposed to outwardly directed osmotic pressure gradients (shrinking mode of the vesicles). The water efflux from vesicles driven by osmotic pressure was

evaluated by monitoring the scattering-intensity change of the vesicles, as was done in several recent studies (Figure 8) [14, 18, 42]. The rapid kinetics seen in the scattering traces indicates a faster size change of vesicles with channel incorporation and, consequently, a higher vesicular membrane permeability. The water permeability of lipid membranes increased with increasing mCLRs, which indicates that the embedded PAH[4]s enhanced the membranes' water permeation rates (Figure 16A). Single PAH[4] channel water permeability could be calculated by counting the actual number of PAH[4]s per unit membrane area obtained from fluorescence correlation spectroscopy (FCS) measurements at different mCLRs. Interestingly, PAH[4]s exhibited an enhanced single-channel permeability at higher channel densities (>~700 channels per square micrometer of lipid membrane area) and the single-channel permeability reached up to $(3.7 \pm 0.3) \times 10^9$ H2O· s^{-1}·channel^{-1} or $(1.1 \pm 0.1) \times 10^{-13}$ $cm^3 \cdot s^{-1} \cdot channel^{-1}$ at 25 °C (Figure 16B), the highest among the reported values of AWCs except for carbon nanotube porins (CNTPs) of ~8 Å diameter. These values are even comparable to that of aquaporin-1 (AQP1) (4.0×10^9 $H_2O \cdot s^{-1} \cdot channel^{-1}$) (Figure 16C). Although the most the widely adapted model was exploited to calculate water permeability of the PAH[4] channel to maintain a consistency of evaluating PAH[4] channels with published references, Pohl and co-workers recently proposed a more accurate equation to quantify water permeability [14, 66]. When this model was used for PAH[4]s, the single-channel permeability was calculated to be slightly lower at $(8.9 \pm 0.8) \times 10^8$ $H_2O \cdot s^{-1} \cdot channel^{-1}$.

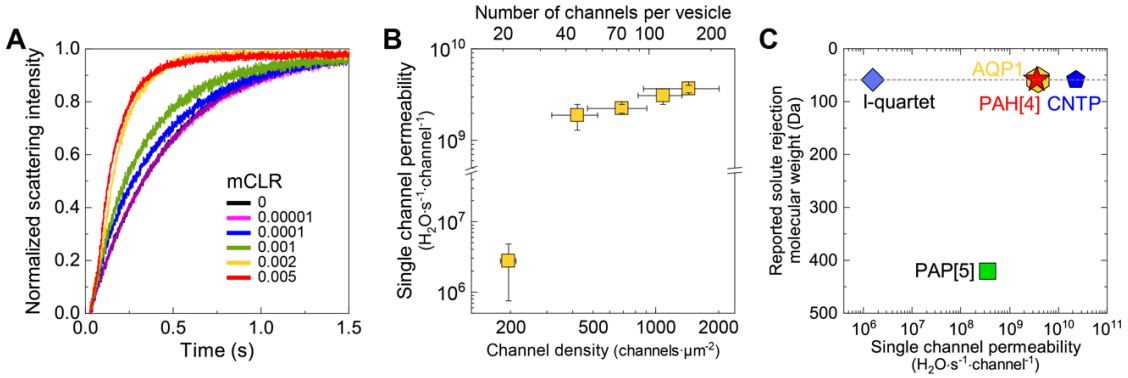

Figure 16. Measurements of water and ion conduction rates through PAH[4]s. (A) Stopped-flow light scattering traces of PAH[4]-reconstituted PC/PS vesicles with different mCLRs under an inwardly directed osmotic gradient indicate an increasing permeability with increased channel concentrations. (B) Single PAH[4] channel permeability measured at different channel densities indicates a jump in permeability when the channel concentrations reach a threshold between ~200 channels μm^{-2} (or ~20 channels per average sized vesicle) and ~420 channels μm^{-2} (or ~45 channels per vesicle), which suggests a possible cooperativity. (C) Comparison of the calculated single channel permeability and the reported effective solute rejection property of representative artificial and biological water channels: imidazole quartet (I-quartet), PAP[5], AQP1 and CNTPs.

PAH[4] clusters in the lipid bilayer membranes were observed by atomic force microscopy (AFM) performed in an aqueous buffer (Figure 17) and the domain size of the channel clusters observed from AFM experiments match well with the number of PAH[4] subunits per vesicle estimated by FCS. Further, the cluster-forming behavior of PAH[4]s in lipid bilayer membranes was confirmed via fluorescence recovery after photobleaching (FRAP) experiments (Figure 12) and molecular dynamics (MD) simulations (Figure 3G). These results are similar to our recent study that demonstrated the aggregation behavior of another triPhe chain-based unimolecular AWC, PAP[5]. Combined with the increased single-channel permeability observed with increasing channel densities in the low

membrane concentration range (Figure 16B), these results indicate a cooperatively enhanced water permeation via channel cluster formation.

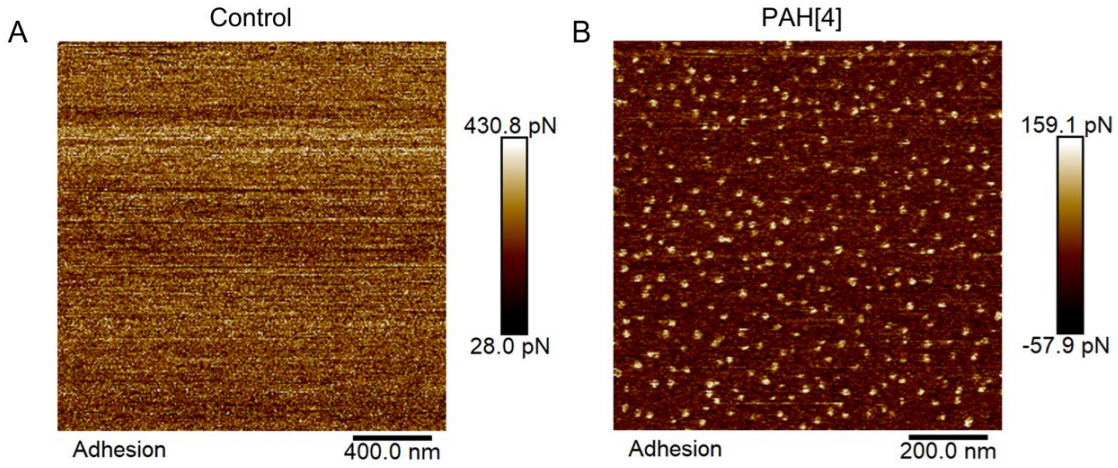

Figure 17. AFM images of (A) control and (B) PAH[4]-reconstituted supported lipid bilayer membranes on mica. The average PAH[4] domain diameter was observed to be 19.6 ± 3.2 nm with an average cluster area of 301 ± 8 nm^2. Considering the cross-sectional area of each PAH[4] monomer to be about ~2 nm^2 (from MD simulations), each cluster domain consists of 150 ± 4 PAH[4] monomers.

1.4.2. ACTIVATION ENERGY OF WATER PERMEATION THROUGH PAH[4] CLUSTERS

The measured single-channel permeability indicated that PAH[4]s can mediate water transport as efficiently as AQP1. This was further confirmed by measurement of the activation energy of water permeation through the channels (Figure 18). Control lipid membranes were shown to have an activation energy of 11.1 ± 0.8 kcal · mol^{-1} for water permeation, which corresponds to reported reference values of lipid bilayers in which water permeation takes place through the solution-diffusion mechanism [5, 45]. The activation energy for PAH[4]-mediated water permeation was measured as 3.6 ± 1.2 kcal $mol \cdot ^{-1}$, which indicates a lower energy barrier for water permeation across the membranes by

PAH[4] insertion. This low activation energy (<5 kcal · mol^{-1}) is strong evidence of single-file water transport [16]. Based on the measured activation energy and the presumption of single-file water conduction, the permeability was calculated as 6.9×10^{-13} cm^3 · channel^{-1}, which is in good agreement with the measured single PAH[4] permeability. This confirms the single-file water permeation through PAH[4] architectures across the membranes [16], which is also validated by our MD simulation results.

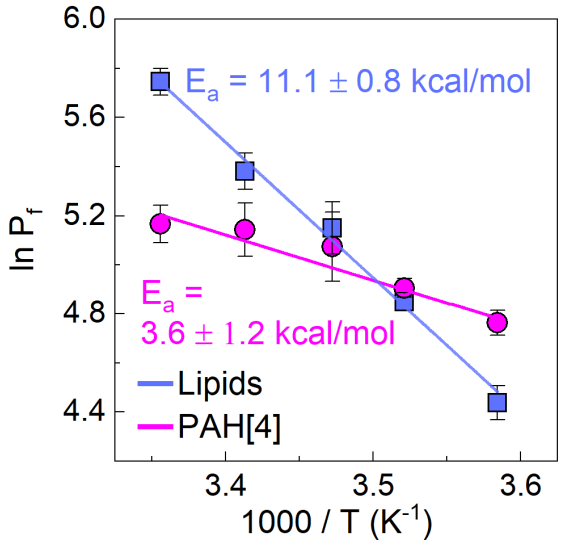

Figure 18. Arrhenius plots of the osmotic permeability (P_f (μm · s^{-1})) for the bare lipid membranes and the PAH[4]-mediated membrane permeability.

1.4.3. Quantitative Measurement of Monovalent Ion Permeability

As mentioned above, to achieve both a high permeability and selectivity is a significant challenge for membrane systems in general and AWC systems in particular—the other challenge is methodological. The water-over-ion selectivity properties of all the AWCs reported so far have been obtained using qualitative techniques rather than numerical values, such as number ratios between permeating water and ion molecules,

which represent intrinsic molecular transport properties [4]. This challenge was also recently discussed for desalination membranes and, to provide a baseline for membrane material development efforts, Park and co-workers reported an upper-bound plot of the intrinsic water/NaCl permeability–selectivity trade-off for representative polymeric desalination membranes [67]. Therefore, it is important to obtain the intrinsic transport properties of the channels is quite important to achieve coherence in terms of evaluating AWCs for any future applications, including desalination.

A combination of colloidal quenching halide ion sensitive dyes (lucigenin dyes), stopped-flow fluorescence spectrometry and FCS techniques was exploited to evaluate the quantitative PAH[4] channel chloride (Cl^-) permeability (Figure 19). Cl^- ion fluxes were measured at different Cl^- concentration gradients for both the control and PAH[4]-reconstituted membranes (Figure 19B) and the Cl− permeability coefficient of lipid membranes was measured as $(8.6 \pm 1.9) \times 10^{-10}$ cm s^{-1}, which corresponds to the reported Cl^- permeability coefficients of lipid bilayers (10^{-8} – 10^{-11} cm · s^{-1}) [68]. The single PAH[4] Cl^- permeability was calculated using channel numbers per membrane area, obtained from the FCS analysis to be $(9.5 \pm 3.6) \times 10^{-23}$ $cm^3 \cdot s^{-1}$. The channel area (~2 nm^2) normalized Cl^- permeability coefficient was $(4.7 \pm 1.7) \times 10^{-9}$ cm · s^{-1}, which is about fivefold higher than that of highly retentive lipid membranes. When combined with a water permeability of (($(3.6 \pm 0.3) \times 10^9$ H2O · s^{-1} · $channel^{-1}$ or $(1.1 \pm 0.1) \times 10^{-13}$ $cm^3 \cdot s^{-1}$)), PAH[4] exhibited an ~10^9 water/salt selectivity that far surpasses the selectivity requirements (~16,000) for desalination membranes [20].

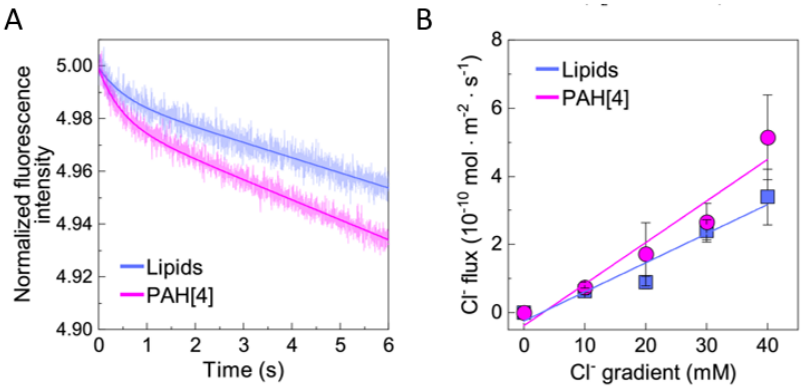

Figure 19. (A) Comparison of fluorescence intensity traces between the control and PAH[4]-reconstituted (mCLR 0.005) lipid vesicles that encapsulate lucigenin, measured in the presence of a 20 mM Cl^- concentration gradient. (B) Plots of Cl^- flux as a function of Cl^- concentration (mM) gradients for both control and PAH[4]-reconstituted lipid membranes.

The absence of suitably sensitive cation colloidal quenching dyes makes it difficult to measure the single-channel Na^+ permeability. As an alternative, an assay based on 8-hydroxypyrene-1,3,6-trisulfonic acid dye was performed to observe if any effective Na^+ permeation occurs through PAH[4]s, as this method has been widely adopted to test ion permeation through various ion channels [69], but no detectable Na^+ permeation was observed for PAH[4]-reconstituted membranes (Figure 20).

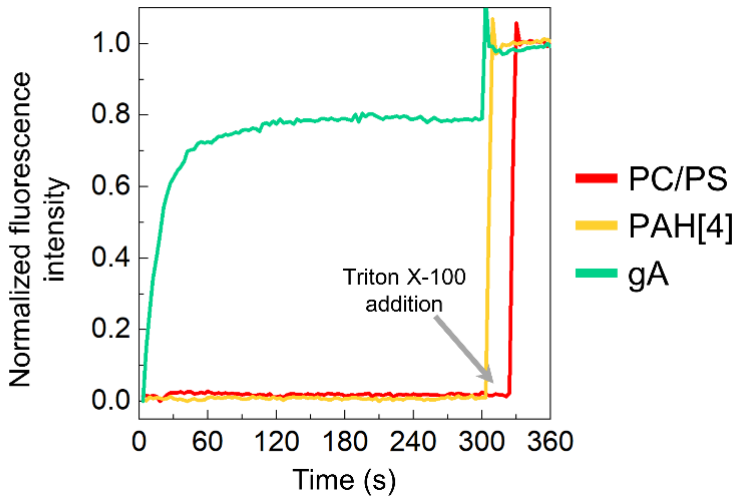

Figure 20. Representative traces of fluorescence intensity changes of HPTS dyes encapsulated in lipid vesicles, after vesicles were exposed to lower proton concentration environment (higher pH). No significant fluorescence intensity change is shown for both control (PC/PS) and PAH[4]-reconstituted (mCLR 0.005) vesicles, indicating that PAH[4]-vesicular membranes can reject Na^+ ions as efficiently as control lipid membranes. As a positive control, gA, which is well known as a cation transporting peptide, was tested as a positive control. Vesicles with gA showed fast increase fluorescence intensity. This is attributed to that Na^+ permeation through vesicular membranes that mitigates cationic electrostatic imbalance between inside and outside of vesicles and allow faster diffusion of H^+ from inside to outside of vesicles, resulting in enhanced fluorescence intensity of H^+-sensitive HPTS dyes.

Ionic current measurements across PAH[4]-reconstituted lipid bilayers were performed to demonstrate the highly retentive ion permeation properties of PAH[4]s, using a droplet interface bilayer (DIB) system [47]. The DIB system exploits PAH[4]-reconstituted PC/PC vesicles, which were confirmed to have PAH[4]s embedded in membranes from the stopped-flow experiments, to form bilayers at the interface of two droplets and, thereby, maximize the opportunity of PAH[4] presence in the DIB membranes during the ionic current measurements (Figure 21A). During the course of the current–voltage (*I–V*) measurements, PAH[4]-reconstituted membranes did not show any

ionic current at any tested conditions and the resistance value of the membranes (R_m, ~5 GΩ) was equivalent to that of the control insulating lipid bilayer membranes [22, 47], which demonstrates the highly efficient ionic rejection of PAH[4]s (Figure 21B). In terms of interpretation of this result, it is still possible that PAH[4]s were not successfully integrated into the membranes during the DIB formation process. Therefore, the unimolecular AWC PAP[5], which is structurally analogous to PAH[4] and found to allow ion permeation in our previous study [37], was used as a positive control and subjected to *I–V* measurements using the DIB system to show the stable insertion of triPhe-chain based unimolecular transmembrane structures into the membranes during the DIB formation. Under the same conditions, PAP[5]-reconstituted membranes showed significant ionic currents with lowered membrane resistance values of ~5-13 GΩ (Figure 21C).

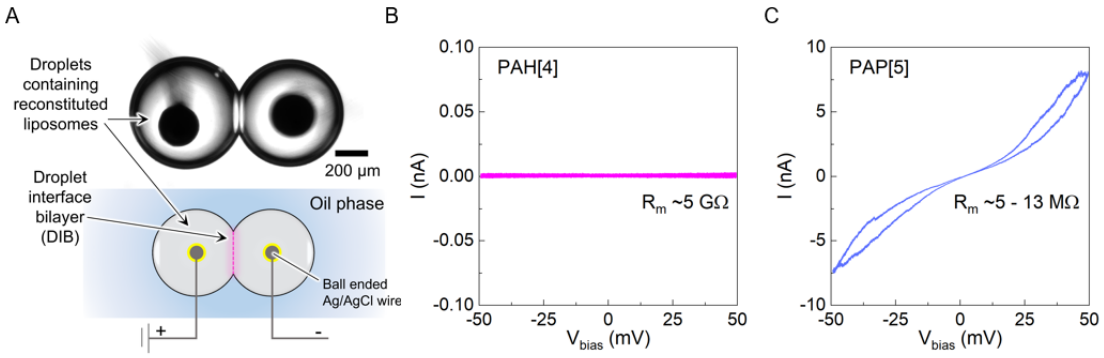

Figure 21. Ionic current measurements of the channels using droplet-interface bilayers. (A) Optical microscope image of hanging droplets with DIB at droplet-contacting interface (upper) and schematic illustration of ionic current measurement setup (bottom panel). I-V plots of (B) PAH[4] (mCLR 0.005) and (C)PAP[5] (mCLR 0.002) reconstituted membranes measured under the DIB system. The nonlinearity of I-V curves of PAP[5] membranes is caused by membrane area change due to electrowetting, not channels.

1.4.4. EVALUATION OF PAH[4] WATER-TO-SALT PERMSELECTIVITY

Based on experimentally measured molecular transport rates, the PAH[4] intrinsic permeabilities of water (P_w) and salt (NaCl (P_s)) were calculated as $(2.2 \pm 0.2) \times 10^{-6}$ cm^2 $\cdot$ s^{-1} and $(1.9 \pm 0.7) \times 10^{-15}$ cm^2 $\cdot$ s^{-1}, respectively, using chloride as the limiting ion. Note that, instead of the pore area, the cross-sectional channel area (~2 nm^2) occupied in the membranes was used to calculate individual permeability values to provide a membrane engineering perspective [22]. As the water channel integration efficiency into a biomimetic membrane matrix is another critical factor in evaluating channel-based membranes, P_w and P_s values for PAH[4]-reconstituted PC/PS lipid membranes were calculated for several cases of channel integration efficiency (α) that ranged from 0.01 to 1, and compared to reported desalination membranes' values (Figure 22). Additionally, representative membranes based on biomimetic water channels (CNTPs and *Rhodobacter sphaeroides* aquaporin Z (RsAqpZ), which is reported to have the highest permeability among the AQP family [21]) were plotted using the same method to provide a comparison of the various types of channel-based biomimetic membranes possible for the development of desalination membranes. As shown in Figure 22, the plot of water/salt selectivity (P_w/P_s) against water permeability (P_w) shows that PC/PS lipid membrane matrices by themselves are below the trade-off upper limit of polymeric desalination membranes. This is reasonable, given that water and salt permeations take place via the solution-diffusion mechanism for both cases. Remarkably, with a gradual increase in channel insertion into the membranes (α = ~0.01 – 1), channel-based biomimetic membranes demonstrate water/NaCl selectivity that far exceeds state-of-the-art polymeric membranes' upper bound limit by several orders of magnitude (Figure 22). It is proposed that this is a conservative estimate of the permeability–selectivity trend for PAH[4]-enhanced biomimetic matrices because quantitative Cl^- ion permeability was used as a model for NaCl permeability.

Usually, under reverse-osmosis conditions, Cl^- permeation is limited by the slower diffusing Na^+. This assumption that Na+ is the limiting ion was used recently to estimate, based on indirect measurements, that biomimetic membranes could have NaCl selectivity in a range three orders of magnitude higher than that shown here [22]. Hence, values reported here represent the conservative evaluation of PAH[4] channel-based desalination membranes with direct measurements of the channel transport rates. However, it is possible that PAH[4] channels could demonstrate an ~10^{12} water-to-salt selectivity as estimated in the previous study for AQPs if Na^+ ion transport rates could be measured accurately and used instead.

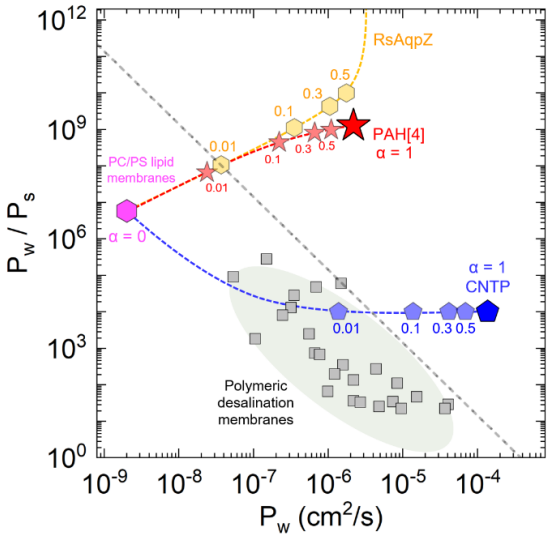

Figure 22. Intrinsic water/NaCl selectivity (*P*w/*P*s) versus *P*w of PAH[4]-, CNTP-, and RsAqpZ-based biomimetic membranes. The data points of channel-reconstituted biomimetic membranes with PC/PS matrix molecules with an increasing fractional area of the membranes occupied by the channels (α = 0.5 indicates that 50% of membrane area is occupied by channels) are compared; α values indicate the corresponding data points for the PAH[4] (red stars), RsAqpZ (orange hexagons) and CNTP (blue pentagons) membranes. The dashed lines for the channel-based membranes are guides for the eye. Data for the representative polymeric desalination membranes (grey squares) and their upper bound trade-off line (dashed grey line) are adapted from Geise et *al.* [67].

1.4.5. COMPUTER SIMULATIONS OF PAH[4] PERMEABILITY

To provide detailed descriptions that relate the microstructure-to-molecular transport properties of PAH[4] clusters, representative PAH[4] cluster configurations were generated *in silico* [70, 71] and subjected to MD simulations (~400 ns) in lipid bilayer patches (Figure 23) (Appendix A provides the details of *in silico* experiments). As the PAH[4] configurations evolved from the monomer to the dimer and to 22-mer clusters, water permeability per PAH[4] molecule enhanced significantly, which suggests a cooperative water-permeating path formation between the PAH[4] molecules (Figure A.1 - A.8). The agreement in permeability values between experiment and simulation along with recapitulating the experimental trend of increasing permeability when clusters are formed with increasing channel density represents the appropriateness of the simulation setting to emulate oligomerized PAH[4] clusters in lipid membranes. In another set of simulations, a transmembrane voltage of ±1 V was applied in two MD simulations of the PAH[4] 22-mer clusters that were most water conductive to measure the ionic conductance, but no ion permeation was observed during each 100 ns simulation, which confirms the ion-exclusion property of PAH[4] channels. In terms of a numerical value, these simulations indicate that the conductance of the membrane patch was <1 pS.

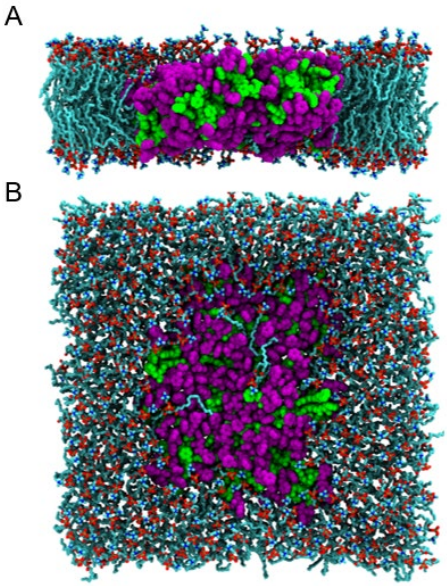

Figure 23. (A) Side and (B) top view of a PAH[4] 22-mer cluster (purple and green) embedded in a model lipid bilayer membrane (turquoise) for MD simulations; water and ions are not shown for visual clarity.

Full MD trajectories provided several insights into the rapid water permeation through PAH[4] clusters. First, all the permeating water molecules have to undergo at least one 'bulk–2D wire–bulk' transition. Two-dimensional water-wire formation is a crucial factor to enable a rapid water conduction via an almost perfect slippage of the water molecules, which cannot be achieved in the systems in which continuum hydrodynamics is predominant [72]. Water-wire formation is not seen in monomeric PAH[4] configurations, which supports the assertion that PAH[4]s provide synergistic paths via cluster formation (Figure A.5). Specifically, analyses of the number of hydrogen bonds for each of the ~800 water molecules that permeated through the PAH[4] 22-mer cluster showed several interesting features in comparison to that in an AQP1 tetramer. As a water molecule approaches the center of the membrane, the number of hydrogen bonds that it forms gradually reduces from an average of ~3.5 to ~2.5 on both sides of the membrane

and then drops rapidly to ~1.5 within the constriction region of the channel, at *Z*-axis values within 9 Å of the membrane's midplane (Figure 24); the number of hydrogen bonds lower than two in the constriction region indicates that water molecules lose their bulk state, which enables a fast permeation in this region [18]. A similar dependence was observed for AQP1, with one major difference: the location of the minimally hydrogen-bonded water molecule was well-defined by the channel's structure, whereas this location was not well-defined in the dynamic PAH[4] clusters. Further, the varying numbers of hydrogen bonds formed by ten randomly chosen water molecules as they pass through each channel was plotted (Figure A.9) for both the PAH[4] and AQP1 channels. This analysis indicated that, in the case of the PAH[4] cluster system, the number of hydrogen bonds of each water molecule could drop even lower than 1.5 during individual permeation events similar to that in AQP1 (Figure A.9). However, owing to the lack of a well-defined structure for PAH[4] clusters, averaging over all the permeating molecule produces a slightly higher minimum number of hydrogen bonds in the constriction region for PAH[4] as compared to that of AQP1.

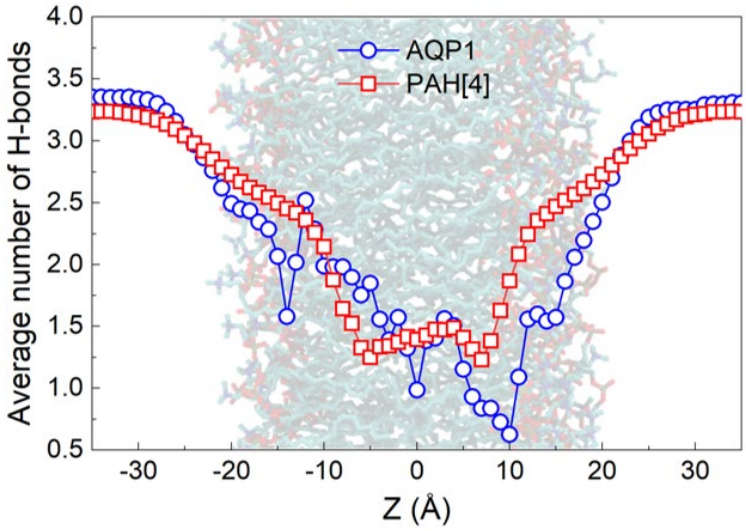

Figure 24. Average number of hydrogen bonds formed by a permeating water molecule as a function of its *Z* coordinate in an AQP1 tetramer and a cluster of PAH[4] channels embedded in a lipid bilayer membrane. To calculate the number of hydrogen bonds, a 3.5 Å distance cutoff between the donor and acceptor and a 40° angle cutoff for the donor–hydrogen–acceptor angle were used. The number of hydrogen bonds was averaged over all the permeated water molecules during the course of the MD trajectory (~800 and ~400 for PAH[4] and AQP1, respectively).

The obtained dependence of the number of hydrogen bonds along the Z axis was used to define the average location of the channel constriction region for both the PAH[4] and AQP1 systems: (−9 Å, 9 Å) and (−14 Å, 14 Å), respectively. Having defined the boundaries of the channel constriction, the path each water molecule took to permeate the PAH[4] cluster or the AQP1 tetramer was used (two such paths are shown for each system in Figure 25) and computed the time it took for each water molecule to pass from one side of the constriction to the other for both systems (Figure A.10). The histograms of the normalized probability of the permeation times are shown in Figure 26 for PAH[4] and AQP1, respectively. As expected, the histogram has a longer tail in the case of the PAH[4] 22-mer cluster, reflective of the more convoluted permeation path for some water

molecules. The average permeation time is, however, of the same order: 20.3 ns for PAH[4] and 5.5 ns for AQP1, with the AQP1 channel showing a fourfold faster transport per permeation path.

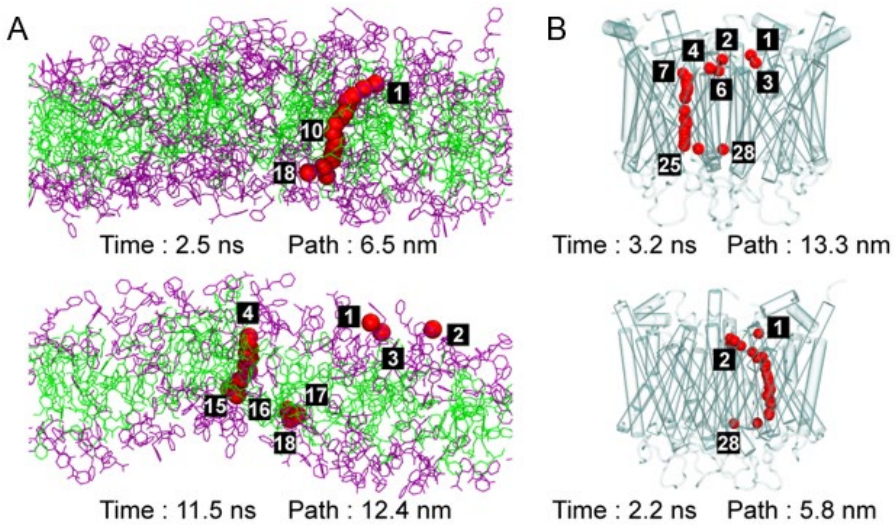

Figure 25. The approximated path of the two representative water molecules permeated through the PAH[4] cluster (A) and the (B) AQP1 tetramer. The PAH[4] molecules are shown using green and purple lines, whereas the AQP1 channel is shown using white semi-transparent cylinders. The red spheres show the average location of the permeating water molecule in each 1 Å bin along the *Z* direction during the permeation path. Lipid and other water molecules are not shown for clarity. The numbers specify the bin index along the *Z* axis, from 1 to 18 or 1 to 28 bins for PAH[4] and AQP1, respectively; some bin numbers are omitted for clarity. The permeation path length and the permeation time of the respective water molecules are specified in each figure.

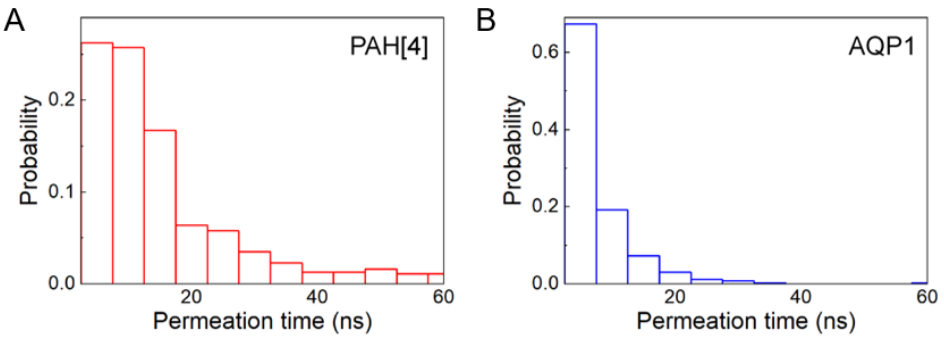

Figure 26. The normalized distribution of the permeation time for all the water molecules that passed through (A) the PAH[4] cluster and (B) the AQP1 tetramer.

The average distance travelled by a water molecule was further compared (Figure A.11). The average permeation path is slightly longer for the PAH[4] channel than that for AQP1, as can be seen from the normalized distributions of the water permeation path lengths (Figure 27). The average location of the water molecules in 1 Å *Z*-axis bins was used to visualize a typical permeation path through the PAH[4] cluster and AQP1 (Figure 25). In the case of AQP1, the permeation path is well-defined, whereas for PAH[4] the path can be either well-defined or dispersed. The results of our analysis suggest that both the average time and the average path taken by a water molecule that permeates through an PAH[4] cluster is of the same order as that for the APQ1 channel. Although both the permeation time and permeation path are statistically longer for PAH[4], the overall permeation rate can approach that of AQP1 if a sufficient number of such channels simultaneously forms per unit area of the membrane, which provides highly efficient water permeation networks. This conclusion is also supported by corresponding experimental observations (channel aggregation and increasing channel permeability at higher channel densities).

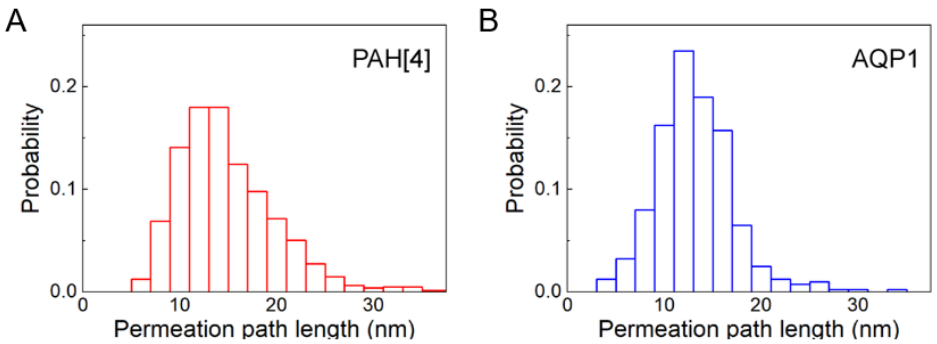

Figure 27. The normalized distribution of the permeation length for all the water molecules that passed through (A) the PAH[4] cluster and (B) the AQP1 tetramer.

Chapter 1.5: Conclusion

The transmembrane unimolecular PAH[4] architecture was shown to enable a highly efficient and selective water permeation through mechanisms distinct from traditional water channels. These mechanisms include lateral aggregation and the formation of an interconnected water-wire network in a biomimetic membrane matrix, which results in intrinsic water/NaCl transport properties that exceed the permselectivity performance of the current desalination membranes by orders of magnitude. Combined with recent progress in maximizing the AWC insertion efficiency in bioinspired block copolymer membranes by up to ~60% and utilizing them for the fabrication of scalable membranes [37], cluster-forming AWCs could pave the way for a unique architecture of bioinspired membranes for a variety of applications.

REFERENCES

[1] Barboiu, M., Artificial Water Channels, Angewandte Chemie International Edition 51(47) (2012) 11674-11676.

[2] Song, W., Lang, C., Shen, Y.-x., Kumar, M., Design Considerations for Artificial Water Channel–Based Membranes, Annual Review of Materials Research 48(1) (2018) 57-82.

[3] Barboiu, M., Artificial water channels – incipient innovative developments, Chemical Communications 52(33) (2016) 5657-5665.

[4] Barboiu, M., Gilles, A., From Natural to Bioassisted and Biomimetic Artificial Water Channel Systems, Accounts of Chemical Research 46(12) (2013) 2814-2823.

[5] Pohl, P., Saparov, S.M., Borgnia, M.J., Agre, P., Highly selective water channel activity measured by voltage clamp: Analysis of planar lipid bilayers reconstituted with purified AqpZ, Proceedings of the National Academy of Sciences, USA 98(17) (2001) 9624-9629.

[6] Murata, K., Mitsuoka, K., Hirai, T., Walz, T., Agre, P., Heymann, J.B., Engel, A., Fujiyoshi, Y., Structural determinants of water permeation through aquaporin-1, Nature 407(6804) (2000) 599-605.

[7] Horner, A., Pohl, P., Single-file transport of water through membrane channels, Faraday Discussions 209(0) (2018) 9-33.

[8] Decker, K., Page, M., Boyd, A., MacAllister, I., Ginsberg, M., Aksimentiev, A., Selective Permeability of Truncated Aquaporin 1 in Silico, ACS Biomaterials Science & Engineering 3(3) (2017) 342-348.

[9] Hummer, G., Rasaiah, J.C., Noworyta, J.P., Water conduction through the hydrophobic channel of a carbon nanotube, Nature 414(6860) (2001) 188-190.

[10] Majumder, M., Chopra, N., Andrews, R., Hinds, B.J., Enhanced flow in carbon nanotubes, Nature 438(7064) (2005) 44-44.

[11] Holt, J.K., Park, H.G., Wang, Y., Stadermann, M., Artyukhin, A.B., Grigoropoulos, C.P., Noy, A., Bakajin, O., Fast Mass Transport Through Sub-2-Nanometer Carbon Nanotubes, Science 312(5776) (2006) 1034-1037.

[12] Khodabakhshi, M., Moosavi, A., Unidirectional Transport of Water through an Asymmetrically Charged Rotating Carbon Nanotube, The Journal of Physical Chemistry C 121(42) (2017) 23649-23658.

[13] Secchi, E., Marbach, S., Niguès, A., Stein, D., Siria, A., Bocquet, L., Massive radius-dependent flow slippage in carbon nanotubes, Nature 537(7619) (2016) 210-213.

[14] Horner, A., Zocher, F., Preiner, J., Ollinger, N., Siligan, C., Akimov, S.A., Pohl, P., The mobility of single-file water molecules is governed by the number of H-bonds they may form with channel-lining residues, Science Advances 1(2) (2015).

[15] Gravelle, S., Joly, L., Detcheverry, F., Ybert, C., Cottin-Bizonne, C., Bocquet, L., Optimizing water permeability through the hourglass shape of aquaporins, Proceedings of the National Academy of Sciences 110(41) (2013) 16367-16372.

[16] Horner, A., Pohl, P., Comment on "Enhanced water permeability and tunable ion selectivity in subnanometer carbon nanotube porins", Science 359(6383) (2018).

[17] Mills, R., Self-diffusion in normal and heavy water in the range 1-45.deg, The Journal of Physical Chemistry 77(5) (1973) 685-688.

[18] Tunuguntla, R.H., Henley, R.Y., Yao, Y.-C., Pham, T.A., Wanunu, M., Noy, A., Enhanced water permeability and tunable ion selectivity in subnanometer carbon nanotube porins, Science 357(6353) (2017) 792-796.

[19] Baaden, M., Barboiu, M., Bill, R.M., Casanova, S., Chen, C.-L., Conner, M., Freger, V., Gong, B., Góra, A., Hinds, B., Horner, A., Hummer, G., Kumar, M., Lokesh, M., Mitra, S., Noy, A., Pohl, P., Sadet, A., Sansom, M., Törnroth-Horsefield, S., Vashisth, H., Structure and function of natural proteins for water transport: general discussion, Faraday Discussions 209(0) (2018) 83-95.

[20] Park, H.B., Kamcev, J., Robeson, L.M., Elimelech, M., Freeman, B.D., Maximizing the right stuff: The trade-off between membrane permeability and selectivity, Science 356(6343) (2017).

[21] Erbakan, M., Shen, Y.-x., Grzelakowski, M., Butler, P.J., Kumar, M., Curtis, W.R., Molecular Cloning, Overexpression and Characterization of a Novel Water Channel Protein from Rhodobacter sphaeroides, PLOS ONE 9(1) (2014) e86830.

[22] Werber, J.R., Elimelech, M., Permselectivity limits of biomimetic desalination membranes, Science Advances 4(6) (2018) eaar8266.

[23] Licsandru, E., Kocsis, I., Shen, Y.-x., Murail, S., Legrand, Y.-M., van der Lee, A., Tsai, D., Baaden, M., Kumar, M., Barboiu, M., Salt-Excluding Artificial Water Channels Exhibiting Enhanced Dipolar Water and Proton Translocation, Journal of the American Chemical Society 138(16) (2016) 5403-5409.

[24] Le Duc, Y., Michau, M., Gilles, A., Gence, V., Legrand, Y.-M., van der Lee, A., Tingry, S., Barboiu, M., Imidazole-Quartet Water and Proton Dipolar Channels, Angewandte Chemie International Edition 50(48) (2011) 11366-11372.

[25] Percec, V., Dulcey, A.E., Balagurusamy, V.S.K., Miura, Y., Smidrkal, J., Peterca, M., Nummelin, S., Edlund, U., Hudson, S.D., Heiney, P.A., Duan, H., Magonov, S.N., Vinogradov, S.A., Self-assembly of amphiphilic dendritic dipeptides into helical pores, Nature 430(7001) (2004) 764-768.

[26] Kaucher, M.S., Peterca, M., Dulcey, A.E., Kim, A.J., Vinogradov, S.A., Hammer, D.A., Heiney, P.A., Percec, V., Selective Transport of Water Mediated by Porous Dendritic Dipeptides, Journal of the American Chemical Society 129(38) (2007) 11698-11699.

[27] Barboiu, M., Le Duc, Y., Gilles, A., Cazade, P.-A., Michau, M., Marie Legrand, Y., van der Lee, A., Coasne, B., Parvizi, P., Post, J., Fyles, T., An artificial primitive mimic of the Gramicidin-A channel, Nature Communications 5(1) (2014) 4142.

[28] Zhou, X., Liu, G., Yamato, K., Shen, Y., Cheng, R., Wei, X., Bai, W., Gao, Y., Li, H., Liu, Y., Liu, F., Czajkowsky, D.M., Wang, J., Dabney, M.J., Cai, Z., Hu, J., Bright, F.V., He, L., Zeng, X.C., Shao, Z., Gong, B., Self-assembling subnanometer pores with unusual mass-transport properties, Nature Communications 3(1) (2012) 949.

[29] Zhao, H., Sheng, S., Hong, Y., Zeng, H., Proton Gradient-Induced Water Transport Mediated by Water Wires Inside Narrow Aquapores of Aquafoldamer Molecules, Journal of the American Chemical Society 136(40) (2014) 14270-14276.

[30] Zhao, H., Ong, W.Q., Fang, X., Zhou, F., Hii, M.N., Li, S.F.Y., Su, H., Zeng, H., Synthesis, structural investigation and computational modelling of water-binding aquafoldamers, Organic & Biomolecular Chemistry 10(6) (2012) 1172-1180.

[31] Schneider, S., Licsandru, E.-D., Kocsis, I., Gilles, A., Dumitru, F., Moulin, E., Tan, J., Lehn, J.-M., Giuseppone, N., Barboiu, M., Columnar Self-Assemblies of Triarylamines

as Scaffolds for Artificial Biomimetic Channels for Ion and for Water Transport, Journal of the American Chemical Society 139(10) (2017) 3721-3727.

[32] Hu, X.-B., Chen, Z., Tang, G., Hou, J.-L., Li, Z.-T., Single-Molecular Artificial Transmembrane Water Channels, Journal of the American Chemical Society 134(20) (2012) 8384-8387.

[33] Si, W., Chen, L., Hu, X.-B., Tang, G., Chen, Z., Hou, J.-L., Li, Z.-T., Selective Artificial Transmembrane Channels for Protons by Formation of Water Wires, Angewandte Chemie International Edition 50(52) (2011) 12564-12568.

[34] Chen, L., Si, W., Zhang, L., Tang, G., Li, Z.-T., Hou, J.-L., Chiral Selective Transmembrane Transport of Amino Acids through Artificial Channels, Journal of the American Chemical Society 135(6) (2013) 2152-2155.

[35] Si, W., Hu, X.-B., Liu, X.-H., Fan, R., Chen, Z., Weng, L., Hou, J.-L., Self-assembly and proton conductance of organic nanotubes from pillar[5]arenes, Tetrahedron Letters 52(19) (2011) 2484-2487.

[36] Feng, W.-X., Sun, Z., Barboiu, M., Pillar[n]arenes for Construction of Artificial Transmembrane Channels, Israel Journal of Chemistry 58(11) (2018) 1209-1218.

[37] Shen, Y.-x., Song, W., Barden, D.R., Ren, T., Lang, C., Feroz, H., Henderson, C.B., Saboe, P.O., Tsai, D., Yan, H., Butler, P.J., Bazan, G.C., Phillip, W.A., Hickey, R.J., Cremer, P.S., Vashisth, H., Kumar, M., Achieving high permeability and enhanced selectivity for Angstrom-scale separations using artificial water channel membranes, Nature Communications 9(1) (2018) 2294.

[38] Tajkhorshid, E., Nollert, P., Jensen, M.Ø., Miercke, L.J.W., O'Connell, J., Stroud, R.M., Schulten, K., Control of the Selectivity of the Aquaporin Water Channel Family by Global Orientational Tuning, Science 296(5567) (2002) 525-530.

[39] Saparov, S.M., Pfeifer, J.R., Al-Momani, L., Portella, G., de Groot, B.L., Koert, U., Pohl, P., Mobility of a One-Dimensional Confined File of Water Molecules as a Function of File Length, Physical Review Letters 96(14) (2006) 148101.

[40] Boinski, T., Cieszkowski, A., Rosa, B., Szumna, A., Hybrid [n]Arenes through Thermodynamically Driven Macrocyclization Reactions, The Journal of Organic Chemistry 80(7) (2015) 3488-3495.

[41] Shen, Y.-x., Si, W., Erbakan, M., Decker, K., De Zorzi, R., Saboe, P.O., Kang, Y.J., Majd, S., Butler, P.J., Walz, T., Highly permeable artificial water channels that can self-assemble into two-dimensional arrays, Proceedings of the National Academy of Sciences, USA 112(32) (2015) 9810-9815.

[42] Shen, Y.-x., Si, W., Erbakan, M., Decker, K., De Zorzi, R., Saboe, P.O., Kang, Y.J., Majd, S., Butler, P.J., Walz, T., Aksimentiev, A., Hou, J.-l., Kumar, M., Highly permeable artificial water channels that can self-assemble into two-dimensional arrays, Proceedings of the National Academy of Sciences, USA 112(32) (2015) 9810-9815.

[43] Woodle, M.C., Papahadjopoulos, D., [9] Liposome preparation and size characterization, Methods in Enzymology, Academic Press1989, pp. 193-217.

[44] Latimer, P., Pyle, B.E., Light Scattering at Various Angles: Theoretical Predictions of the Effects of Particle Volume Changes, Biophysical journal 12(7) (1972) 764-773.

[45] Borgnia, M.J., Kozono, D., Calamita, G., Maloney, P.C., Agre, P., Functional reconstitution and characterization of AqpZ, the E. coli water channel protein11Edited by W. Baumeister, Journal of Molecular Biology 291(5) (1999) 1169-1179.

[46] Najem, J.S., Taylor, G.J., Weiss, R.J., Hasan, M.S., Rose, G., Schuman, C.D., Belianinov, A., Collier, C.P., Sarles, S.A., Memristive Ion Channel-Doped Biomembranes as Synaptic Mimics, ACS Nano 12(5) (2018) 4702-4711.

[47] Taylor, G.J., Venkatesan, G.A., Collier, C.P., Sarles, S.A., Direct in situ measurement of specific capacitance, monolayer tension, and bilayer tension in a droplet interface bilayer, Soft Matter 11(38) (2015) 7592-7605.

[48] Humphrey, W., Dalke, A., Schulten, K., VMD: Visual molecular dynamics, Journal of Molecular Graphics and Modelling 14(1) (1996) 33-38.

[49] Vanommeslaeghe, K., Hatcher, E., Acharya, C., Kundu, S., Zhong, S., Shim, J., Darian, E., Guvench, O., Lopes, P., Vorobyov, I., CHARMM general force field: A force field for drug-like molecules compatible with the CHARMM all-atom additive biological force fields, Journal of Computational Chemistry 31(4) (2010) 671-690.

[50] Best, R.B., Zhu, X., Shim, J., Lopes, P.E., Mittal, J., Feig, M., MacKerell Jr, A.D., Optimization of the additive CHARMM all-atom protein force field targeting improved sampling of the backbone ϕ, ψ and side-chain $\chi 1$ and $\chi 2$ dihedral angles, Journal of Chemical Theory and Computation 8(9) (2012) 3257-3273.

[51] Jo, S., Kim, T., Iyer, V.G., Im, W., CHARMM-GUI: a web-based graphical user interface for CHARMM, Journal of Computational Chemistry 29(11) (2008) 1859-1865.

[52] Jorgensen, W.L., Chandrasekhar, J., Madura, J.D., Impey, R.W., Klein, M.L., Comparison of simple potential function for simulating liquid water, Journal of Chemical Physics 79(2) (1983) 926-935.

[53] Sui, H., Han, B.-G., Lee, J.K., Walian, P., Jap, B.K., Structural basis of water-specific transport through the AQP1 water channel, Nature 414 (2001) 872.

[54] Phillips, J.C., Braun, R., Wang, W., Gumbart, J., Tajkhorshid, E., Villa, E., Chipot, C., Skeel, R.D., Kale, L., Schulten, K., Scalable molecular dynamics with NAMD, Journal of Computational Chemistry 26(16) (2005) 1781-1802.

[55] Feller, S.E., Zhang, Y., Pastor, R.W., Brooks, B.R., Constant pressure molecular dynamics simulation: the Langevin piston method, Journal of Chemical Physics 103(11) (1995) 4613-4621.

[56] Martyna, G.J., Tobias, D.J., Klein, M.L., Constant pressure molecular dynamics algorithms, Journal of Chemical Physics 101(5) (1994) 4177-4189.

[57] Sindhikara, D.J., Kim, S., Voter, A.F., Roitberg, A.E., Bad seeds sprout perilous dynamics: Stochastic thermostat induced trajectory synchronization in biomolecules, Journal of Chemical Theory and Computation 5(6) (2009) 1624-1631.

[58] Klauda, J.B., Venable, R.M., Freites, J.A., O'Connor, J.W., Tobias, D.J., Mondragon-Ramirez, C., Vorobyov, I., MacKerell Jr, A.D., Pastor, R.W., Update of the CHARMM all-atom additive force field for lipids: validation on six lipid types, Journal of Physical Chemistry B 114(23) (2010) 7830-7843.

[59] Yoo, J., Aksimentiev, A., New tricks for old dogs: improving the accuracy of biomolecular force fields by pair-specific corrections to non-bonded interactions, Physical Chemistry Chemical Physics 20(13) (2018) 8432-8449.

[60] Yoo, J., Aksimentiev, A., Refined Parameterization of Nonbonded Interactions Improves Conformational Sampling and Kinetics of Protein Folding Simulations, Journal of Physical Chemistry Letters 7(19) (2016) 3812-3818.

[61] Yoo, J., Aksimentiev, A., Improved parameterization of amine–carboxylate and amine–phosphate interactions for molecular dynamics simulations using the CHARMM

and AMBER force fields, Journal of Chemical Theory and Computation 12(1) (2015) 430-443.

[62] Yoo, J., Aksimentiev, A., Improved parametrization of Li+, Na+, K+, and Mg2+ ions for all-atom molecular dynamics simulations of nucleic acid systems, Journal of Physical Chemistry Letters 3(1) (2012) 45-50.

[63] Miyamoto, S., Kollman, P.A., Settle: An analytical version of the SHAKE and RATTLE algorithm for rigid water models, Journal of Computational Chemistry 13(8) (1992) 952-962.

[64] Andersen, H.C., Rattle: A "velocity" version of the shake algorithm for molecular dynamics calculations, Journal of Computational Physics 52(1) (1983) 24-34.

[65] Roe, D.R., Cheatham, T.E., III, PTRAJ and CPPTRAJ: Software for Processing and Analysis of Molecular Dynamics Trajectory Data, Journal of Chemical Theory and Computation 9(7) (2013) 3084-3095.

[66] Hannesschläger, C., Barta, T., Siligan, C., Horner, A., Quantification of Water Flux in Vesicular Systems, Scientific Reports 8(1) (2018) 8516.

[67] Geise, G.M., Park, H.B., Sagle, A.C., Freeman, B.D., McGrath, J.E., Water permeability and water/salt selectivity tradeoff in polymers for desalination, Journal of Membrane Science 369(1) (2011) 130-138.

[68] Toyoshima, Y., Thompson, T.E., Chloride flux in bilayer membranes. Chloride permeability in aqueous dispersions of single-walled, bilayer vesicles, Biochemistry 14(7) (1975) 1525-1531.

[69] Lang, C., Li, W., Dong, Z., Zhang, X., Yang, F., Yang, B., Deng, X., Zhang, C., Xu, J., Liu, J., Biomimetic Transmembrane Channels with High Stability and Transporting Efficiency from Helically Folded Macromolecules, Angewandte Chemie International Edition 55(33) (2016) 9723-9727.

[70] Chowdhury, R., Ren, T., Shankla, M., Decker, K., Grisewood, M., Prabhakar, J., Baker, C., Golbeck, J.H., Aksimentiev, A., Kumar, M., Maranas, C.D., PoreDesigner for tuning solute selectivity in a robust and highly permeable outer membrane pore, Nature Communications 9(1) (2018) 3661.

[71] Entzminger, K.C., Hyun, J.-m., Pantazes, R.J., Patterson-Orazem, A.C., Qerqez, A.N., Frye, Z.P., Hughes, R.A., Ellington, A.D., Lieberman, R.L., Maranas, C.D., Maynard, J.A., De novo design of antibody complementarity determining regions binding a FLAG tetra-peptide, Scientific Reports 7(1) (2017) 10295.

[72] Berezhkovskii, A., Hummer, G., Single-File Transport of Water Molecules through a Carbon Nanotube, Physical Review Letters 89(6) (2002) 064503.

SECTION 2: ARTIFICIAL WATER CHANNEL-BASED MEMBRANES[2]

Chapter 2.1: Abstract

Synthetic polymer membranes, critical to diverse energy-efficient separations, are subject to permeability-selectivity trade-offs that decrease their overall efficacy. These trade-offs are due to structural variations (e.g., broad pore size distributions) in both nonporous membranes and porous membranes. Biological membranes utilize well-defined Angstrom-scale pores to provide exceptional transport properties and can be used as inspiration to overcome this trade-off. In this section, a comprehensive demonstration of such a bioinspired approach is presented based on pillar[5]arene artificial water channels, peptide-appended pillar[5]arenes (PAP[5]s), resulting in channel-based synthetic polymer membranes. These membranes have a sharp selectivity profile with a molecular weight cutoff of ~ 500 Da, a size range challenging to achieve with current membranes, while achieving a large improvement in permeability (~65 $L \cdot m^{-2} \cdot h^{-1} \cdot bar^{-1}$ compared with 4 – 7 $L \cdot m^{-2} \cdot h^{-1} \cdot bar^{-1}$) over similarly rated commercial membranes.

---

[2] This section has been adapted from:

Shen, Y.-x. Song, W. Barden, D.R. Ren, T. Lang, C. Feroz, H. Henderson, C.B. Saboe, P.O. Tsai, D. Yan, H. Butler, P.J. Bazan, G.C. Phillip, W.A. Hickey, R.J. Cremer, P.S. Vashisth, H. and Kumar, M. Achieving high permeability and enhanced selectivity for Angstrom-scale separations using artificial water channel membranes. *Nature Communications* 9, 2294 (2018).

Song, W. Shen, Y.-x. Lang, C. Saha, P. Zenyuk, I.V. Hickey, R.J. and Kumar, M. Unique selectivity trends of highly permeable PAP[5] water channel membranes *Faraday Discussions* 209, 193-204 (2018).

Woochul Song (W.S.) conceived and designed the research. W.S. performed the experiments of channel-based membrane fabrication and transport study. W.S. analyzed the data. W.S. wrote the paper.

Chapter 2.2: Introduction and Background

In this chapter, an inception-to-implementation description of highly permeable and selective channel-based polymer membranes is presented, which are consisting of well-defined, densely packed artificial water channels (AWCs). The design of the channel used in this work, peptide-appended pillar[5]arene (PAP[5]) artificial water channel with a pore size of ~ 5 Å [1], was inspired by AQPs found in cell membranes (Figure 28). For the practical implementation of AWCs into scalable membranes, amphiphilic block copolymers (BCPs) are used as self-assembled membrane matrices instead of lipids (Figure 29). BCPs form lipid-like bilayer structures, and are more mechanically and chemically stable than lipids, and offer customizable polymer types, membrane thicknesses, and terminal functional groups [2, 3, 4]. Poly(butadiene)-b-poly(ethylene oxide) di-block copolymers were chosen because they have been used to study membrane proteins and demonstrate unique self-assembly properties including the ability to assemble membrane channels into two-dimensional crystals [5, 6]. The water conductance of PAP channels in BCPs was determined to be in the range of AQPs ($\sim 10^8 - 10^9$ water molecules $\cdot$ s^{-1}), confirmed by both experiments and simulations. For the membrane fabrication, PAP[5] channels were successfully packed into two-dimensional sheets within PB-PEO polymers through a controlled self-assembly process; and the composite membranes were synthesized by depositing these 2D sheets using a layer-by-layer technique on porous substrates (Figure 30). These membranes preserve the permeability and selectivity properties of PAP[5] channels determined at molecular scale. These channel-based membranes demonstrated the water permeance with order of magnitude above corresponding commercial membranes while maintaining a close to ideal selectivity expected from a membrane with monodisperse 5 Å pores.

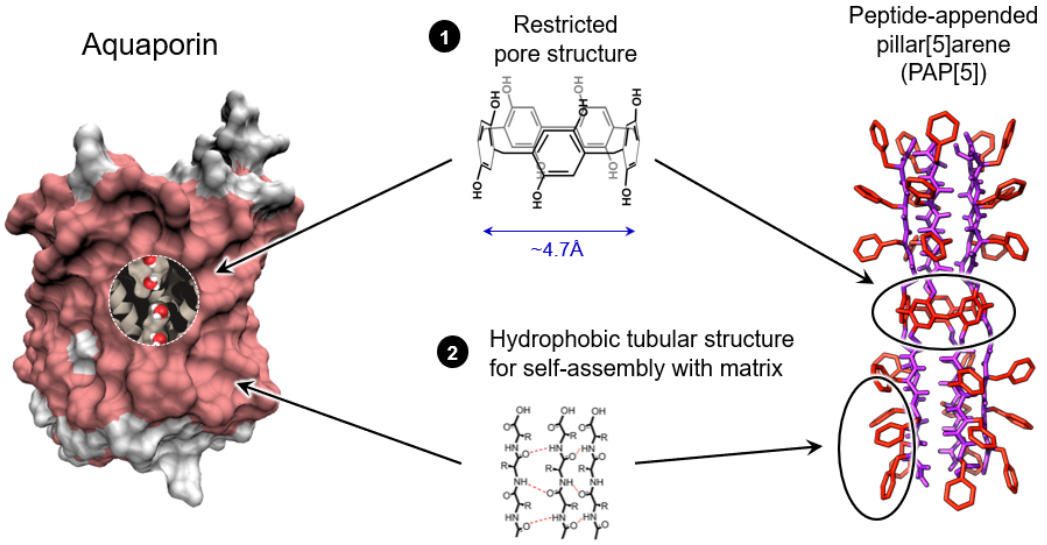

Figure 28. Representative structural comparison between aquaporin and PAP[5] water channels.

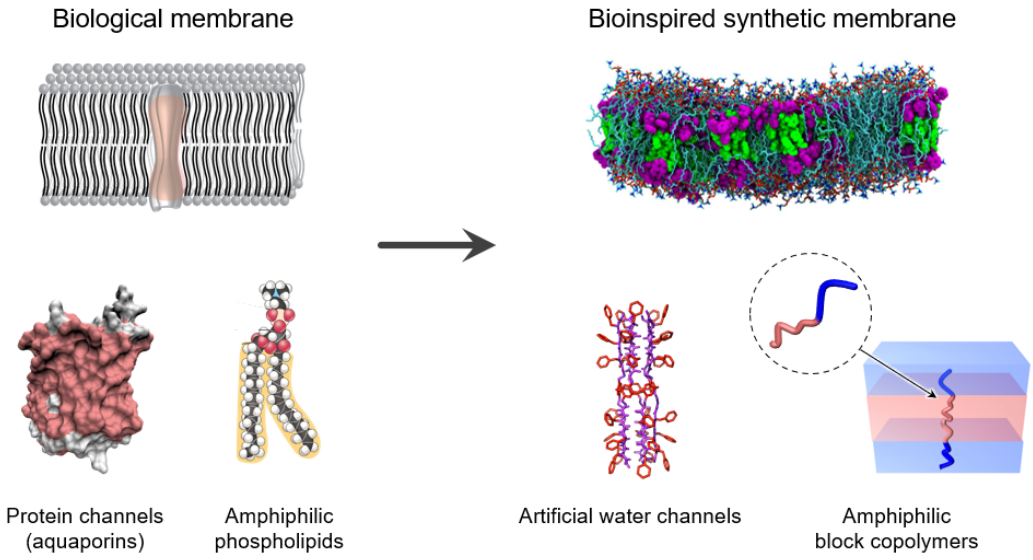

Figure 29. Schematic illustration of the design concept of bioinspired channel-based polymer membranes.

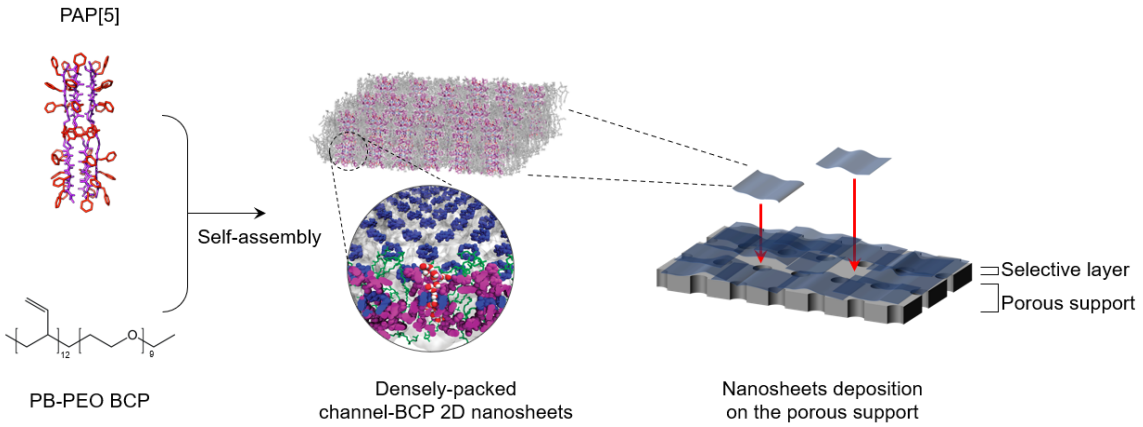

Figure 30. Schematic illustration of PAP[5] channel implementation into scalable polymer membranes. PAP[5] channels and PB-PEO diBCPs were reconstituted into 2D nanosheets through controlled self-assembly, and the 2D nanosheets were deposited on top of porous support membranes to prepare thin-film composite membrane structures.

Chapter 2.3: Materials and Experimental Methods

2.3.1. Self-assembly of PAP[5] channel/PB-PEO 2D nanosheets (aggreagates)

PAP[5] channels and PB-PEO diBCPs were reconstituted into 2D nanosheets using a slow dialysis method as described elsewhere [5, 7]. In brief, 0.06 mg PB-PEO polymers were dissolved in $CHCl_3$ with desirable amounts of PAP[5] channels in the flasks. The solution was evaporated and rehydrated with dialysis buffer (10 mM HEPES, 100 mM NaCl, and 0.01% NaN_3 (w/v) at pH 7.0), which contained 4% (w/v) *n*-octyl-β-D-glucoside (OG) detergents. The rehydrated solution was transferred to 12-kDa MWCO dialysis membrane with final concentration of 1mg · ml^{-1}. The volume of dialysis solution was doubled with detergent-free buffer every 12 hours until the OG concentration of the buffer reached 0.25% (w/v). After this, the buffer was replaced with detergent-free buffer three times every 12 hours.

2.3.2. FABRICATION OF COMPOSITE MEMBRANES

PAP[5]/PB-PEO 2D sheets were made via the slow dialysis method as mentioned above. Carboxylic PB12 copolymers were used so that the final 2D sheets were fully carboxylic terminated. The molar channel to polymer ratio was control within 0.3 − 0.5 to so that the majority of the PAP[5]/PB-PEO aggregates were in the form of giant collapsed vesicles and 2D sheets. A total of 50 nm track-etched PC membranes and 30 nm PES membranes were used as substrates. They were first treated in a UV/Ozone cleaner for 30 s in order to ionize the surface (the shiny side) to obtain a negatively charged surface. The cleaned membranes, of 2.5 cm diameter, were placed onto a stainless steel mesh and assembled into a stirred cell (Model 8010, Millipore Corp., MA). The membranes were covered with 1ml polyelectrolyte solution containing 40mM PEI (60,000 Da), 35mM CaCl2, and 0.5M NaCl at pH of 5.548. After incubation for 15 min, the solution was discarded, and the membranes were rinsed with DI water and replaced with 10 μl 2D sheets suspension diluted to 1 ml using the same buffer at pH of 8. The suspension was then filtered through the membranes after another 15 min. Thus, one layer of PEI and 2D sheets was physically deposited onto the substrates. After a desired number of layers was immobilized, the membranes were incubated overnight with 1mg · ml^{-1} 1-Ethyl-3-(3-dimethylaminopropyl)carbodiimide, 1mg · ml^{-1} *N*-hydroxysuccinimide, and 10 mM potassium phosphate at pH of 7. The incubation chemically cross-linked the amine groups from PEI and the carboxylic groups from the 2D sheets.

2.3.3. EVALUATION OF PAP[5]-PB/PEO MEMBRANES

The PAP[5]-PB/PEO membranes were evaluated in terms of water permeance and rejection properties by dead-end stirred filtration. Hydraulic permeance was estimated using the following Equation (2.1).

$$L_p = \frac{J_v}{\Delta P} \tag{2.1}$$

where L_p is the hydraulic permeability ($L \cdot m^{-2} \cdot h^{-1} \cdot bar^{-1}$, LMH/bar), J_v is the volumetric flux of water ($L \cdot m^{-2} \cdot h^{-1}$, LMH) and ΔP is the applied pressure (bar) difference across the membranes. The membranes were tested at 70 psi and volumetric flow rates were measured after they became consistent with filtration time. The solute rejection tests were carried out with different sets of molecules with various molecular weights or ionic valence ratios, including organic dyes (35mM), ionic salts (0.5 mM) and PEO oligomers ($1\ g \cdot L^{-1}$). The rejection of each solute was calculated based on the Equation (2.2).

$$R = \left(1 - \frac{C_P}{C_F}\right) \times 100 \tag{2.2}$$

where R is the rejection of solute (%), and C_P and C_F are the solute concentrations in the permeate and feed solutions, respectively. The concentrations of ions, organic dyes and PEO oligomers were measured using conductivity measurements, UV-vis spectrometry, and a total organic carbon analyzer, respectively.

2.3.4. CONCENTRATION POLARIZATION CORRECTION

The rejection property of the PAP[5]/PB-PEO membranes were corrected using the stagnant film model [8, 9].

$$R' = 1 - \frac{C_P}{C_M} = \frac{R}{R + e^{-J/k(1-R)}} \tag{2.3}$$

where C_M is the concentration of solutes at the feed-side membrane surfaces, k is the mass transfer coefficient, and R is apparent rejection of the membranes. Here, mass transfer coefficient k for each dye can be determined from Colton-Smith empirical correlation [9, 10, 11].

$$Sh = 0.285\, Re^{0.567} Sc^{0.33} (8 \times 10^3 < Re \leq 3.2 \times 10^4) \tag{2.4}$$

$$Sh = 0.443\, Re^{0.746} Sc^{0.33} (3.2 \times 10^4 < Re \leq 8.2 \times 10^4) \tag{2.5}$$

where Reynold number, $Re = \rho\omega r^2/\mu$, Schmidt number, $Sc = \mu/(\rho D)$ and Sherwood number, $Sh = kr/D$ with ρ, ω, μ, D and r being density, rotation speed (in radians per sec), viscosity, diffusivity, and stirred cell effective radius (8.5 mm) respectively. J is the volumetric flux through the membrane. Diffusivity D can be calculated from Stokes-Einstein equation.

$$D = \frac{kT}{6\pi\mu a} \tag{2.6}$$

where k, T and a being Boltzmann constant, temperature and molecule radius respectively. Molecule radius a (nm) is estimated from the Equation (2.7) [12].

$$a = 0.066 M^{1/3} \tag{2.7}$$

where M being the molecular weight. Each dye molecule was assumed to have the simplest shape, a sphere, and the partial specific volume is similar to that of proteins.

2.3.5. ANALYSIS OF THE MWCO CURVE SHAPES

A simple logistic function (a type of sigmoid function) [13] was used to characterize the S-shaped curve of the molecular weight cutoff data and its derivative is a continuous probability distribution, which is a probability density function can be used to determine the pore size distribution.

$$y = \frac{1}{1+e^{-\gamma x+\beta}} \tag{2.8}$$

$$y' = \gamma \frac{e^{-\gamma x+\beta}}{\left(1+e^{-\gamma x+\beta}\right)^2} \tag{2.8}$$

The standard deviation (σ) of this pore size distribution is Equation (2.9).

$$\sigma = \frac{\pi}{\sqrt{3}\gamma} \tag{2.9}$$

2.3.6. STEERED MD SIMULATIONS

To validate the selectivity of PAP channels, a series of steered MD simulations on two selected dye molecules were performed [14]. Methyl orange (MO, 328 Da) and rose bengal (RB, 1018 Da) dyes were chosen, based on the selectivity experiments of PAP[5] with MO able to transport through the channel and RB rejected. This conjecture was tested by pulling each molecule through the central ring of PAP for 10 times. Structures and parameters for the dyes were generated using the CHARMM-GUI Ligand Reader and Modeler [15]. Systems were prepared by taking the initial POPC simulation structures and adding a single dye molecule displaced 10 Å from the central ring of PAP[5]. Harmonic constraints with a force constant of 2 kcal · mol^{-1} were placed on the dye and the central

ring of PAP[5] to keep them in place while the rest of the system was equilibrated in the NPT ensemble at 303 K and 1 atm for 25 ns. Pulling runs were performed at a rate of 10 Å · ns^{-1} with a spring constant of 1000 kcal · mol^{-1}. Harmonic constraints with a force constant of 2 kcal · mol^{-1} were kept on the central ring of PAP[5] to hold it in place. The simulation runs were averaged together and then integrated to construct the potential of mean force for each molecule. These free energy values could explain the selectivity of PAP channels to different dye molecules.

Chapter 2.4: Results and Discussions

2.4.1. Fabrication and characterization of PAP[5] channel 2D nanosheet composite membranes

PAP[5] channels and PB-PEO BCPs formed micron sized 2D sheets through controlled self-assembly using the dialysis method as observed in the transmission electron microscopy (TEM) images (Figure 31). The large aspect ratio of the nanosheets made them ideal for membrane fabrication. Each PAP[5] channel has five carboxylic acid groups at each end of the channel. PB-PEO BCPs were functionalized with carboxylic groups so that the final 2D sheets were fully carboxylate terminated. A modified layer-by-layer method was then used to immobilize these 2D sheets onto polycarbonate track-etched membranes (PC) and polyethersulfone microfiltration (PES) support membranes with the aid of polyethyleneimine (PEI) (Figure 32) [16]. After three and four cycles of modification, 2D sheets achieved ~ 100% coverage on track-etched polycarbonate (PC) and PES membranes, respectively as observed by scanning electron microscopy (SEM) (Figure 33 and Figure 34). The sharp edges of these sheets can be observed in the SEM images. The permeability gradually decreased with the increasing cycles of modification (Figure 35),

and reached 3.0 ± 1.2 LMH/bar and 64.8 ± 11.3 LMH/bar for completely covered PC and PES membranes, respectively (Figure 36A). A series of charged low molecular weight dyes were selected for conducting solute rejection tests. First, a filtration test was performed on PEI-modified control membranes over a period of 60 min to exclude the adsorption effect contributed by polyelectrolytes (Figure 37) [17] and a similar protocol was then followed with each of the selected dyes. The dye rejection properties improved as the number of depositions increased (Figure 37). The molecular exclusion limit of PC and PES membranes were ~560 Da and ~450 Da when completely covered with PAP 2D sheets, respectively (Figure 36B), which is very close to the designed PAP[5] pore, which has an exclusion limit of ~500 Da [1]. This size range is significant as only two commercial membranes exist with a MWCO ~ 500 Da with the entire range of NF membranes reported in literature (Figure 38) shown in spanning 200 − 1000 Da and exhibiting an average permeability of ~10.0 (±6.6) LMH/bar. The molecular weight cutoff probability distributions after fitting the solute exclusion data to a sigmoidal curve model showed that the composite PES membrane presented a sharper pore size distribution (based on the ratio of standard deviation to average MWCO) compared with two commercial membranes of MWCO ~ 400 − 500 Da: N30F [18] and NDX (Figure 36B), which were also tested using the same dyes. The composite membranes also showed a consistent molecular weight cutoff trend with both positively and negatively charged dyes (Figure 39 and Figure 40).

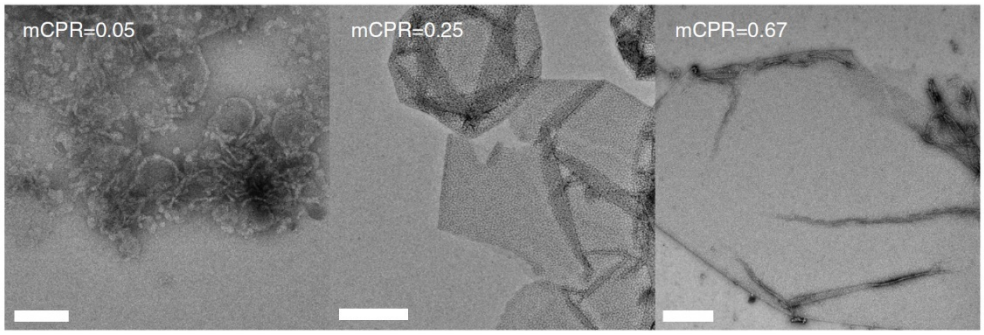

Figure 31. TEM images of PAP[5]/PB-PEO nanosheet aggregates. Micron-scale nanosheets with high aspect ratios were observed at high mCPRs (molar ratio of channels to polymers).

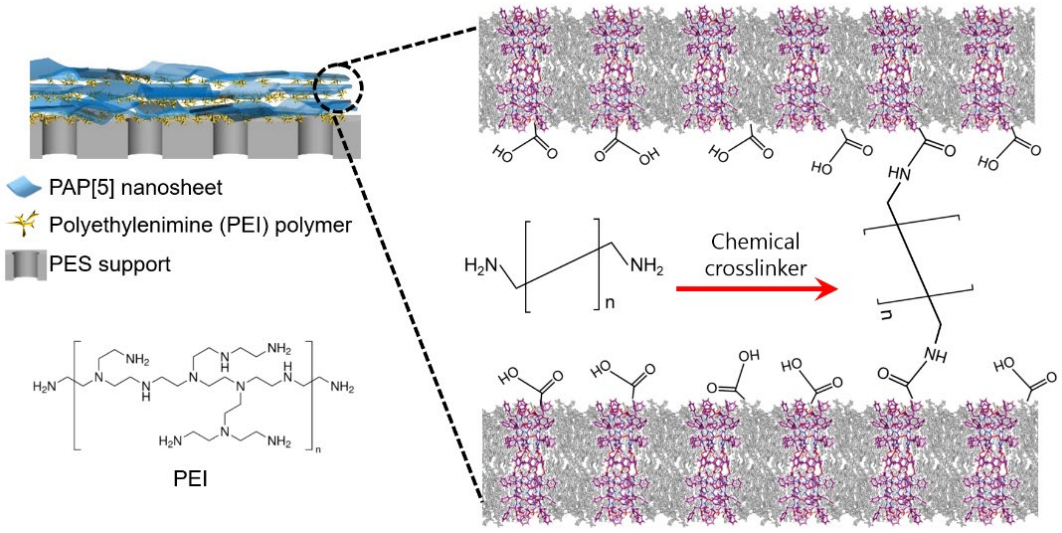

Figure 32. Schematic illustration of layer-by-layer deposition of PAP[5]/BCP nanosheets and PEI polymers to form selective layers on top of PES support membranes.

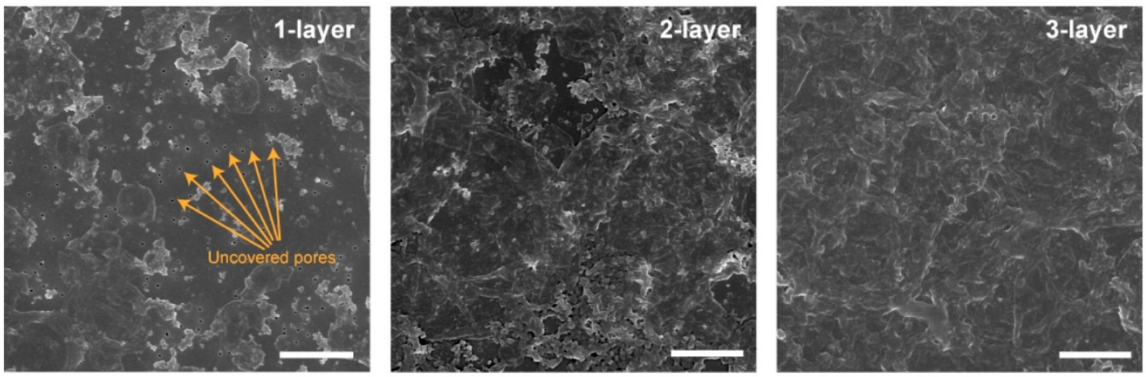

Figure 33. SEM images showed the coverage of PAP[5] 2D sheets on PC support membranes after 1, 2, and 3 cycles of layer-by-layer deposition. Scale bars are 2 μm.

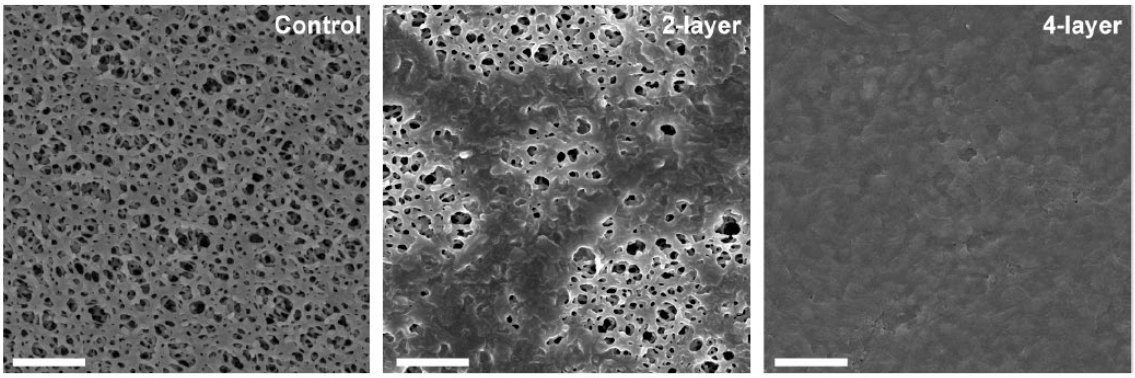

Figure 34. SEM images showed the coverage of PAP[5] 2D nanosheets on PES membranes after 0, 2, and 4 cycles of layer-by-layer depositions. Scale bars are 2 μm.

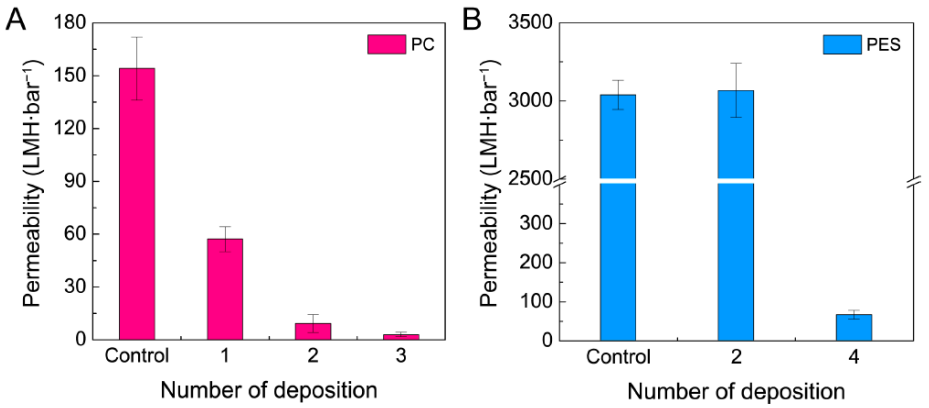

Figure 35. For PAP[5] channels 2D sheet composite membranes, the permeability decreased as the number of depositions increased. Panel A and B were the results using 50 nm track-etched polycarbonate (PC) membranes and 30 nm polysulfone (PES) ultrafiltration membranes as support membranes, respectively. Data shown are the average of triplicate measurements with standard deviation.

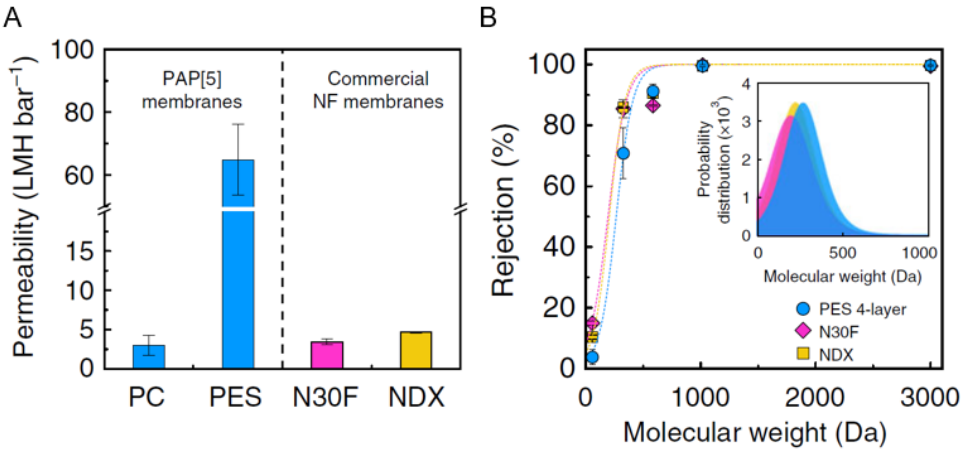

Figure 36. Water permeance and rejection profiles of PAP[5]/PB-PEO composite membranes. (A) After three and four cycles of deposition on PC and PES membranes, the permeabilities were 3.0 ± 1.2 LMH/bar and 64.8 ± 11.3 LMH/bar, respectively, (mean ± s.d., n = 3). The permeability of the modified PES membranes is approximately one order of magnitude higher that of commercial nanofiltration membrane N30F (3.4 ± 0.3 LMH bar−1) and NDX (4.6 ± 0.1 LMH bar−1) with a similar molecular weight cutoff (MWCO). (B) The molecular weight cutoff (MWCO) was ~ 450 Da, 370 Da, and 360 Da for the modified PES membrane, commercial N30F and NDX membranes, respectively, as determined from filtration of dyes of various molecular weights. The molecular weight cutoff probability distributions derived from fitting to a sigmoidal model showed the standard deviation (σ) of modified PES (132 Da) membranes was similar to that of N30F (146 Da) and NDX (125 Da). The pore size distribution is tighter for the PES membrane with a σ/MWCO ratio of 0.29 compared with 0.35 – 0.39 for the commercial membranes. The measured rejection values were corrected using a concentration polarization model and all the cutoff data were fit to a sigmoidal function, as described in Method section.

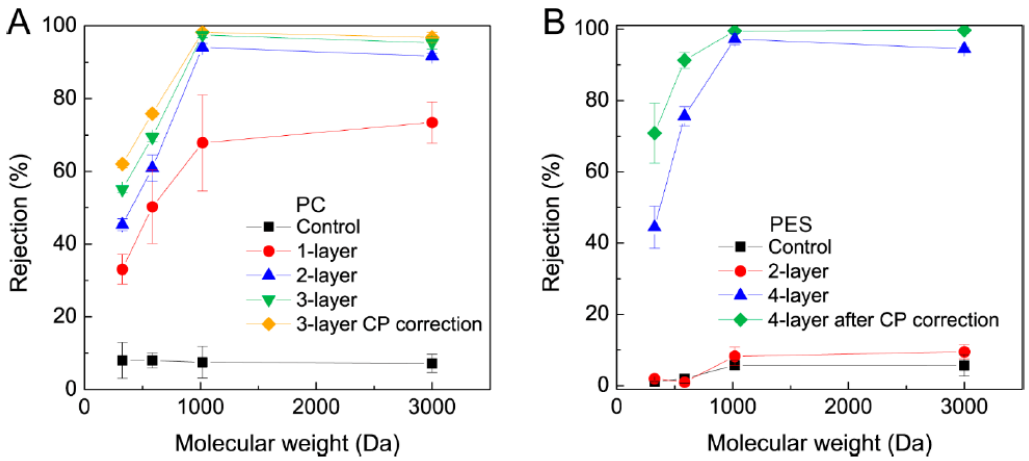

Figure 37. For PAP[5] channels 2D sheet composite membranes, the rejection properties against dye molecules improved as the number of depositions increased. The dye molecules included methyl orange, acid fuchsin, rose bengal and fluorescent dextran. Panel A and B were the results using 50 nm track-etched PC and 30 nm PES ultrafiltration membranes as support membranes, respectively. The rejections (3-layer on PC and 4-layer on PES membranes) were corrected by a concentration polarization model described in Supplementary Methods. Data shown are the average of triplicate measurements with standard deviation.

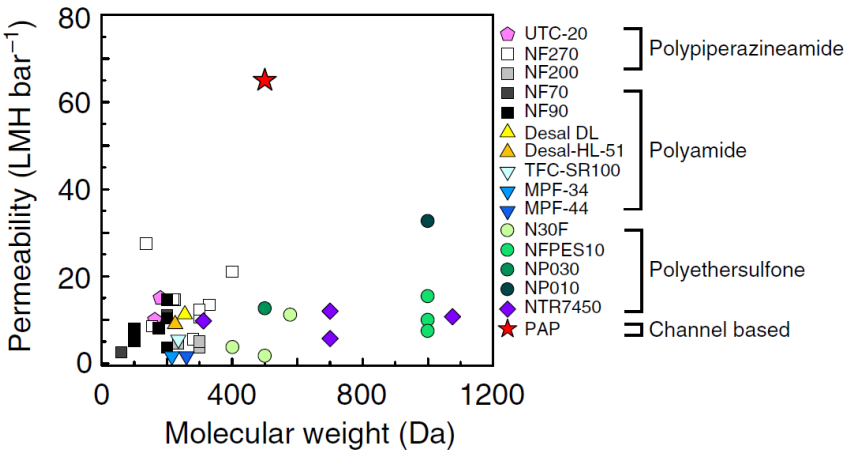

Figure 38. A comparison of PAP[5] channel-based membrane to other commercial NF membranes shows that within the cutoff range (400~500 Da), the channel-based membrane has one order of magnitude higher permeability and in general is several times higher that of commercial nanofiltration membranes across the complete range of available data on such membranes from literature.

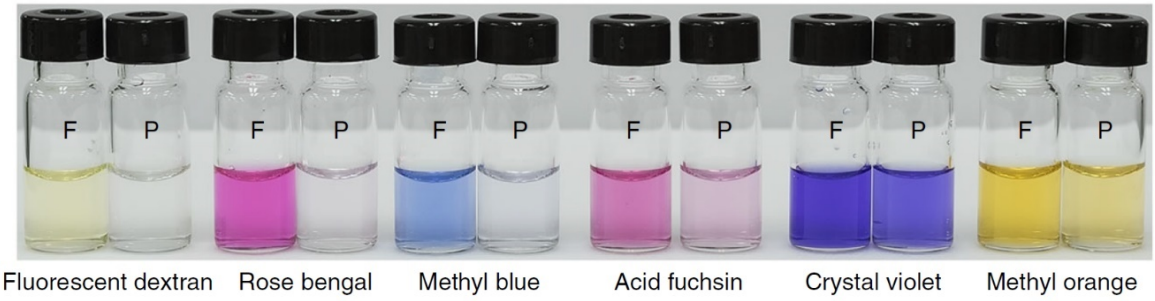

Figure 39. Photographs of feed (F) and permeate (P) containing different dye molecules (decreasing MW from left to right in image) for modified PC membranes. Both positively and negatively charged dyes had similar rejections.

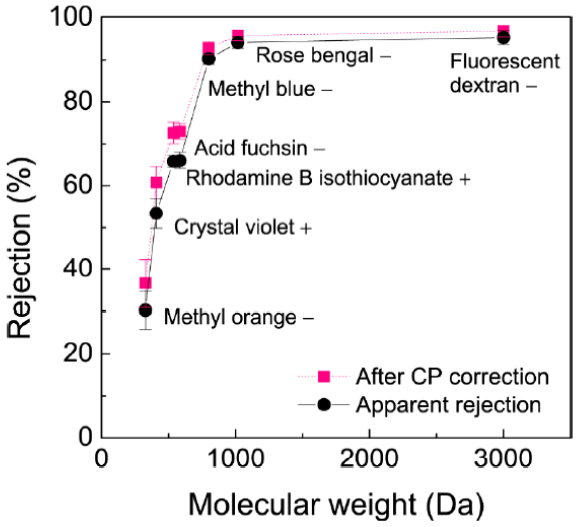

Figure 40. For PC membranes with 3-layer PAP[5] channels 2D sheet depositions, the rejection properties (both apparent rejection and the rejection after corrected by proposed concentration polarization model) showed a consistent molecular weight cutoff trend to different charged dyes. Data shown are the average of triplicate measurements with standard deviation.

A series of steered MD simulations were conducted on the selected dye molecules, Methyl Orange (MO, 328 Da) and Rose Bengal (RB, 1018 Da), to validate the experimentally observed selectivity of the channel (Figure 41). This conjecture was tested by "pulling" each molecule through the central ring of PAP for 10 times and calculating the averaged potential of mean force (PMF) as a parameter to evaluate the ability of each molecule to be transport through the channel. It was observed that MO could be pulled through the channel with relatively small values of PMF (< 100 kcal · mol^{-1}), whereas RB required significantly greater PMF values (> 1500 kcal · mol^{-1}). During steered MD simulations, the RB molecule remained stuck in the central ring until the pulling force was sufficient to deform both the molecule and PAP[5] channel central ring enough to pull the molecule through. The existence of significantly high free-energy barriers indicate that the

transport of RB would not occur naturally. This series of simulations agree well with the diameter of PAP[5] channels, earlier molecular transport studies[1], and the molecular weight cutoff experiment of channel based membranes in the filtration experiments.

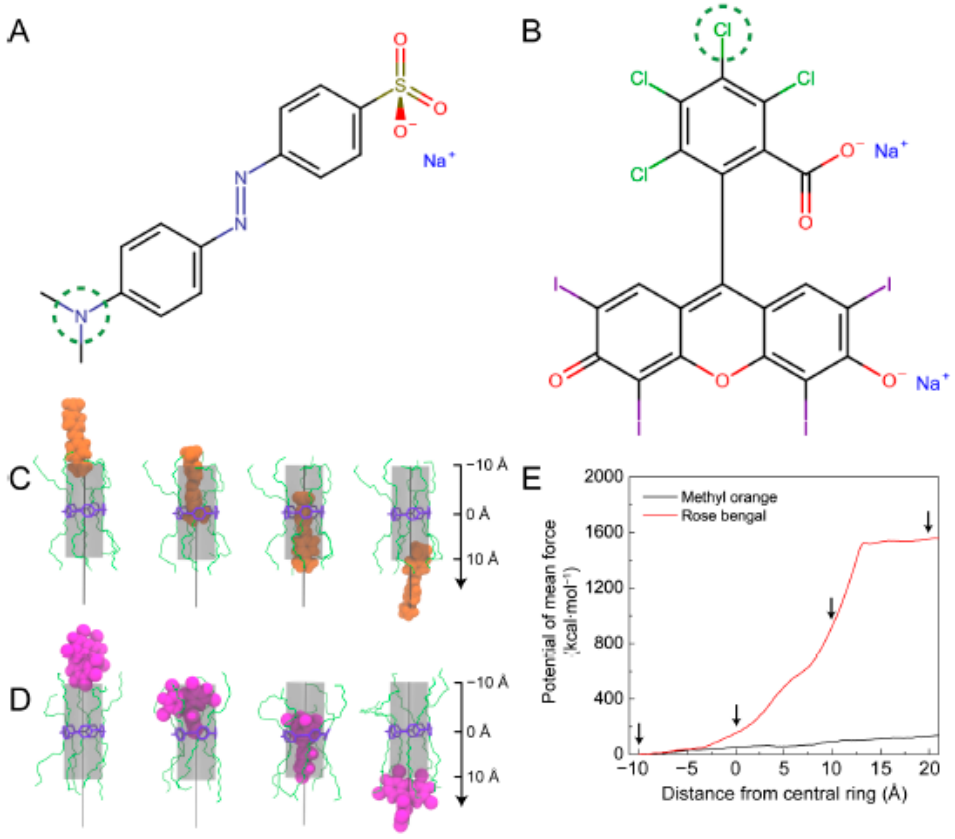

Figure 41. A series of steered molecular dynamics simulation demonstrated the rejection behavior of PAP channels. The pulled atom in each structure (A) methyl orange (MO) and (B) rose bengal (RB) is identified by a green circle. Snapshots of MO (C) and RB (D) are shown at different points during this pulling simulation. The snapshots from left to right correspond to the locations where the pulled atoms of MO and RB (as shown in panels A and B) were −10, 0, 10, and 20 Å away from the central ring of PAP channels along the pulling trajectory. (E) The potential of mean force for pulling molecules of MO and RB through PAP[5] demonstrated that MO could transport through PAP channels while BR should be rejected. The arrows correspond to the snapshots from left to right in panels C and D.

In addition, the channel-based membranes were also able effectively separate a mixture of methyl blue (800 Da) and MO (328 Da) as shown in Figure 42, while the commercial NF membranes N30F and NDX with a MWCO of 400 − 500 Da failed to achieve a clear molecular separation.

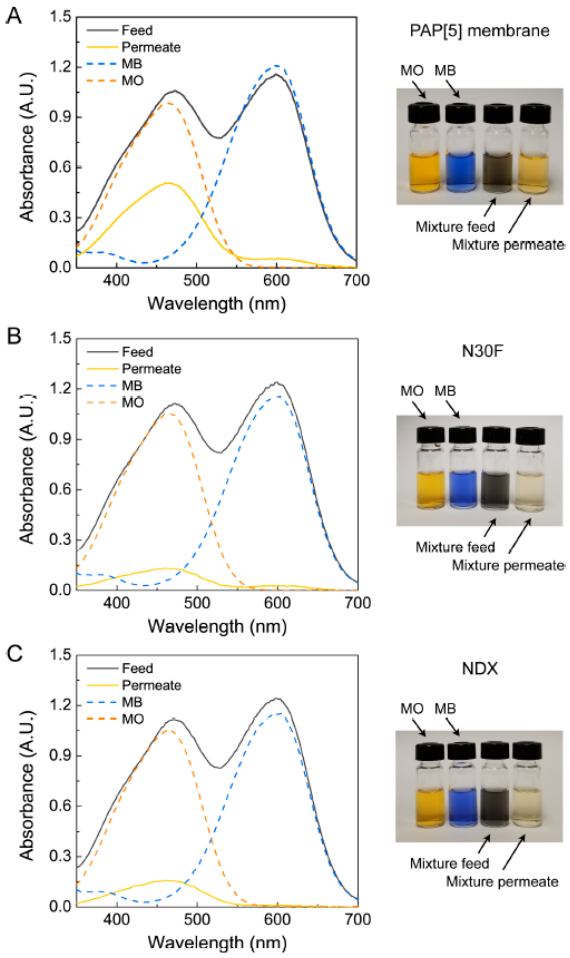

Figure 42. Mixed feed filtration experiment with feed solutions containing two dyes (methyl blue (MB), 800 Da and methyl orange (MO), 328 Da) showed complete rejection of methyl blue while showing ~50% passage of methyl orange for (A) PC membranes with 3-layer PAP[5] channels 2D sheet deposition. For commercial membranes N30F (B) and NDX (C), these membranes almost rejected both two dyes completely although their molecular weight cutoffs are 400-500 Da.

The composite membranes (especially modified PES membranes with porosity one order of magnitude higher than that of PC membranes) had a permeability of ~60 LMH/bar and a cutoff of 450 Da. In order to confirm the contribution of channels to molecular exclusion, a block copolymer control membrane was first tested without PAP[5] channels. Because the PB-PEO only forms micelles or small vesicles during aqueous based self-assembly, synthesizing a control membrane using aqueous self-assembly alone was found to be excessively difficult. As an alternative, a solvent casting method was adopted to fabricate a control membrane fully made out of block copolymers. The control membrane displayed a low permeability (~0.1 LMH/bar), and almost complete rejection (~96%) of the smallest dye used in this work (MO, 328 Da). This indicates that the high water transport permeability and the MWCO of ~500 Da are attributed primarily to the transport characteristics of the PAP[5] channels, and not from the BCPs themselves. Second, the d-spacing between laminar 2D sheets was determined by X-ray diffraction as conducted in similar studies for laminar graphene oxide membranes [19]. This d-spacing was found to be 1.5 nm (Figure 43) for wet membranes, a spacing that is expected to allow a globular molecule of ~1 kDa to be accommodated [20]. This result indicates that the rejection from our membranes was mainly contributed by normal flow through PAP[5] channels within these 2D sheets rather than the lateral flow observed between two sheets and then transverse flow between the sheets as in laminar graphene oxide and graphene membranes [21].

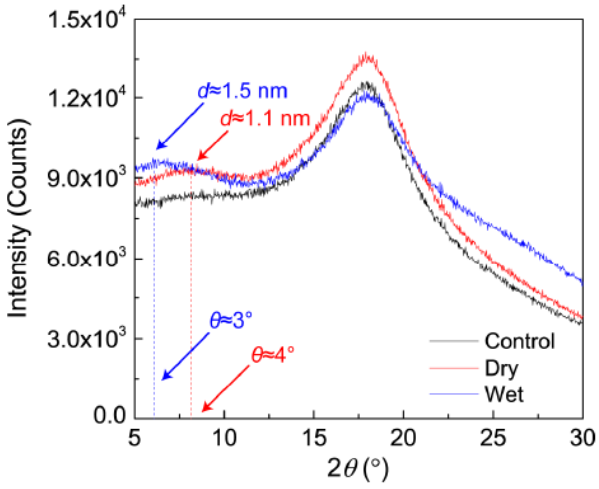

Figure 43. X-ray diffraction patterns of control PES membrane, dry PAP[5] 2D nanosheet based membrane, and wet PAP[5] 2D nanosheet based membrane.

The permeability values measured for the composite membranes were of the same order of magnitude as the values calculated from osmotic permeability measurements from stopped-flow experiments, with the measured permeability of composite membranes ~2 – 3 times larger. Given the uncertainties and differences in testing at these two very different scales (nm^2 vs cm^2 scale) and techniques (osmotic shock vs. pressure driven flow), of which agreement is considered as excellent. In terms of the rejection profile, the MWCO curve was sharper than those of commercial membranes (Figure 36B inlet). The obtained sigmoidal model does not completely rule out that some transport could occur through channels or defects of sizes different than the 5 Å pore size of the channels across these composite membranes but nevertheless indicates excellent performance of these first generation membranes. Possible defect mechanisms may include transport through the interlayer of the layer-by-layer structure, leakage through gaps between the block copolymer and the channels, diffusion through the block copolymer matrix itself, and leakage through uncovered substrate pores. During our fabrication, it was tried to minimize

any leakage with our best ability. The *d*-spacing analysis demonstrated the rejection was mainly from the normal flow through PAP[5] pores, but the lateral flow between layers could still have contributed to the overall flow. Also, a method of multiple layer-by-layer depositions and post chemical crosslinking to enhance the membrane integrity was performed. In the long term, a fully cross-linked polymer matrix with better physical and chemical compatibility with channels is desired, and the fabrication process could be further optimized. However, owing to our ability to generate close to defect-free composite membranes, the permeability of the current PAP[5] channel-based membrane is several times higher than current commercial nanofiltration and ultrafiltration membranes with MWCOs from 200 Da to 1 kDa, and its molecular separation was also demonstrated to be significantly enhanced over that of those commercial NF membranes as seen from example dye mixture separation experiments (Figure 42).

2.4.2. SEPARATION MECHANISMS OF THE PAP[5] BASED MEMBRANE; SIZE EXCLUSION VS. ELECTROSTATIC INTERACTION

PAP[5] membranes showed a MWCO of 500 Da in good agreement with single channels' size-exclusive selectivity that was estimated from stopped-flow experiments (~420 Da) [1], which was evaluated by pressure driven filtration experiments of organic dyes with various molecular weights. However, regarding this result, an important question to address was whether the molecular selectivity originates from size exclusion of channels or electrostatic interactions between solutes and layered membrane structures, because most water-soluble organic dyes are charged.

To identify the PAP[5] membranes' exclusion mechanism, dye rejection tests were carried out under various ionic strength environments. If the electrostatic interactions are

the main mechanism for exclusions, the rejections would be severely affected by the ionic strength of the solution due to the electrostatic screening effect [22]. For this experiment, methyl blue (MB) was chosen as a subject solute owing to the similarity in its molecular weight (~750 Da) to the membrane's MWCO (~500 Da). The ionic strength of the feed solution was adjusted from 0.035 to 200 mM using sodium chloride (NaCl). The PAP[5] membranes did not show a significant rejection decrease at the highest ionic strength condition, maintaining more than 85% of dye rejection (Figure 44A). Also, this result indicates that the rejections are independent of the Debye length (λ_D) of the ionic solutions (Figure 44B). λ_D is a parameter that describes how far electrolytes' electrostatic effects can be sustained from the subjects' surfaces in electrolyte solutions. Using this property, Fornasiero *et al.* studied the relationship between λ_D and the ion exclusion behavior of electrochemically modified carbon nanotube membranes, and it was demonstrated that the solute rejections almost disappear as λ_D becomes close to the pore diameter, if charged species exclusion occurs mostly by electrostatic interactions [22]. In the case of PAP[5] membranes, λ_D was 0.48 nm for the 200mM ionic strength condition, which is comparable to the pore size of the PAP[5] channel (~0.5 nm). Nonetheless, the dyes were effectively excluded by the PAP[5] membranes even under these conditions (Figure 44B), implying that the electrostatic interactions did not play a significant role in the selective properties of the ML-PAP[5] membranes for the macromolecular dyes, which had been used for estimating the MWCO. Consequently, the size dependent exclusion is the dominant factor for this membrane at these molecular scales.

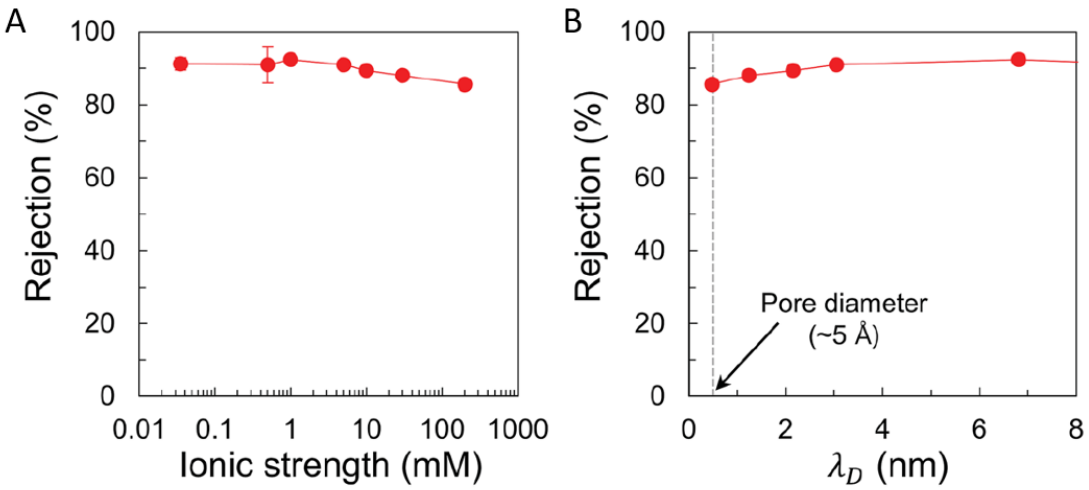

Figure 44. Methyl blue dye rejection as a function of (A) ionic strength and corresponding (B) Debye screening length (λ_D, nm) of the solution. Methyl blue dyes were selected as a subject solute due to their comparable molecular weight (~750 Da) to the MWCO of the membranes (~500 Da). The ionic strength of the solutions was adjusted using NaCl. Small error bars (smaller than 1%, n = 3) are not shown for clarity except for 0.5 mM in (A).

2.4.3. POINT-CHARGED ION EXCLUSION BY THE PAP[5] MEMBRANES

Ion exclusion by the PAP[5] membranes at low ionic strengths was also studied to understand how electrostatic layered structures affect the ion exclusion properties, especially in low ionic concentration environments. Note that no significant ionic exclusion was shown at ionic strengths greater than 35 mM, which are similar to standard conditions for testing conventional nanofiltration (NF) or reverse osmosis (RO) membranes, due to the large pore size of the channels compared to ionic species.

Ion exclusion via electrostatic interactions between ions and charged membranes has been well described by the Donnan exclusion effect [23]. This theory describes the electrochemical solute behavior at the interface of charged membranes and ionic solutions. In general, the charged membrane builds opposite charge gradients over the membrane

surface and presents electrostatic potentials from the membrane surface to the bulk phase of the ionic solution, which is called the Donnan potential [22, 23, 24]. As a result, under pressure driven filtration, some ions cannot overcome this potential resulting in ionic exclusion. Also, the counter ions will potentially be rejected at the same time, if they cannot compensate for the energy requirement, which is needed to separate the ion pairs. The rejection coefficient resulting from Donnan exclusion is described by the following Equation (2.10).

$$R = 1 - \left(\frac{|z_i|c_i}{|z_i|{c_i}^m + {c_x}^m}\right)^{|z_i/z_j|} \tag{2.10}$$

where c_i and ${c_m}^i$ are the co-ion (same charge ions with membrane) concentrations of the solution and membrane, ${c_m}^x$ is the charge concentration of the membrane, i and j represent the opposite charge signs, and z is the ionic valence number. ${c_m}^i$ is generally adapted as the co-ion concentration of the permeate solution [25].

From the structural point of view, the selective layer of the PAP[5] membranes have two oppositely charged layers, which can be effective for ionic exclusion; one is the channel-based nanosheet layer which is negatively charged and the other is the positively charged PEI layer. The nanosheet layers are highly functionalized with –COOH reactive groups on both the channel entrances and PEO ends of block copolymers, representing the negatively charged layers. Whereas the PEI polymers possess a number of primary amine groups, which result in positive charges at circumneutral pH. Both reactive groups were introduced to be crosslinked with each other to confer enough mechanical stability onto the entire selective layer. However, this resulted in charged layer-by-layer structures.

To understand whether the PAP[5] membrane has ionic selectivity at low ionic strength and, if it does, what charge interactions are responsible for the electrostatic exclusion, several salts with different ionic valence ratios were tested and the rejection trend was compared with that predicted by the Donnan equilibrium Equation (2.10). The ionic exclusion measurement showed a trend of increasing rejection along with the increasing ratios of positive to negative valence numbers (Figure 45A), indicating that positively charged layers are responsible for the ionic rejections. This result is counter-intuitive as the outermost top layer of the PAP[5] membrane is composed of negatively charged nanosheets and the expectation was that this top layer would have dominant impact on the observed ionic rejection trends. However, this result suggested that, even though the electrostatic potential can be constructed by both PEI and nanosheet layers, the net surface potential is dominated by positively charged PEI layers and results in multi-valent anionic selectivity (Figure 46A). It was confirmed by conducting surface zeta-potential (ξ, mV) measurements of the PAP[5] membranes (Figure 46B and Figure 46C), which indicated that the PAP[5] membranes have a positive zeta potential, despite the presence of the outermost layer of negatively charged PAP[5] nanosheets.

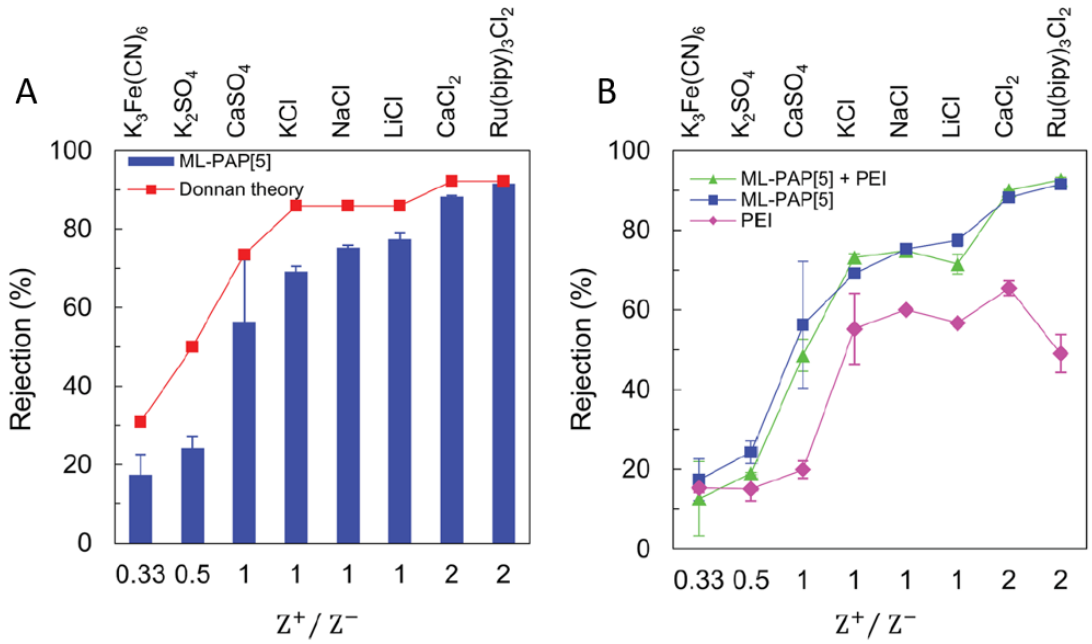

Figure 45. Point-charged ion rejection tests indicate the presence of a positively charged discriminating layer on the membrane. Z^+ and Z^- are the ionic valence numbers of the positively and negatively charged ions, respectively. (A) Ion rejection results of the PAP[5] membranes along with various valence ratios of positively to negatively charged ions. Theoretical Donnan rejections were calculated using Equation (2.10). The membrane charge was estimated as 3.5 mM, obtained by fitting the experimental rejection data of $Ru(bipy)_3Cl_2$ salts into Equation (2.10). (B) Ionic rejection trends of the support membrane with only a PEI layer (PEI), the PAP[5] membrane (ML-PAP[5]), and the PAP[5] membrane with an additional PEI layer on the top (ML-PAP[5] + PEI). $K_3Fe(CN)_6$; potassium ferricyanide, K_2SO_4; potassium sulfate, $CaSO_4$; calcium sulfate, KCl; potassium chloride, NaCl; sodium chloride, LiCl; lithium chloride, $CaCl_2$; calcium chloride, and $Ru(bipy)_3Cl_2$; tris(bipyridine)ruthenium(III) chloride.

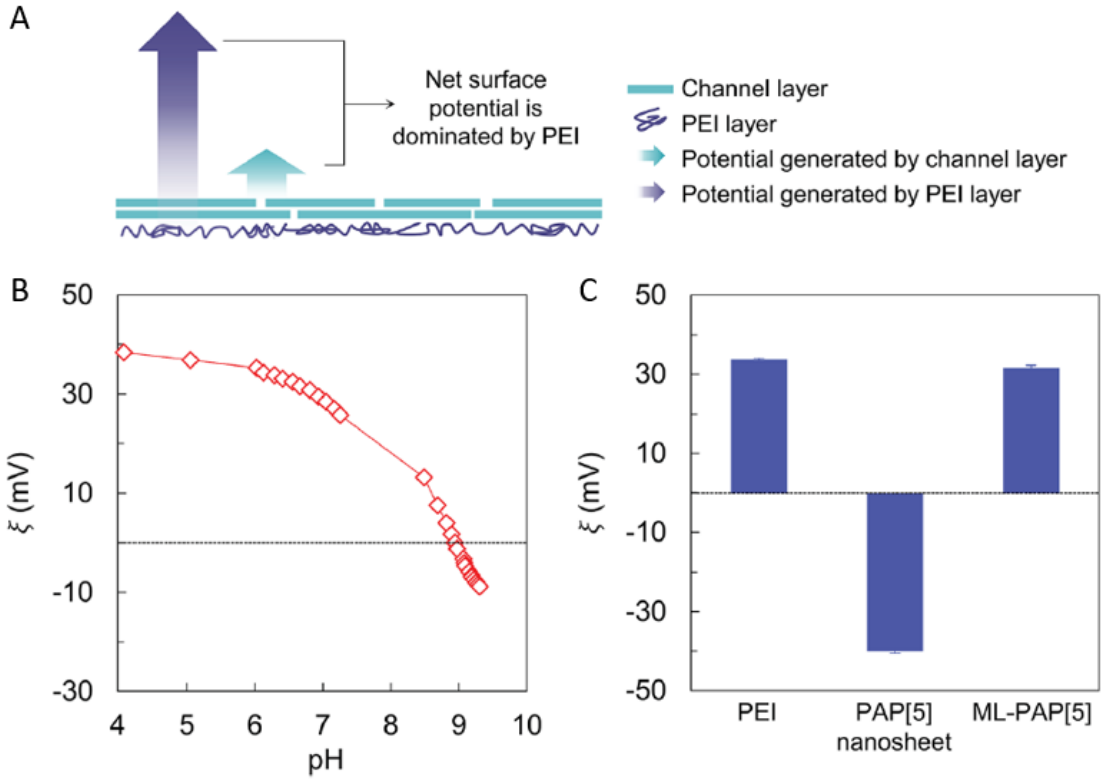

Figure 46. Zeta potential measurements confirm that the surface potential of the PAP[5] membranes is dominated by the positively charged PEI layers. (A) Schematic illustration for the surface charge of PAP[5] membranes. (B) Zeta potential (ξ, mV) measurements of the PAP[5] membranes were conducted over a wide range of pH values. These indicated that the isoelectric point was located around pH 9, indicating positively charged surface behavior of the PAP[5] membranes around circumneutral pH environments. (C) Zeta potentials of the membrane with only a PEI layer (PEI), the membrane with only a PAP[5] nanosheet layer (PAP[5] nanosheet), and the PAP[5] membrane (ML-PAP[5]) at pH 6.5, which is representative of filtration testing conditions.

To further verify that the PEI layers were indeed responsible for cation selectivity under low ionic concentrations, the support polycarbonate membranes with only PEI layers were also tested for ionic salt rejections (Figure 45B). In spite of the large pore size of the support membrane (50 nm), they showed 60 – 80% ion exclusion compared to the PAP[5] membranes. Also, the ML-PAP[5] membranes with an additional PEI layer on the top

showed similar ion rejection trends to the ML-PAP[5] membranes, indicating the large impact of the PEI layers in terms of ion rejection rather than the PAP[5] channel layers. Theoretical ionic rejections were calculated using Equation (2.10) and compared with the experimental results. The charge concentration of the membrane (c_x^m) is estimated as 3.5 mM by fitting the experimental rejection data of tris(bipyridine)ruthenium(III)chloride ($Ru(bipy)_3Cl_2$) into Equation (2.10). As expected, the theoretical Donnan rejections showed good agreement with the experimental values (Fig. 3A).

2.4.4. LINEAR MOLECULE PASSAGE THROUGH A CYLINDRICAL PORE VIA ELONGATIONAL FLOW

Linear and flexible polymer chains have been known to permeate through cylindrical or conical pores that are much smaller than the expected polymer dimensions in aqueous solutions [26, 27, 28, 29]. This passage phenomenon has been explored in a number of studies and has implications in fields ranging from polymer physics to practical downstream membrane bioseparations [30, 31, 32, 33, 34, 35]. The phenomenon of linear molecule flow through small pores is based on polymer deformation, which is accompanied by elongational flow of the solvent, leading to polymers' entrance into pores. Flexible polymers in the dilute regime (when the polymer concentration is less than the chain overlap concentration) maintain thermodynamically stable conformations, and this results in globular (folded chain) shapes with predictable radii of gyration (R_g). Thus, from the geometric perspective, if the R_g value is larger than the radius of the pores (R_p), polymers are not able to flow through the pores. However, many empirical experiments have shown that under certain conditions, linear polymers can flow through the pores even though the R_p is substantially smaller than R_g. Specifically, under the filtration environment, when the polymers get closer to the pore entrances along with the solvent flow, two compensating

factors compete with each other resulting in the final polymer conformation that dictates whether the polymer enters and passes through the pores (Figure 47). One is elongational shear stress (stretching force) and the other is polymer relaxation (restoration force). The shear force originates from convergent flow of the solvent near the pore entrance, while polymer relaxation is a result of Brownian fluctuations of the polymers. If the polymers can be stretched out as a result of the shear rate overcoming the relaxation force, then they can flow through the pores; this polymer deformation phenomenon is called affine [36]. In the opposite situation where the shear rate cannot overcome the relaxation force, the polymers exist as thermodynamically stable globule shapes and cannot pass through the pores. With respect to this phenomenon, the critical shear rate (S_c) has been described as Equation (2.11).

$$S_c \cong {\tau_z}^{-1} \cong \frac{k_B T}{\eta {R_g}^3} \tag{2.11}$$

where τ_z is the Zimm relaxation time of the polymers, k_B is the Boltzmann constant, T is the absolute temperature and η is the viscosity of the solution [36]. Daoudi and Brochard correlated this equation with membrane performances and suggested a critical flux (J_c) equation, which describes the minimum hydraulic flux to attain S_c that allows for entrance of the polymers into the pore along with solvent flow as in Equation (2.12) [27].

$$J_c = \frac{k_B T}{\eta} \tag{2.12}$$

Although this equation is based on a number of assumptions, such as perfectly circular and uniform pore shapes, and no interferences in convergent flows between

neighboring pores, this critical flux equation has led to many other derived critical flux equations that are reasonably applicable in various membrane applications. Furthermore, the work by Daoudi and Brochard suggests that any flexible linear polymer chain in the dilute regime, no matter the molecular weight, such as poly(ethyleneoxide) (PEO), will pass through a cylindrical pore when the elongational shear reaches a critical value. For the stated reasons, it is highly possible for linear polymer chains to pass through the PAP[5] channels, as will be described within the following section.

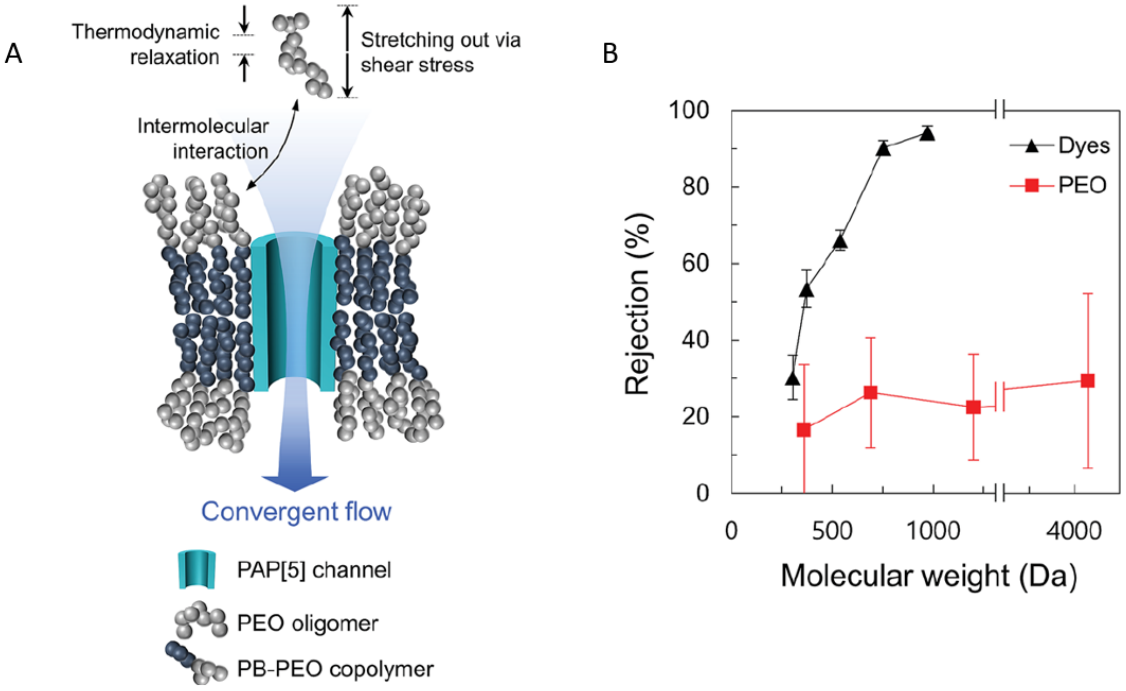

Figure 47. Several factors lead to the passage of large MW linear PEO molecules through the straight through pore of the PAP[5] membranes. (A) Schematic illustration of possible factors for PEO polymer deformation, entering into a cylindrical PAP[5] water channel. (B) PAP[5] membranes' rejection results for globular dyes and linear PEO polymers with a wide molecular weight range.

2.4.5. PEO TRANSMISSION ACROSS THE PAP[5] MEMBRANES THROUGH PAP[5] CHANNELS' STRAIGHT THROUGH PORES

The ML-PAP[5] membranes were tested with PEO polymers to confirm that the molecular sieving effect of the ML-PAP[5] membranes is irrespective of charge effects. However, repeated experiments revealed that PEO polymers of sizes several times larger than the determined exclusion limit of the membrane (500 Da) could not be substantially rejected by the ML-PAP[5] membranes, regardless of the wide range of oligomer molecular weights (Figure 47B). Contrary to the channel-based membranes, current nanofiltration membranes with similar MWCOs to the ML-PAP membranes have an active layer, which is commonly considered nonporous and is expected to have voids that are only connected transiently due to thermal motion of the polymers. For these membranes, the use of linear molecules, such as PEO and poly(propylene oxide), seems to work well, and is an established standard in many protocols for MWCO determination [37, 38]. On the other hand, channel-based PAP[5] membranes have cylindrical, straight through pores spanning the entire selective layer. Thus, considering the PEO's flexibility as well as linearity, it was hypothesized that linear molecule transmission could be a distinctive property of channel-based membranes, which has been mostly seen in ultrafiltration membrane applications up to date. To rationally presume the possibility of this hypothesis, the theoretical critical flux (J_c) was calculated (Appendix B), and then compared with the actual experimental water flux. However, the experimental water flux (0.223 mol $\cdot$ m^{-2} $\cdot$ s^{-1}) was significantly lower than the theoretical critical flux (296,000 mol $\cdot$ m^{-2} $\cdot$ s^{-1}), implying that the PEO molecules cannot be sufficiently stretched out under this experimental (hydraulic flux) condition and cannot pass through the channel pores.

Another possible hypothesis that could explain PEO transmission through the ML-PAP[5] membrane is to consider possible mutual interactions between PEO oligomers and

the PAP[5] membrane matrix. As shown in Figure 47A, the PAP[5] water channels are structurally supported by PB-PEO block copolymers. Consequently, very dense PEO brushes face the feed solution side and surround the channel entrances. Therefore, it would be worthwhile to consider potential intermolecular interactions between PEO oligomers and the PEO matrix, which can have an influence on the observed PEO passage trends. Most current elongational flow models do not consider the effect of intermolecular interactions on polymer deformations as most practical membrane applications involve operations at dilute polymer concentrations. However, in the case of semi-diluted or highly concentrated polymer solutions, intermolecular interactions could result in a significant effect on polymer deformation and passage through the pore [27, 29]. For example, if the polymer coils are overlapped with each other in concentrated environments, the polymer relaxation time (τ_z) would be greater than that of diluted polymers due to the steric hindrance of very closely spaced polymers and this would result in a significantly reduced critical shear rate of the polymers (see Equation (2.11)). Based on this approach, Brochard and Neel suggested a corrected critical flux equation (J_c^*) for concentrated polymer solutions (2.12).

$$J_c^* = \frac{k_B T}{\eta}\left(\frac{C^*}{C}\right)^{\frac{15}{4}} \tag{2.12}$$

where C^* and C are the polymer overlap concentration and polymer concentration in the feed solution, respectively. This equation indicates that if the polymer concentration is higher than the corresponding polymers' overlap concentration, the polymers can suffer chain deformation much more easily even under the mild shear stress environments with dramatically lowered critical flux. Based on this approach, it is hypothesized that when

PEO polymer chains get closer to PEO brushes along with convergent flow of water, they can be easily stretched out owing to the surrounding dense PEO brushes and are able to pass through the channel pores with water flow. However, since there are a number of assumptions inherent to the current analyses, further studies will be needed to confirm the proposed hypothesis.

Chapter 2.5: Conclusion

A completely synthetic biomimetic membrane that consists of densely packed PAP artificial water channels have been fabricated. The resulting membrane maintained high permeability and, more importantly, maintained selectivity expected from the molecular design of these PAP[5] artificial water channels. Also, several unique selectivity trends were observed for this new class of synthetic membranes. This characteristic ion selectivity trend at low ionic strengths is attributed to the membrane structure rather than to the channel's characteristics. These results suggest several new aspects that need to be considered in designing practical channel-based membranes. During the last few years, the relationships between channels and their molecular transport behaviors have been carefully studied, however, only the importance of the channels' properties has been emphasized in most cases. An emerging emphasis of current channel research is on synthesizing practical membranes, therefore, it would be worthwhile to consider the channel-based membranes more systemically, from the unitary properties of the channels to the entire membrane system. In addition, due to the intrinsic cylinder like pore structures of water channels, the transport phenomenon is difficult to anticipate just based on the consideration of transport in current polymeric membranes. Therefore, addressing this knowledge gap would be

necessary to fully understand the potential advantages and drawbacks of channel-based membranes for future applications.

REFERENCES

[1] Shen, Y.-x., Si, W., Erbakan, M., Decker, K., De Zorzi, R., Saboe, P.O., Kang, Y.J., Majd, S., Butler, P.J., Walz, T., Aksimentiev, A., Hou, J.-l., Kumar, M., Highly permeable artificial water channels that can self-assemble into two-dimensional arrays, Proceedings of the National Academy of Sciences, USA 112(32) (2015) 9810-9815.

[2] Discher, D.E., Eisenberg, A., Polymer Vesicles, Science 297(5583) (2002) 967-973.

[3] Mai, Y., Eisenberg, A., Self-assembly of block copolymers, Chemical Society Reviews 41(18) (2012) 5969-5985.

[4] Rakhmatullina, E., Meier, W., Solid-Supported Block Copolymer Membranes through Interfacial Adsorption of Charged Block Copolymer Vesicles, Langmuir 24(12) (2008) 6254-6261.

[5] Kumar, M., Habel, J.E.O., Shen, Y.-x., Meier, W.P., Walz, T., High-Density Reconstitution of Functional Water Channels into Vesicular and Planar Block Copolymer Membranes, Journal of the American Chemical Society 134(45) (2012) 18631-18637.

[6] Klara, S.S., Saboe, P.O., Sines, I.T., Babaei, M., Chiu, P.-L., DeZorzi, R., Dayal, K., Walz, T., Kumar, M., Mauter, M.S., Magnetically Directed Two-Dimensional Crystallization of OmpF Membrane Proteins in Block Copolymers, Journal of the American Chemical Society 138(1) (2016) 28-31.

[7] Shen, Y.-x., Song, W., Barden, D.R., Ren, T., Lang, C., Feroz, H., Henderson, C.B., Saboe, P.O., Tsai, D., Yan, H., Butler, P.J., Bazan, G.C., Phillip, W.A., Hickey, R.J., Cremer, P.S., Vashisth, H., Kumar, M., Achieving high permeability and enhanced selectivity for Angstrom-scale separations using artificial water channel membranes, Nature Communications 9(1) (2018) 2294.

[8] Zydney, A.L., Stagnant film model for concentration polarization in membrane systems, Journal of Membrane Science 130(1) (1997) 275-281.

[9] Feroz, H., Vandervelden, C., Ikwuagwu, B., Ferlez, B., Baker, C.S., Lugar, D.J., Grzelakowski, M., Golbeck, J.H., Zydney, A.L., Kumar, M., Concentrating membrane proteins using ultrafiltration without concentrating detergents, Biotechnology and Bioengineering 113(10) (2016) 2122-2130.

[10] Colton, C.K., Smith, K.A., Mass transfer to a rotating fluid. Part II. Transport from the base of an agitated cylindrical tank, AIChE Journal 18(5) (1972) 958-967.

[11] Koutsou, C.P., Karabelas, A.J., Shear stresses and mass transfer at the base of a stirred filtration cell and corresponding conditions in narrow channels with spacers, Journal of Membrane Science 399-400 (2012) 60-72.

[12] Erickson, H.P., Size and Shape of Protein Molecules at the Nanometer Level Determined by Sedimentation, Gel Filtration, and Electron Microscopy, Biological Procedures Online 11(1) (2009) 32.

[13] Dean, D.C., O'Muircheartaigh, J., Dirks, H., Waskiewicz, N., Lehman, K., Walker, L., Han, M., Deoni, S.C.L., Modeling healthy male white matter and myelin development: 3 through 60months of age, NeuroImage 84 (2014) 742-752.

[14] Rathee, V.S., Qu, S., Phillip, W.A., Whitmer, J.K., A coarse-grained thermodynamic model for the predictive engineering of valence-selective membranes, Molecular Systems Design & Engineering 1(3) (2016) 301-312.

[15] Kim, S., Lee, J., Jo, S., Brooks III, C.L., Lee, H.S., Im, W., CHARMM-GUI ligand reader and modeler for CHARMM force field generation of small molecules, Journal of Computational Chemistry 38(21) (2017) 1879-1886.

[16] Rajesh, S., Yan, Y., Chang, H.-C., Gao, H., Phillip, W.A., Mixed Mosaic Membranes Prepared by Layer-by-Layer Assembly for Ionic Separations, ACS Nano 8(12) (2014) 12338-12345.

[17] Tang, H., Ji, S., Gong, L., Guo, H., Zhang, G., Tubular ceramic-based multilayer separation membranes using spray layer-by-layer assembly, Polymer Chemistry 4(23) (2013) 5621-5628.

[18] Boussu, K., Van der Bruggen, B., Volodin, A., Van Haesendonck, C., Delcour, J.A., Van der Meeren, P., Vandecasteele, C., Characterization of commercial nanofiltration membranes and comparison with self-made polyethersulfone membranes, Desalination 191(1) (2006) 245-253.

[19] Mo, Y., Zhao, X., Shen, Y.-x., Cation-dependent structural instability of graphene oxide membranes and its effect on membrane separation performance, Desalination 399 (2016) 40-46.

[20] Zhao, X., Bu, X., Wu, T., Zheng, S.-T., Wang, L., Feng, P., Selective anion exchange with nanogated isoreticular positive metal-organic frameworks, Nature Communications 4(1) (2013) 2344.

[21] Abraham, J., Vasu, K.S., Williams, C.D., Gopinadhan, K., Su, Y., Cherian, C.T., Dix, J., Prestat, E., Haigh, S.J., Grigorieva, I.V., Carbone, P., Geim, A.K., Nair, R.R., Tunable sieving of ions using graphene oxide membranes, Nature Nanotechnology 12(6) (2017) 546-550.

[22] Fornasiero, F., Park, H.G., Holt, J.K., Stadermann, M., Grigoropoulos, C.P., Noy, A., Bakajin, O., Ion exclusion by sub-2-nm carbon nanotube pores, Proceedings of the National Academy of Sciences 105(45) (2008) 17250-17255.

[23] Donnan, F.G., The Theory of Membrane Equilibria, Chemical Reviews 1(1) (1924) 73-90.

[24] Ohshima, H., Ohki, S., Donnan potential and surface potential of a charged membrane, Biophysical journal 47(5) (1985) 673-678.

[25] Schaep, J., Van der Bruggen, B., Vandecasteele, C., Wilms, D., Influence of ion size and charge in nanofiltration, Separation and Purification Technology 14(1) (1998) 155-162.

[26] Kremer, K., Binder, K., Dynamics of polymer chains confined into tubes: Scaling theory and Monte Carlo simulations, The Journal of Chemical Physics 81(12) (1984) 6381-6394.

[27] Daoudi, S., Brochard, F., Flows of Flexible Polymer Solutions in Pores, Macromolecules 11(4) (1978) 751-758.

[28] Long, T.D., Anderson, J.L., Flow-dependent rejection of polystyrene from microporous membranes, Journal of Polymer Science: Polymer Physics Edition 22(7) (1984) 1261-1281.

[29] Nguyen, Q.T., Neel, J., Characterization of ultrafiltration membranes.: Part IV. Influence of the deformation of macromolecular solutes on the transport through ultrafiltration membranes, Journal of Membrane Science 14(2) (1983) 111-127.

[30] Latulippe, D.R., Zydney, A.L., Elongational flow model for transmission of supercoiled plasmid DNA during membrane ultrafiltration, Journal of Membrane Science 329(1) (2009) 201-208.

[31] Latulippe, D.R., Ager, K., Zydney, A.L., Flux-dependent transmission of supercoiled plasmid DNA through ultrafiltration membranes, Journal of Membrane Science 294(1) (2007) 169-177.

[32] Hancher, C.W., Ryon, A.D., Evaluation of ultrafiltration membranes with biological macromolecules, Biotechnology and Bioengineering 15(4) (1973) 677-692.

[33] Hirasaki, T., Sato, T., Tsuboi, T., Nakano, H., Noda, T., Kono, A., Yamaguchi, K., Imada, K., Yamamoto, N., Murakami, H., Manabe, S.-i., Permeation mechanism of DNA molecules in solution through cuprammonium regenerated cellulose hollow fiber (BMMtm), Journal of Membrane Science 106(1) (1995) 123-129.

[34] Higuchi, A., Kato, K., Hara, M., Sato, T., Ishikawa, G., Nakano, H., Satoh, S., Manabe, S.-i., Rejection of single stranded and double stranded DNA by porous hollow fiber membranes, Journal of Membrane Science 116(2) (1996) 191-197.

[35] Kahn, D.W., Butler, M.D., Cohen, D.L., Gordon, M., Kahn, J.W., Winkler, M.E., Purification of plasmid DNA by tangential flow filtration, Biotechnology and Bioengineering 69(1) (2000) 101-106.

[36] Hinch, E.J., Mechanical models of dilute polymer solutions in strong flows, The Physics of Fluids 20(10) (1977) S22-S30.

[37] Xu, L., Shahid, S., Shen, J., Emanuelsson, E.A.C., Patterson, D.A., A wide range and high resolution one-filtration molecular weight cut-off method for aqueous based nanofiltration and ultrafiltration membranes, Journal of Membrane Science 525 (2017) 304-311.

[38] Rohani, R., Hyland, M., Patterson, D., A refined one-filtration method for aqueous based nanofiltration and ultrafiltration membrane molecular weight cut-off determination using polyethylene glycols, Journal of Membrane Science 382(1) (2011) 278-290.

SECTION 3: TRANSFORMING ARTIFICIAL CHANNELS TO THIN-FILM COMPOSITE GAS SEPARATION MEMBRANES

Chapter 3.1: Abstract

Membrane gas separations are an attractive technology that is expected to reduce global energy consumption caused by thermal separation processes. Developments of new membrane materials have been proposed but have not been entirely successful for large scale applications during last three decades. Based on the lessons learnt from the past, major challenges at the stage of material developments have been pointed out as controlling the rigid microstructures (improving internal homogeneity), processing into thin-film formats, and maintaining good mechanical stability to avoid plasticization or physical aging. Here, bearing these concepts in mind, thin film composite membranes were prepared using interfacial polymerization of pillar[5]arene macrocycles. This methodology was inspired by the molecular structure of peptide-appended pillar[5]arene artificial water channel discussed in SECTION 2, envisioning the developments of viable membranes for gas separations. As a result, pillar[5]arene macrocycles were incorporated into a few micron-thick polymer films with volume fractions up to ~48 %, thus increasing molecular sieving effects of TFC membranes. It is postulated that such an enhancement is attributed to the improved nanoscale homogeneity of the polymer membranes, thanks to the pillar[5]arenes that possess 4.7 Å cavity that function as ultramicropores (< 7Å in diameter) for molecular differentiation. In addition, since the membranes were developed using interfacial polymerization technique which is one of the most successful membrane platforms in the market, the proposed membranes offer good opportunities to be adopted for large scale applications, alongside the other features such as highly crosslinked structures (good mechanical stability) and cost efficiency (~10 $/m^2 of the membranes).

Chapter 3.2: Introduction

Membrane technology is expected to bring significant energy saving for industrial gas and vapor separations. Membrane processes typically do not require phase change for molecular separations and, therefore, are more energy efficient and environmentally friendly compared to thermal processes such as distillation [1, 2, 3, 4, 5]. Alongside the rapid growth of membrane markets during the last three decades, a great number of membrane materials has been newly developed every year, but still limited number of polymers are used in large scale membrane applications [3, 4]. A broad perspective of scalability just rather than permeability and selectivity has been proposed for the development of new membranes to bridge the gaps between laboratories and large-scale applications. In terms of materials' features, this could be summarized as (1) capability of processing the materials into thin-film or thin selective layer formats at large scale to meet the desirable productivity of membrane skids, and (2) securing mechanical stability of the membranes to avoid structural deformation at molecular level due to plasticization or physical aging.

To help satisfy these requirements, thin-film composite (TFC) membranes were prepared by interfacial polymerization of pillar[5]arene macrocycles. This attempt originates from the efforts to simplify the structural complexity of the channel-based membranes and to improve the processability that are relevant to industrial scale membrane production (Figure 48). TFC membranes are one of the most successful membrane platforms that has been implemented in seawater desalination and other water treatment plants at the large scale of hundreds of millions of gallons per day [6, 7, 8]. While the TFC membranes have not extensively used in gas separations, these membranes have prospective properties to resolve the abovementioned challenges [9]. First, since the

selective layers are formed at the interface of two immiscible phases, the thickness of selective layers is inherently limited to the sub- or few-microns scale. Also, these polymers are highly crosslinked. Recent studies on linear glassy polymers such as polyimides has implied that it would be difficult to significantly improve the membrane selectivity of condensable gas pairs such as CO_2/CH_4 simply by optimizing the chemistry of linear polymers [4, 10]. From this perspective, the TFC membranes eliminate the necessities of additional steps such as post-crosslinking to secure mechanical stability of the membranes and, thereby, maintain separation properties even under the exposure to condensable gases.

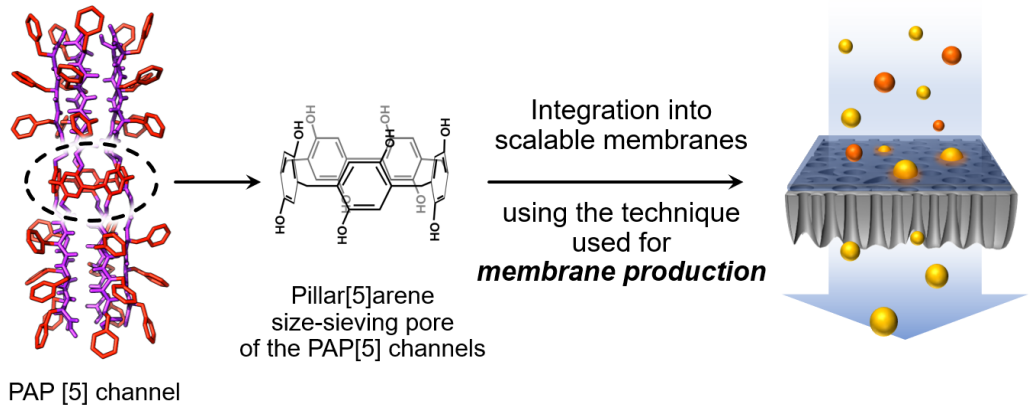

Figure 48. Schematic figure to illustrate the concept of incorporating bioinspired channels into the membranes that are capable of large-scale production.

Chapter 3.3: Materials and Experimental Methods

3.3.1. TFC MEMBRANE FABRICATION USING INTERFACIAL POLYMERIZATION

The TFC membranes were synthesized using the interfacial polymerization technique that are available elsewhere [11, 12]. In brief, Microdyn Nadir MP-005 poly(ether sulfone) ultrafiltration membranes (PES) were purchased and used as porous

support membranes for the TFC membrane fabrication. Before polymerization, the PES membranes were immersed in distilled water and washed for 24 hours changing water several times to remove membrane humectants and preserves. Pillar[5]arenes and *m*-phynylenediamine (MPD) were dissolved in water to prepare aqueous monomer solutions with different monomer concentrations (w/v %). To activate the phenolic reactive groups of pillar[5]arenes to phenoxides, 1.2 × molar excess of NaOH with respect to the number of phenolic groups were added to the solution, and the solution was filtered through 0.2 μm PTFE syringe filter to remove any dust or particulate contaminants. 1,3,5-benzenetricarbonyl trichlorides (trimesoyl chloride, TMC) were dissolved in anhydrous hexane to prepare organic phase monomer solutions. PES support membranes were immersed in aqueous solutions for five minutes, and then transferred on a glass plate. Excess aqueous solution on the surface of the membranes were removed using a squeegee with a silicone blade. Custom made PTFE gasket was placed on the surface of membranes and TMC solution was poured into the gasket to initiate interfacial polymerization. Reaction time for polymerization was 10 minutes unless specifically specified. Reactions were terminated by flushing the TMC solution with fresh hexane. The membranes were placed in oven at 70 °C for 10 minutes for post-baking and washed in distilled water for 24 hours. The prepared membranes were air-dried for one day, and vacuum-dried again at 150 °C for another day to remove any residual solvents (water) in the membranes. Membranes were kept in the desiccator until gas permeation experiments.

3.3.2. PURE GAS PERMEATION MEASUREMENTS

Membranes were masked with brass discs (McMaster-Carr, Cat #9011K4) and sealed with epoxy glue before pure gas permeation measurements. The diameter of brass discs was 47 mm with ~2.8 cm^2 membrane test area (0.75 inch in diameter of the central

holes) unless specifically specified. All measurements were performed at 35 °C with upstream pressures up to 30 atm using constant-volume and variable-pressure apparatus, which is equipped with a high-pressure filter holder (47 mm, HP Filter Holder, #4504700, MilliporeSigma). A 1000-psig industrial grade pressure transducer (Model STJE, Honeywell) and a 10-torr capacitance manometer (Baratron 626A, MKS) were used to monitor and record the upstream and downstream system pressures, respectively. The downstream pressure was maintained below 10 torr for the duration of gas permeation experiments.

3.3.3. SCANNING ELECTRON MICROSCOPY (SEM)

Top and cross-sectional membrane morphology was investigated using scanning electron microscopy (Quanta 650, FEI) with an accelerating voltage between 5 kV and 20 kV. Samples were coated using an EMS sputter coater with Au:Pd ratio of 60:40, and sputter time was 45 seconds. For the cross-sectional film preparation, PES support layer of TFC membranes were etched with dichloromethane and free-standing films were transferred onto alumina oxide (AO) membranes (Anodisc 0.2 μm pore size, Whatman). AO-supported films were cryo-fractured using liquid nitrogen and subjected to SEM investigation.

3.3.4. FOURIER-TRANSFORM INFRARED (FT-IR) SPECTROSCOPY

FT-IR spectra of samples were obtained using a Nicolet 6700 spectrometer (Thermo Scientific, Waltham) to probe the chemical structures of the synthesize polymer films. All scanning was performed with 256 scans per sample with a spectrum resolution of 4 cm^{-1}.

3.3.5. X-RAY PHOTOELECTRON SPECTROSCOPY (XPS)

XPS analysis was performed to quantify elemental compositions (C, N, O) of polymer films. XPS spectra were obtained using a Kratos AXIs Ultra DLD spectrometer with a monochromatic Al-Kα X-ray source ($h\nu$ = 1486.5 eV) with a spot size of 400 μm. All binding energies were adjusted to the adventitious C1s signal at 284.8 eV. The peaks were analyzed using CasaXPS software.

3.3.6. QUANTIFYING FREE CARBOXYLIC ACIDS IN POLYMERS USING INDUCTIVELY COUPLED PLASMA MASS SPECTROSCOPY (ICP-MS)

Density of carboxylic acid groups in selective layers of TFC membranes were quantified using the method first proposed by Elimelech and coworkers [13], based on tagging carboxylic acid groups with Ag^+ proposed by Coronell and coworkers [14]. This method uses Ag^+ ions as molecular probes to detect the free carboxylic acids by ion association. In brief, PA_rA_m polymer films were isolated by immersing the membranes in dichloromethane to etch the PES support layers. Free standing polymer films were then washed with excess volume of methanol and vacuum dried at 150 °C for 24 hours to completely remove any residual solvent. Dried films were weighted to calculate the carboxylic acids density in unit mass of polymers. Polymer films were immersed in the binding solution (40 μM $AgNO_3$ in distilled water at pH 10.5) for 10 minutes, and transferred to new binding solution and incubated for another one hour in orbital shaker. After this binding step, films were transferred to the rinsing solution (1 μM $AgNO_3$ in distilled water at pH 10.5) to rinse off any unbound Ag^+ ions in and around the films. The rinsing solution was replaced four times with new solution every 7 minutes. Lastly, films were transferred to 20 mL of elution solution (2% nitric acid, trace metal grade chemical solution) for two hours. After the elution step, films were removed and the elution buffer was subjected to ICP-MS to measure the concentration of Ag^+ ions in the solution. Since

carboxylic acid reactive groups associate with Ag^+ ions with molar ratio of 1:1, the carboxylic acid density per unit mass of polymers were calculated from the amount of Ag^+ ions eluted from the given polymer weights.

Chapter 3.4. Results and Discussion

3.4.1. Formation of thin films with pillar[5]arenes using interfacial polymerization

Pillar[5]arenes (P[5]s), which are macrocycles with a 4.7 Å central cavity that function as molecular pore [15, 16], were integrated into TFC membranes via co-polymerization with conventional TFC membrane monomers, *m*-phenylenediamine (MPD) and 1,3,5-benzenetricarbonyl trichloride (trimesoyl chloride, TMC) (Figure 49). P[5]s and MPDs were dissolved in water and TMCs were dissolved in hexane with different monomer ratios for the interfacial polymerization. In terms of polymerization chemistry, phenolic reactive groups of P[5]s and primary amine groups of MPDs react with acid chloride of TMCs, and form crosslinked aromatic polyester (polyarylate) [17] and polyamide polymer backbones, respectively. The control polyamide (PA_m) and P[5]-integrated polyarylate-polyamid (PA_rA_m) TFC membranes with different monomer ratios were prepared using conventional interfacial polymerization technique on PES ultrafiltration support membranes as described in 3.3.1. The details of membrane fabrication conditions are summarized in Table 2. As shown from the scanning electron microscopy images (Figure 50 and Figure C.1 – Figure C.5), continuous thin films were successfully formed on top of PES support membranes for both PA_m and PA_rA_m membranes.

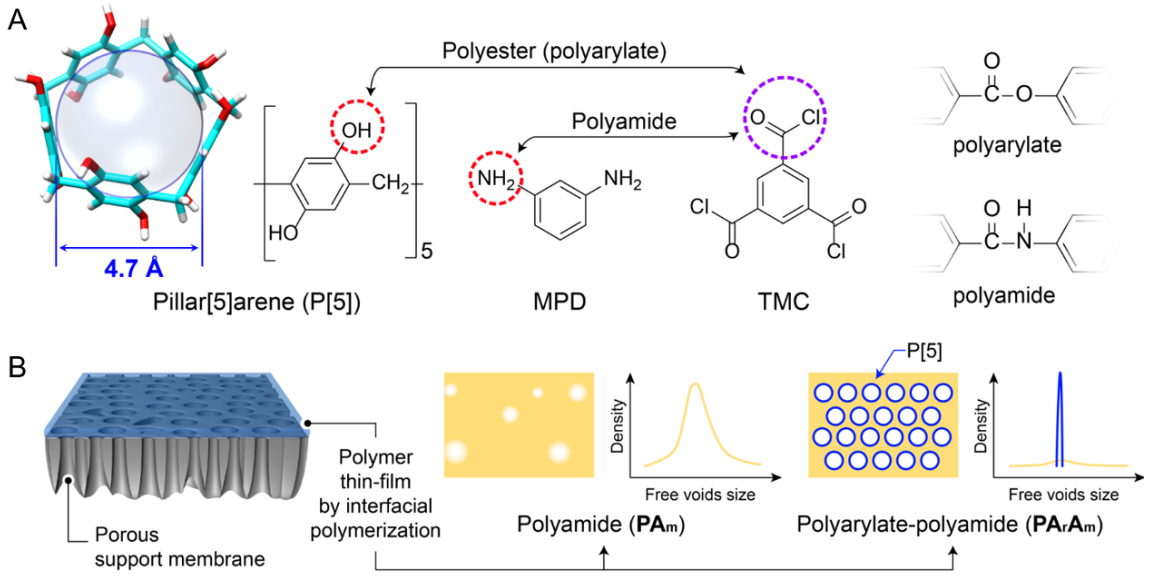

Figure 49. Pillar[5]arene integration into TFC membranes using interfacial polymerization. (A) Chemical structures of control polyamides and P[5]-integrated polyarylate-polyamide TFC membranes. (B) Schematic illustration of increasing nanoscale homogeneity of TFC membranes by incorporating pillar[5]arenes.

	Monomer concentrations (w/v %) in solutions			XPS			Molar ratios of the monomers in polymers			CAs[c] (%)	CA[d] density (10^{-4} mol/g)	P[5]s in polymers (w/w %)
	P[5]	MPD	TMC	C (%)	N (%)	O (%)	P[5]	MPD	TMC			
PA_m		2	0.5	74.55	9.25	16.2		1	1.12	3.85		
PA_rA_m-1	1.5	0.25	0.5	74.92	6.6	18.48	1	4.96	5.31	11.47	6.8	30.3
PA_rA_m-2	1.5	0.5	0.5	75.29	7.58	17.13	1	5.06	3.90	9.83	6.4	34.2
PA_rA_m-3	1.5	0.75	0.5	75.97	7.11	16.92	1	3.38	1.88	7.78	3.4	47.9

Table 2. Summary of the TFC membrane properties.

[c] CAs (%): percentage of free carboxylic acids compared to the number of initially available acid chloride reactive groups in TMC monomers.

[d] CA density (mol/g): mole number of free carboxylic acids per gram of polymer films

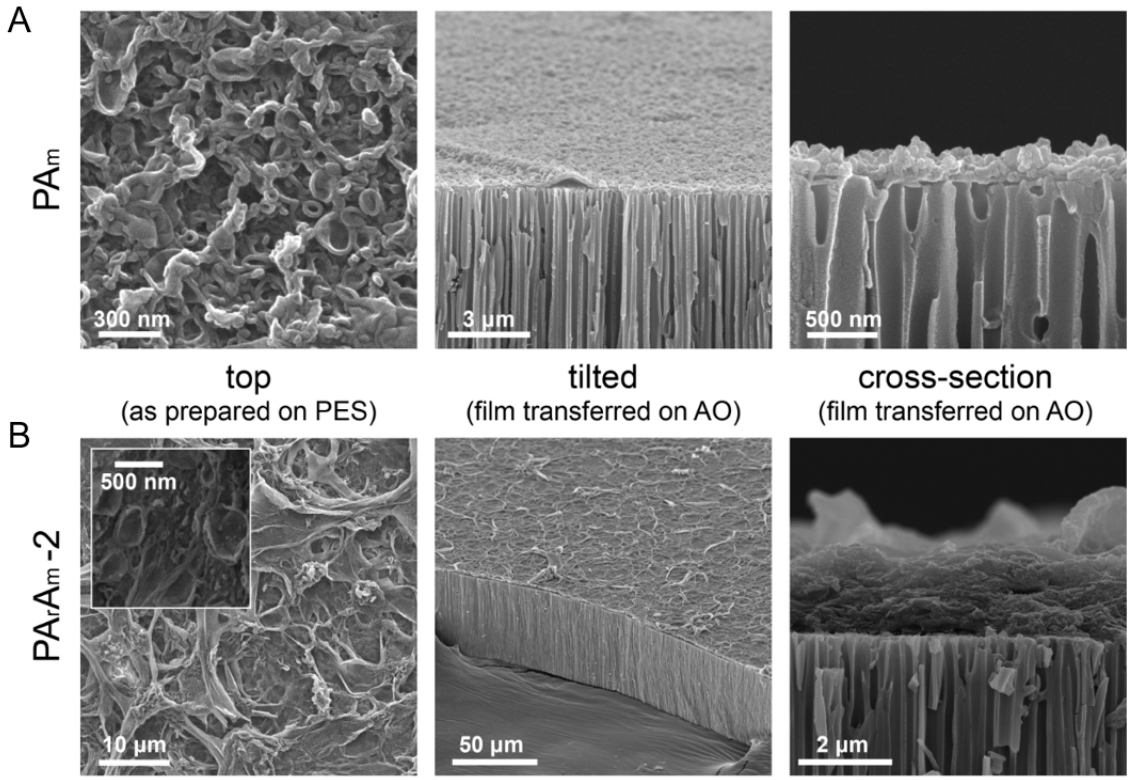

Figure 50. Top, tilted, and cross-sectional SEM images of (A) control PA_m and (B) PA_rA_m-2 membranes showed continuous polymer film formation by interfacial polymerization.

The successful integration of P[5]s into the selective layers was further confirmed by the Fourier-transform infrared (FT-IR) spectroscopy (Figure 51). For both PA_m and PA_rA_m membranes, IR peaks of C=O stretching and N-H bending of the amide bonds were observed at 1630 - 1690 cm^{-1} and 1530 cm^{-1}, respectively. N-H bending of the unreacted amines by MPDs was also observed at 1610 cm^{-1}. In addition, PA_rA_m membranes showed the peak of aromatic ester at 1310 - 1250 cm^{-1} indicating the covalent bond formation by the reactions between P[5]s and TMCs. H-C-H in-plane bending at 1450 cm^{-1} was only observed for PA_rA_m membranes, which is characteristic for P[5]s.

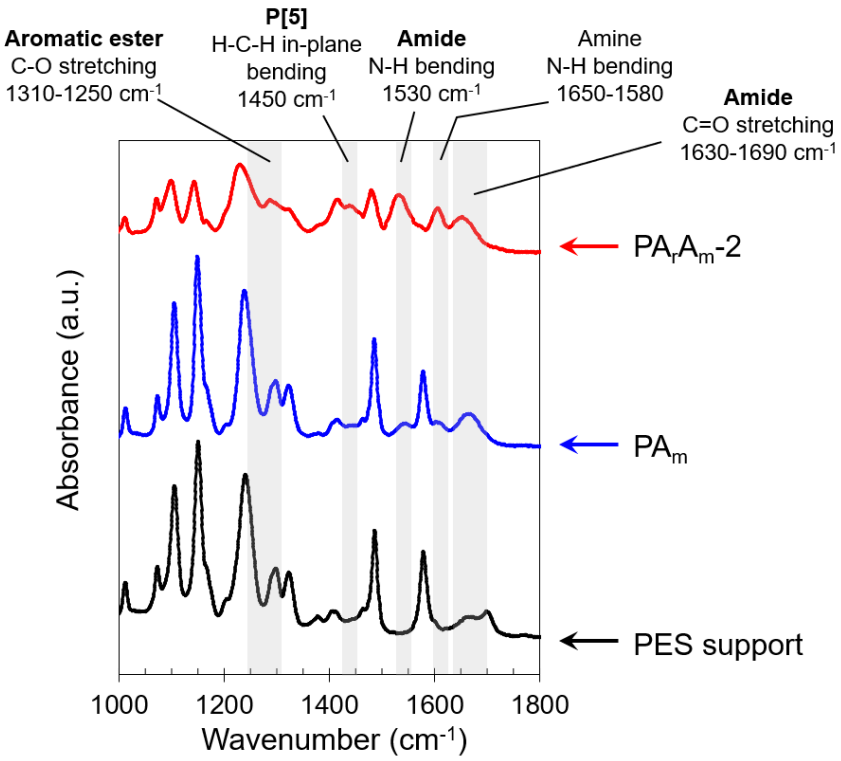

Figure 51. FT-IR spectra of PES support, PA_m, and PA_rA_m-2 membranes.

3.4.2. PURE-GAS PERMEATION TRANSPORT STUDY

Pure-gas permeance of the TFC membranes were tested using the constant-volume and variable-pressure permeation units (Figure 52, Table 3, and Table 4). Representative pure-gas selectivity of the PA_rAm-2 membranes at 35 °C and 10 atm were 32 (H_2/CO_2), 13 (O_2/N_2), 150 (CO_2/CH_4), 4700 (H_2/CH_4), 4.6 (N_2/CH_4), which are higher than the pure-gas selectivity values of the PA_m membranes by up to one order of magnitude. As a comparison, PA_m membrane selectivity values are 7 (H_2/CO_2), 7.4 (O_2/N_2), 45 (CO_2/CH_4), 295 (H_2/CH_4), 1.7 (N_2/CH_4). Also, the other PA_rA_m-1 and the PA_rA_m-3 TFC membranes showed significantly enhanced pure-gas selectivity than the selectivity of PA_m membranes (Figure 52, Table 3, and Table 4), showing the increased molecular sieving effects of the membranes by P[5] integration. The PA_rA_m membranes were also tested under the pressure

range up to 30 atm and gas permeance was stable (Figure 53). Good mechanical stability of the membranes also could be seen from the CO_2 permeance trend with increasing pressure up to 33 bar (~480 psia) that followed the dual mode sorption behavior without showing apparent plasticization, which could be attributed to highly crosslinked chemistry of the interfacial polymerization, which was also observed in conventional polyamide TFC membranes (Figure 54) [9].

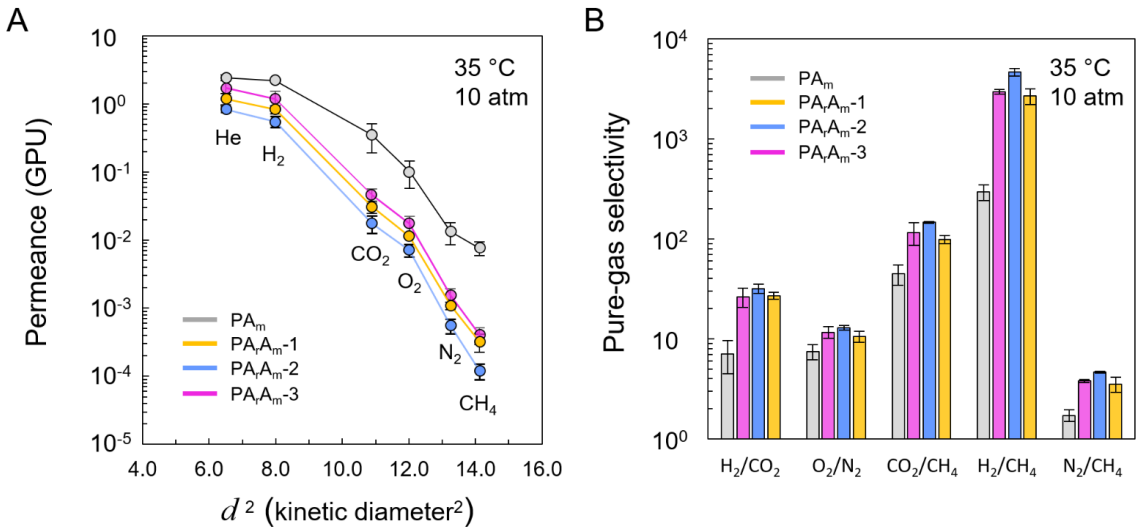

Figure 52. Representative pure-gas permeation results of the PA_m and PA_rA_m membarnes measured at 35 °C and 10 atm. Results are average of three independent membrane measurements. Error bars represent standard deviations. (A) Permeance of different gases. (B) Representative gas pair selectivity.

	He	H_2	CO_2	O_2	N_2	CH_4
PA_m	2.4 ± 0.2	2.2 ± 0.2	0.35 ± 0.16	0.1 ± 0.04	0.013 ± 0.004	0.007 ± 0.0018
PA_rA_m-1	1.2 ± 0.2	0.83 ± 0.1	0.031 ± 0.006	0.011 ± 0.0001	0.0011 ± 0.0001	0.00032 ± 0.00009
PA_rA_m-2	0.82 ± 0.08	0.54 ± 0.1	0.018 ± 0.005	0.0071 ± 0.0015	0.00055 ± 0.0001	0.00012 ± 0.00003
PA_rA_m-3	1.7 ± 0.7	1.2 ± 0.3	0.046 ± 0.01	0.018 ± 0.005	0.0015 ± 0.0004	0.0004 ± 0.0001

Table 3. Gas permeance of the PA_m and PA_rA_m membranes measured at 35 °C and 10 atm. The permeance unit of this table is GPU.

	H_2/CO_2	H_2/CH_4	H_2/N_2	O_2/N_2	CO_2/CH_4	N_2/CH_4
PA_m	7.0 ± 2.5	300 ± 50	180 ± 50	7.4 ± 1.3	45 ± 10	1.7 ± 0.2
PA_rA_m-1	27 ± 2	2700 ± 470	770 ± 5	11 ± 1.3	100 ± 10	3.5 ± 0.6
PA_rA_m-2	32 ± 4	4700 ± 410	1000 ± 70	13 ± 0.6	150 ± 3.7	4.6 ± 0.1
PA_rA_m-3	27 ± 6	3000 ± 160	780 ± 70	12 ± 1.6	120 ± 30	3.8 ± 0.1

Table 4. Representative pure-gas selectivity data of the PA_m and PA_rA_m membarnes measured at 35 °C and 10 atm.

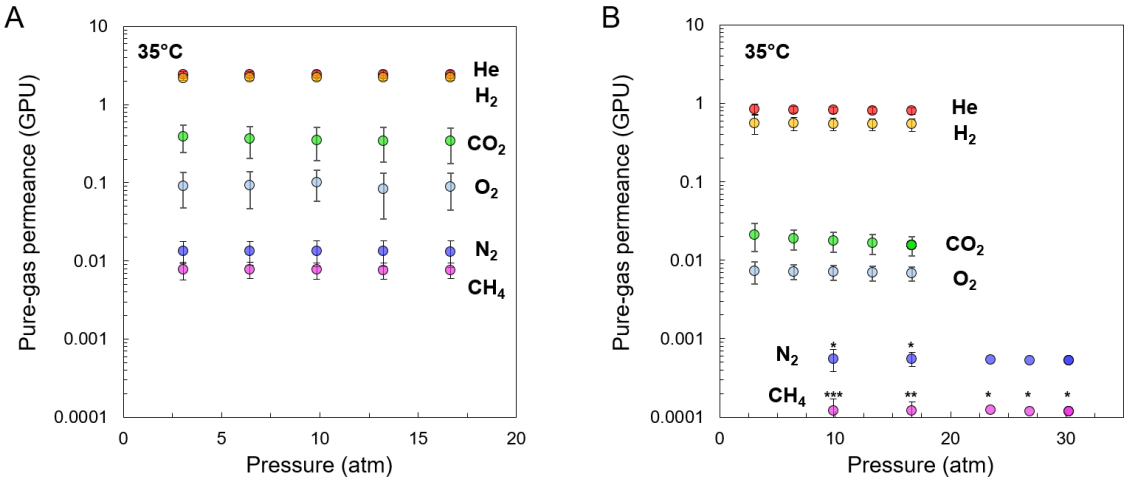

Figure 53. Pure-gas permeance data of (A) the PA_m and (B) PA_rA_m-2 membranes, measured at 35 °C and different pressures. Results are average of three independent membrane measurements. Error bars represent standard deviations. Leak errors of the measurements were less than 1% unless specified as following. *: 1 ~ 5%, **: 5 ~ 10%, ***: 10 ~ 15%.

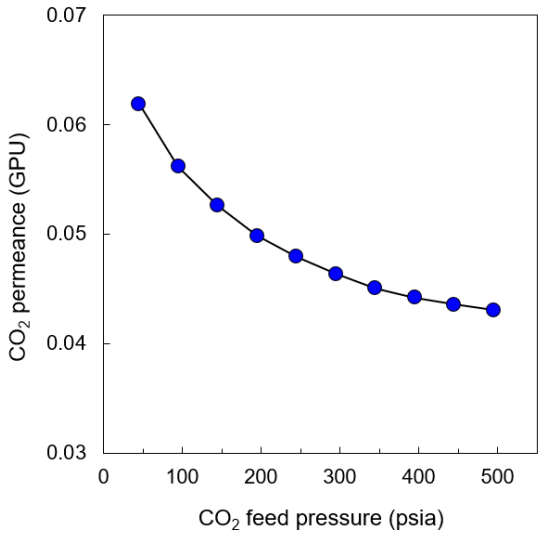

Figure 54. CO_2 permeance change of PA_rA_m-2 TFC membrane with pressures increasing up to 480 psia.

3.4.3. CHARACTERIZATION OF POLYMER FILMS

To find relations between the integrated P[5]s and observed membrane materials and transport properties, the molar ratios of P[5], MPD, and TMC monomers in the polymer films were quantified using X-ray photoelectron spectroscopy (XPS) and Ag^+ tagging of free carboxylic acids in the polymer films as described in 3.3.6 [13, 14, 18], and the results are summarized in Table 2. In brief, after interfacial polymerization, unknown parameters of the polymers in terms of molecular compositions are the molar ratio of each monomers and the number of free carboxylic acids, which are formed by hydrolysis of unreacted acid chloride reactive groups of TMCs. Therefore, PA_m membranes have three unknown parameters (ratio of MPD and TMC, and free carboxylic acids) while PA_rA_m membranes have four (ratio of P[5], MPD and TMC, and free carboxylic acids). From XPS analysis, elemental compositions of carbon (C), nitrogen (N), and oxygen (O) atoms in the polymer films were quantified, and this information was directly used to calculate the unknown three parameters of the PA_m polymers using the three mass balance equations about C, N, and O. For the PA_rA_m polymer membranes, polymer films were isolated by etching the PES support membranes with dichloromethane (DCM, Figure 55) and free carboxylic acids in the isolated polymers were first quantified by tagging free carboxylic acids with Ag^+. The number of associated Ag^+ ions per unit mass of polymers, which corresponds to the number of carboxylic acids, were analyzed using ICP-MS as described in 3.3.6. After this, the ratio of P[5], MPD and TMC were calculated from three mass balance equations about C, N, and O, with known carboxylic acid density in the polymers. As a result, the weight fractions of P[5]s in the PA_rA_m polymers were in the range between 30 ~ 48 % (w/w), which shows substantial fractions of P[5]s integrated in the thin polymer films (Table 2). Also, the PA_rA_m-2 membranes with 34.2 % (w/w) P[5]s in the polymers, which is placed in the middle of the range, showed the strongest molecular sieving

properties than others (Figure 52B). It corresponds with our presumptions that there would be optimized P[5] ratio relative to MPD and TMC monomers. It is noteworthy to point out that, during last few years, several variants of macrocycles have been attempted to prepare PA_r TFC membranes using interfacial polymerization with TMCs, but none of those membranes have been reported as successful in gas separations with to our knowledge [19, 20, 21]. It is hypothesized that minimizing undesired inter-voids between macrocycles by introducing additional monomer MPDs would be the key to maximize molecular sieving effects of the membranes for gas separations (Figure 56). It was further supported by that the PA_r membranes prepared by P[5]s and TMCs without MPDs showed Knudsen selectivity even though continuous films were formed (Figure C.6).

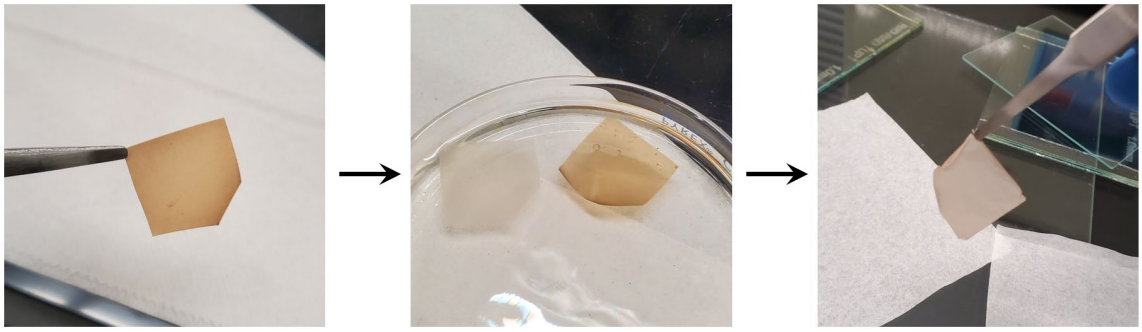

Figure 55. Isolation of free standing PA_rA_m polymer films from the TFC membranes by DCM etching of PES layer.

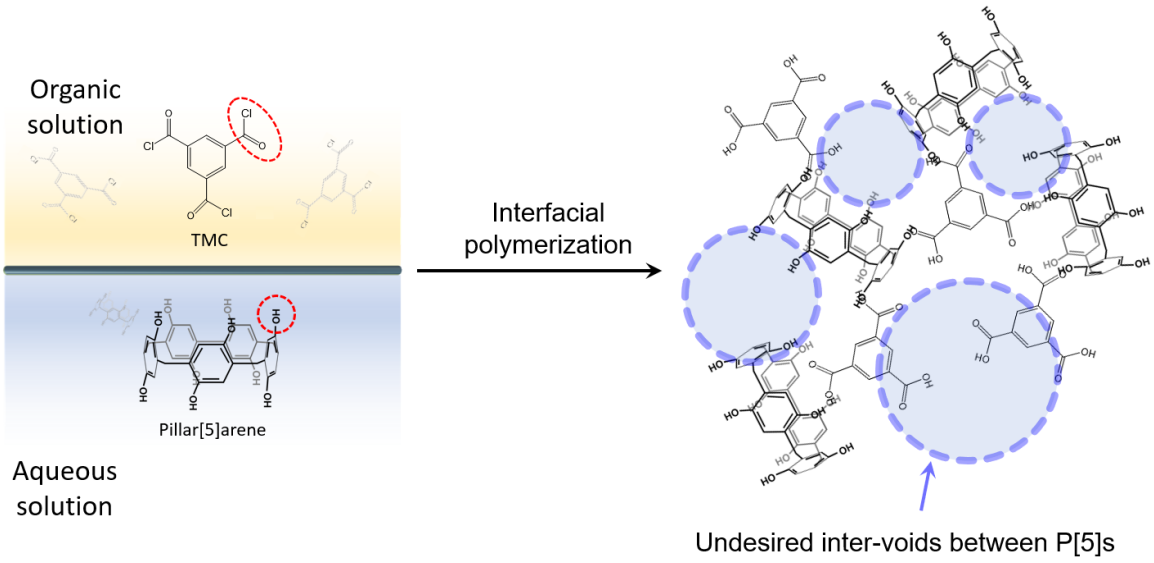

Figure 56. Schematic figures to show the undesired inter voids between P[5]s in PA_r polymers that could be formed by interfacial polymerization by P[5]s and TMCs monomers without MPDs.

The thickness of the polymer films of TFC membranes were further investigated through cross-sectional SEM analyses (Figure 50 and Figure C.2 – Figure C.5). As observed from the images, PA_rA_m membranes have substantially thicker selective layers compared to control PA_m membranes. It is hypothesized that, as the P[5]s have more rigid and bulky structures than other two monomers (MPD and TMC), the polymer chains loose the flexibility and the freedom of rotation during the polymerization and result in relatively thicker layers than control PA_m membranes. Line scanning of the film thicknesses from the cross-sectional SEM images on randomly chosen 50 spots further supported this, showing the clear relations between the weight fractions of P[5]s in the polymers and the film thicknesses (Figure 57). This relatively thick but still less than few (< three) microns film thickness could be a good compromise between membrane permeance and the defect-free membrane fabrications. One challenge of the TFC membranes for gas separations has been susceptibility to pinholes [22, 23, 24]. Many studies on commercially available PA_m TFC

membranes showed the presence of defects of the TFC membranes for gas separations and, to avoid these problems, several approaches have been suggested such as caulking the pinholes with rubbery polydimethylsiloxane (PDMS) polymers [9], or increasing the reaction time and temperature of the interfacial polymerization [25, 26, 27]. In this study, the PA_m membranes were also prepared by increasing the reaction time up to 10 minutes for defect-free thin film formation. While the same reaction time was also used for the PA_rA_m membranes for the comparison, the defect-free PA_rA_m membranes could be readily prepared even with the reaction time reduced up to one minute (Figure 58). On the other hand, the PA_m TFC membranes were not reproducible and resulted in many defects under the reaction time less than 10 minutes.

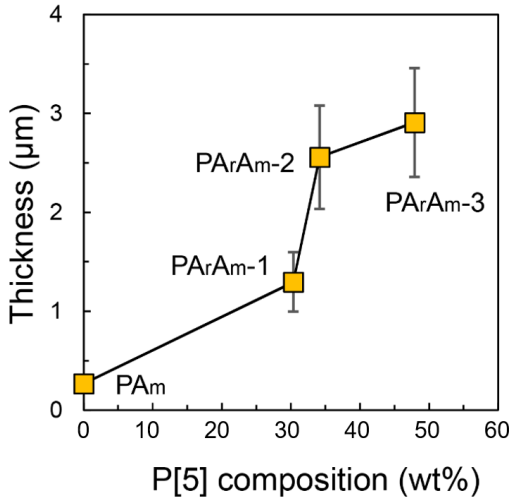

Figure 57. Relations between thicknesses and P[5] compositions in PA_m and PA_rA_m polymer films of the TFC membranes. Polymer film thicknesses were measured by line-scanning the cross-sectional SEM images at 50 different spots of more than 20 independent images. Error bars represent standard deviations.

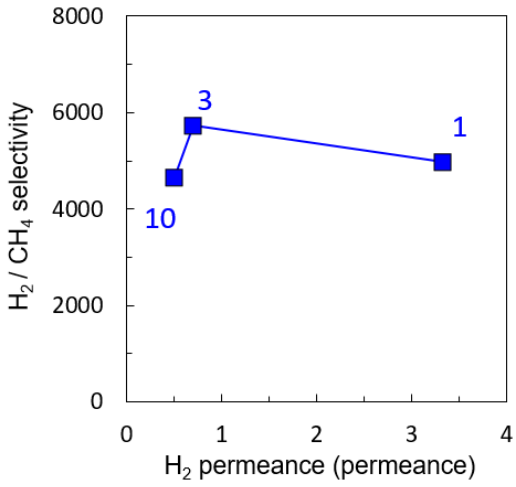

Figure 58. Pure-gas H_2 permeance and H_2 / CH_4 selectivity of PA_rA_m-2 membranes that are prepared with different reaction times. The numbers in the graph represent interfacial polymerization reaction times.

3.4.4. TRANSPORT PROPERTY COMPARISON TO OTHER GAS SEPARATION POLYMERS

Based on the pure-gas permeation data and the thickness information of polymer films, pure-gas permeability and selectivity were calculated and compared to each other as well as to the Robeson plots [28, 29]. First, for the gas pairs with relatively small gases such as He and H_2, pillar[5]arene incorporation resulted in both increased permeability and selectivity compared to the control PA_m TFC membranes. (Figure 59A and Figure 59B). For other gas pairs, it was shown that permeability decreased but selectivity still outperforms most of the other polymers, demonstrating good molecularly selective properties. These separation factors could be attributed to the presence of mechanically and chemically stable ultramicropores (< 7 μm in diameter) that were introduced by pillar[5]arenes [30, 31]. Even though further verification will be desired, it is highly postulated that this enhancement is the results of the improved nanoscale homogeneity of the polymers, considering the substantial weight fractions of pillar[5]arenes and their rigid

molecular structures. Integration of such ultramicropores into the large-scale membranes has been a long-lasting challenge in membrane materials developments [30, 32, 33]. For example, materials with permanent micro porosity such as zeolites, metal-organic frameworks (MOFs), and covalent-organic frameworks (COFs) have been extensively studied but processing them into thin or modular membrane formats is still of great challenge. Pillar[5]arene based TFC membranes provide good comprise between polymers and inorganic (e.g., zeolites or MOFs) materials in terms of membrane processability and the controlled rigid microstructures. Therefore, the presented P[5]-integrated TFC membranes could offer good opportunity to address current challenges for viable membrane developments.

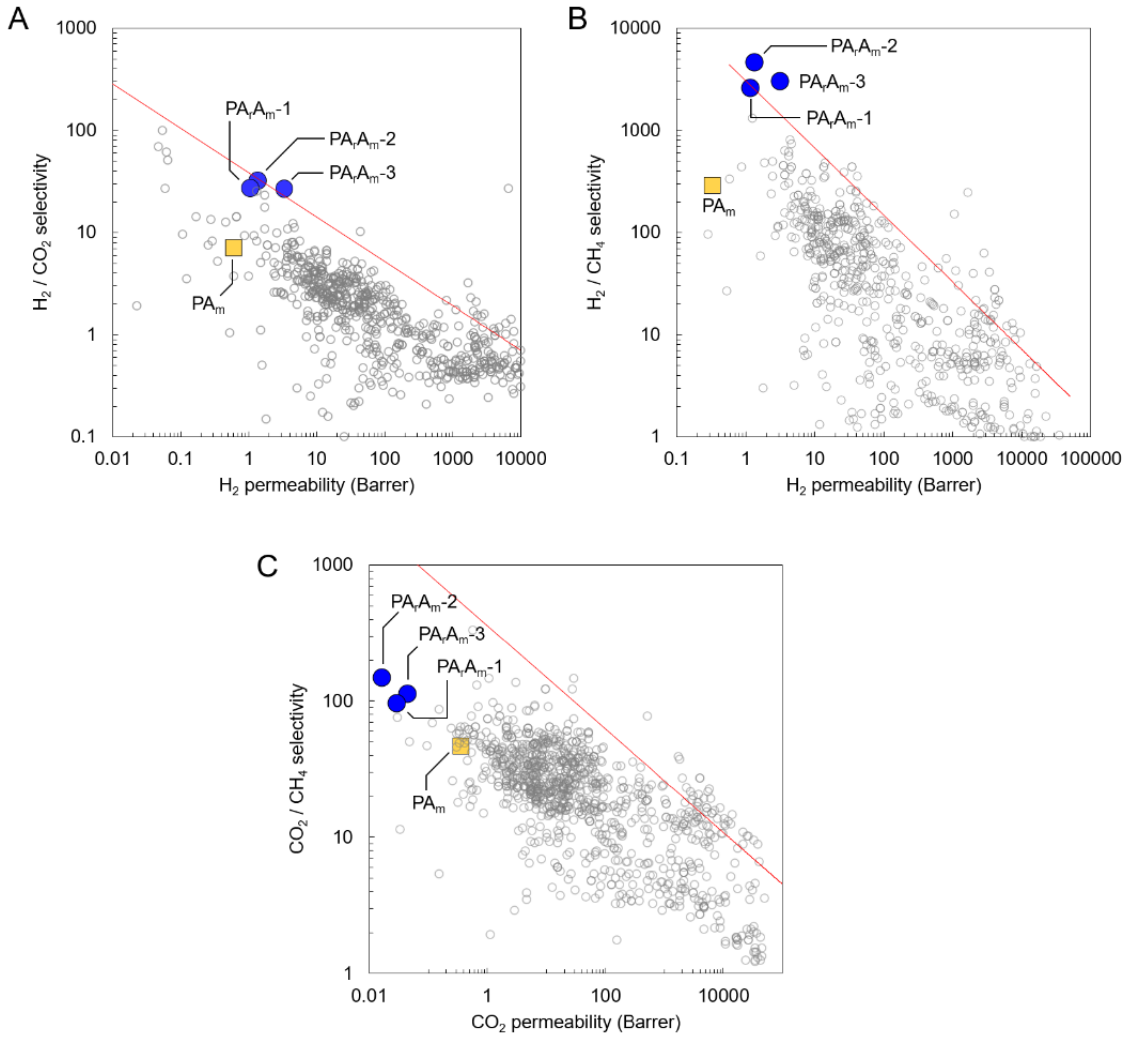

Figure 59. Permeability and selectivity comparison of PA_m and PA_rA_m polymer films to the Robeson plots for (A) H_2/CO_2, (B) H_2/CH_4, and (C) CO_2/CH_4 gas pairs. Red lines are 2008 Robson upper bound limits [28].

Chapter 3.5: Conclusion

Pillar[5]arene macrocycles with ~4.7 Å rigid ultramicropores have been integrated into TFC membranes using interfacial polymerization, to maximize gas separation factors while maintaining the processability of the membranes for large-scale applications. Pure-gas transport data showed that the incorporated pillar[5]arenes substantially increased

molecular sieving effects of the TFC membranes for all gas pairs tested. Also, pillar[5]arenes were highly crosslinked into the polymers with weight fractions up to ~48%. These results indicate that the presented improvements of gas separation properties are attributed to the improved quality of the polymers in terms of nanoscale density distributions with rigid microstructures. However, more scientific verification would be desired to prove this using other analytical tools such as TEM tomography [8, 34] and/or computer simulations. While further optimization steps would be necessary, the P[5]-TFC membranes demonstrated several critical features that should be considered for practical large-scale applications; processing the materials into submicron thicknesses and maintaining mechanical and chemical stabilities. Combined with the precisely controlled molecular structures, the macrocycle incorporated TFC membranes could pave the way for the new membrane developments for advanced molecular separations.

REFERENCES

[1] Sholl, D.S., Lively, R.P., Seven chemical separations to change the world, Nature 532 (2016) 435-437.

[2] Baker, R.W., Future Directions of Membrane Gas Separation Technology, Industrial & Engineering Chemistry Research 41(6) (2002) 1393-1411.

[3] Galizia, M., Chi, W.S., Smith, Z.P., Merkel, T.C., Baker, R.W., Freeman, B.D., 50th Anniversary Perspective: Polymers and Mixed Matrix Membranes for Gas and Vapor Separation: A Review and Prospective Opportunities, Macromolecules 50(20) (2017) 7809-7843.

[4] Baker, R.W., Low, B.T., Gas Separation Membrane Materials: A Perspective, Macromolecules 47(20) (2014) 6999-7013.

[5] Marchetti, P., Jimenez Solomon, M.F., Szekely, G., Livingston, A.G., Molecular Separation with Organic Solvent Nanofiltration: A Critical Review, Chemical Reviews 114(21) (2014) 10735-10806.

[6] Elimelech, M., Phillip, W.A., The Future of Seawater Desalination: Energy, Technology, and the Environment, Science 333(6043) (2011) 712-717.

[7] Geise, G.M., Why polyamide reverse-osmosis membranes work so well, Science 371(6524) (2021) 31-32.

[8] Culp, T.E., Khara, B., Brickey, K.P., Geitner, M., Zimudzi, T.J., Wilbur, J.D., Jons, S.D., Roy, A., Paul, M., Ganapathysubramanian, B., Zydney, A.L., Kumar, M., Gomez, E.D., Nanoscale control of internal inhomogeneity enhances water transport in desalination membranes, Science 371(6524) (2021) 72-75.

[9] Park, J., Yoon, H.W., Paul, D.R., Freeman, B.D., Gas transport properties of PDMS-coated reverse osmosis membranes, Journal of Membrane Science 604 (2020) 118009.

[10] White, L.S., Blinka, T.A., Kloczewski, H.A., Wang, I.f., Properties of a polyimide gas separation membrane in natural gas streams, Journal of Membrane Science 103(1) (1995) 73-82.

[11] Tan, Z., Chen, S., Peng, X., Zhang, L., Gao, C., Polyamide membranes with nanoscale Turing structures for water purification, Science 360(6388) (2018) 518-521.

[12] Xie, W., Geise, G.M., Freeman, B.D., Lee, H.-S., Byun, G., McGrath, J.E., Polyamide interfacial composite membranes prepared from m-phenylene diamine, trimesoyl chloride and a new disulfonated diamine, Journal of Membrane Science 403-404 (2012) 152-161.

[13] Chen, D., Werber, J.R., Zhao, X., Elimelech, M., A facile method to quantify the carboxyl group areal density in the active layer of polyamide thin-film composite membranes, Journal of Membrane Science 534 (2017) 100-108.

[14] Coronell, O., Mariñas, B.J., Zhang, X., Cahill, D.G., Quantification of Functional Groups and Modeling of Their Ionization Behavior in the Active Layer of FT30 Reverse Osmosis Membrane, Environmental Science & Technology 42(14) (2008) 5260-5266.

[15] Feng, W.-X., Sun, Z., Barboiu, M., Pillar[n]arenes for Construction of Artificial Transmembrane Channels, Israel Journal of Chemistry 58(11) (2018) 1209-1218.

[16] Xue, M., Yang, Y., Chi, X., Zhang, Z., Huang, F., Pillararenes, A New Class of Macrocycles for Supramolecular Chemistry, Accounts of Chemical Research 45(8) (2012) 1294-1308.

[17] Jimenez-Solomon, M.F., Song, Q., Jelfs, K.E., Munoz-Ibanez, M., Livingston, A.G., Polymer nanofilms with enhanced microporosity by interfacial polymerization, Nature Materials 15(7) (2016) 760-767.

[18] Coronell, O., Mariñas, B.J., Cahill, D.G., Accessibility and Ion Exchange Stoichiometry of Ionized Carboxylic Groups in the Active Layer of FT30 Reverse Osmosis Membrane, Environmental Science & Technology 43(13) (2009) 5042-5048.

[19] Zhao, Q., Liu, Y., Macrocycle crosslinked mesoporous polymers for ultrafast separation of organic dyes, Chemical Communications 54(53) (2018) 7362-7365.

[20] Ke, J., Zhang, Y., Zhang, X., Liu, Y., Ji, Y., Chen, J., Novel chiral composite membrane prepared via the interfacial polymerization of diethylamino-beta-cyclodextrin for the enantioseparation of chiral drugs, Journal of Membrane Science 597 (2020) 117635.

[21] Villalobos, L.F., Huang, T., Peinemann, K.-V., Cyclodextrin Films with Fast Solvent Transport and Shape-Selective Permeability, Advanced Materials 29(26) (2017) 1606641.

[22] Sridhar, S., Smitha, B., Mayor, S., Prathab, B., Aminabhavi, T.M., Gas permeation properties of polyamide membrane prepared by interfacial polymerization, Journal of Materials Science 42(22) (2007) 9392-9401.

[23] Louie, J.S., Pinnau, I., Reinhard, M., Gas and liquid permeation properties of modified interfacial composite reverse osmosis membranes, Journal of Membrane Science 325(2) (2008) 793-800.

[24] Mohammadi, A.T., Matsuura, T., Sourirajan, S., Gas separation by silicone-coated dry asymmetric aromatic polyamide membranes, Gas Separation & Purification 9(3) (1995) 181-187.

[25] Ali, Z., Ghanem, B.S., Wang, Y., Pacheco, F., Ogieglo, W., Vovusha, H., Genduso, G., Schwingenschlögl, U., Han, Y., Pinnau, I., Finely Tuned Submicroporous Thin-Film Molecular Sieve Membranes for Highly Efficient Fluid Separations, Advanced Materials 32(22) (2020) 2001132.

[26] Ali, Z., Wang, Y., Ogieglo, W., Pacheco, F., Vovusha, H., Han, Y., Pinnau, I., Gas separation and water desalination performance of defect-free interfacially polymerized para-linked polyamide thin-film composite membranes, Journal of Membrane Science 618 (2021) 118572.

[27] Ali, Z., Pacheco, F., Litwiller, E., Wang, Y., Han, Y., Pinnau, I., Ultra-selective defect-free interfacially polymerized molecular sieve thin-film composite membranes for H2 purification, Journal of Materials Chemistry A 6(1) (2018) 30-35.

[28] Robeson, L.M., The upper bound revisited, Journal of Membrane Science 320(1) (2008) 390-400.

[29] Thornton, A.W., Freeman, B.D., Polymer Gas Separation Membrane Database. http://membrane-australasia.org/.

[30] Koros, W.J., Zhang, C., Materials for next-generation molecularly selective synthetic membranes, Nature Materials 16(3) (2017) 289-297.

[31] Singh, A., Koros, W.J., Significance of Entropic Selectivity for Advanced Gas Separation Membranes, Industrial & Engineering Chemistry Research 35(4) (1996) 1231-1234.

[32] Qian, Q., Asinger, P.A., Lee, M.J., Han, G., Mizrahi Rodriguez, K., Lin, S., Benedetti, F.M., Wu, A.X., Chi, W.S., Smith, Z.P., MOF-Based Membranes for Gas Separations, Chemical Reviews 120(16) (2020) 8161-8266.

[33] Kosinov, N., Gascon, J., Kapteijn, F., Hensen, E.J.M., Recent developments in zeolite membranes for gas separation, Journal of Membrane Science 499 (2016) 65-79.

[34] Culp, T.E., Shen, Y.-x., Geitner, M., Paul, M., Roy, A., Behr, M.J., Rosenberg, S., Gu, J., Kumar, M., Gomez, E.D., Electron tomography reveals details of the internal microstructure of desalination membranes, Proceedings of the National Academy of Sciences 115(35) (2018) 8694-8699.

SUMMARY AND RECOMMENDATIONS

Chapter 4.1: Summary

Inspired by biological membranes that demonstrate exceptional performances with regard to molecular separations, bioinspired channel-based synthetic membranes have been created and tested. The proposed membranes have demonstrated their potentials for advanced molecular separations from various perspectives, including nanoscale transport, channel reconstitution into scalable membranes, and transformation to the new membrane designs that are viable for the large-scale applications. These achievements were possible due primarily to the precise control of microstructures of the membrane elements and, therefore, improve the internal uniformity of the membranes at molecular scale. Based on the knowledges acquired in this dissertation research, the following studies are suggested for future work to help these membranes contribute better to the membrane community as well as the developments of viable membranes for energy and environmental sustainability.

Chapter 4.2: Recommendations for future work

4.2.1. PAH[4] ARTIFICIAL WATER CHANNELS

A unique mechanism of water transport in PAH[4] clusters have been investigated. This study was carried out based on the standard biological membrane matrix, phospholipid bilayers. One open question is whether this transport mechanism will be preserved in the other biomimetic membrane matrices. Special interests would be studying in synthetic membranes such as block copolymers as it is important for the next step of scaling up the membranes for separation applications. Since one of the key mechanisms of water transport through PAH[4] channels is cluster formation, this study could be much more critical

compared to the other water channel cases. For example, membrane matrix fluidity could affect the dynamics of lateral diffusion of channels in membranes and, therefore, the formation of channel clusters. Also, PAP[5] artificial water channels, which are structural analogous to PAH[4]s, showed channel cluster formation in PB-PEO block copolymer membranes but not in lipid bilayer membranes, implying better channel-to-channel interactions rather than channel-to-matrix in block copolymer membranes [1, 2]. Therefore, further transport study in synthetic polymer-based membrane matrices would be a milestone to assess the future potential of PAH[4] channels for the developments of channel-based membranes.

4.2.2. ARTIFICIAL WATER CHANNEL-BASED MEMBRANES FOR MOLECULAR SEPARATIONS

PAP[5] artificial water channels were used to fabricate channel-based membranes with high channel packing density. A series of transport study showed the size-sieving effects of the membranes that corresponds to the PAP[5] channels' molecular configuration. One interesting observation was the transmission of the linear molecules PEO oligomers. It is hypothesized that this is attributed to (1) the characteristic molecular pore configurations of channel-based membranes that span through the membranes and (2) PEO polymer brushes facing toward the entrances of the channels (pores). Therefore, additional study with other linear-shaped oligomers rather than PEOs would provide further insights on the shaped-dependent and/or intermolecular interaction (between permeants and matrix polymers) dependent transmission of the molecules through the channel-based membranes.

4.2.3. MACROCYCLE BASED TFC MEMBRANES FOR GAS SEPARATIONS

Pillar[5]arene based TFC membranes have been investigated and proved that significant amount of pillar[5]arenes were successfully integrated with weight fractions up to ~48% and increased the molecular sieving effects of the membranes. It was hypothesized that the integrated pillar[5]arenes improved the nanoscale homogeneity of the polymer membranes compared to the conventional polyamide TFC membranes. Further analytical analyses are recommended to verify this. Recent study of using transmission electron microscopy, for example, demonstrated that the electron tomography is a great tool to investigate the polymer nanofilms' internal physical properties with one-nanometer resolution and their effects on molecular transport in the polymers [3, 4]. Applying such an analytical tool for the pillar[5]arene based polymer films would provide better understanding on the microstructures-to-transport relationships of macrocycle-based TFC membranes.

Studying the pillar[5]arene based polymers using computer simulation is also recommended. Given molecular compositions of the polymers such as the ratios of pillar[5]arene, MPD and TMC, the Polymatic algorithm has been widely used to generate amorphous structures of the polymers to study the materials and transport properties at molecular level [5]. For example, using the generated polymer models, gas sorption properties can be studied with canonical Monte Carlo (GCMC) simulations [6]. Also, molecular dynamic simulations can be used to track the trajectory of molecular diffusion in the polymers to investigate whether the pillar[5]arene macrocycles actually function as molecular pores.

In addition, further transport study such as mixed-gas permeation experiments is recommended. Due to the complexity of the actual compositions of industrial pipelines, molecular transport properties could behave differently compared to the pure-gas

permeation environments. One of the representative examples are gas permeation with condensable contaminants such as CO_2 and water vapor. Such condensable species can result in different ways of increasing and/or decreasing gas permeance, due to the interplay of plasticization, antiplasticization, and competitive sorption [7, 8, 9, 10]. Therefore, mixed-gas transport study is imperative to resolve this open question.

Lastly, as the macrocycle-based TFC membranes were first developed seeking the applications toward the large-scale processes, further optimization steps would be necessary. Currently, while the membranes showed good selectivity for all gas pairs tested, the permeance is not satisfactory compared to many industrial requirements [11, 12]. Therefore, increasing the global permeance of the membranes will be required. Possible efforts to achieve this goal could include the selection of better support membranes with high porosity or trying other macrocycle variants to increase the free void fractions in the polymers. Also, thin-film formation on hollow-fiber (HF) support membranes could help resolve this permeance issue, as HF membrane modules can provide orders of higher surface area than others [12]. Due to the feasible chemistry of interfacial polymerization, pillar[5]arene-integrated thin film could be formed on the shell side of porous PES hollow fiber membranes (Figure 60). Even though the membranes in Figure 60 showed defects from gas permeation experiments, further optimization steps could achieve the intact HF-TFC membranes with macrocycles for practical gas separation applications.

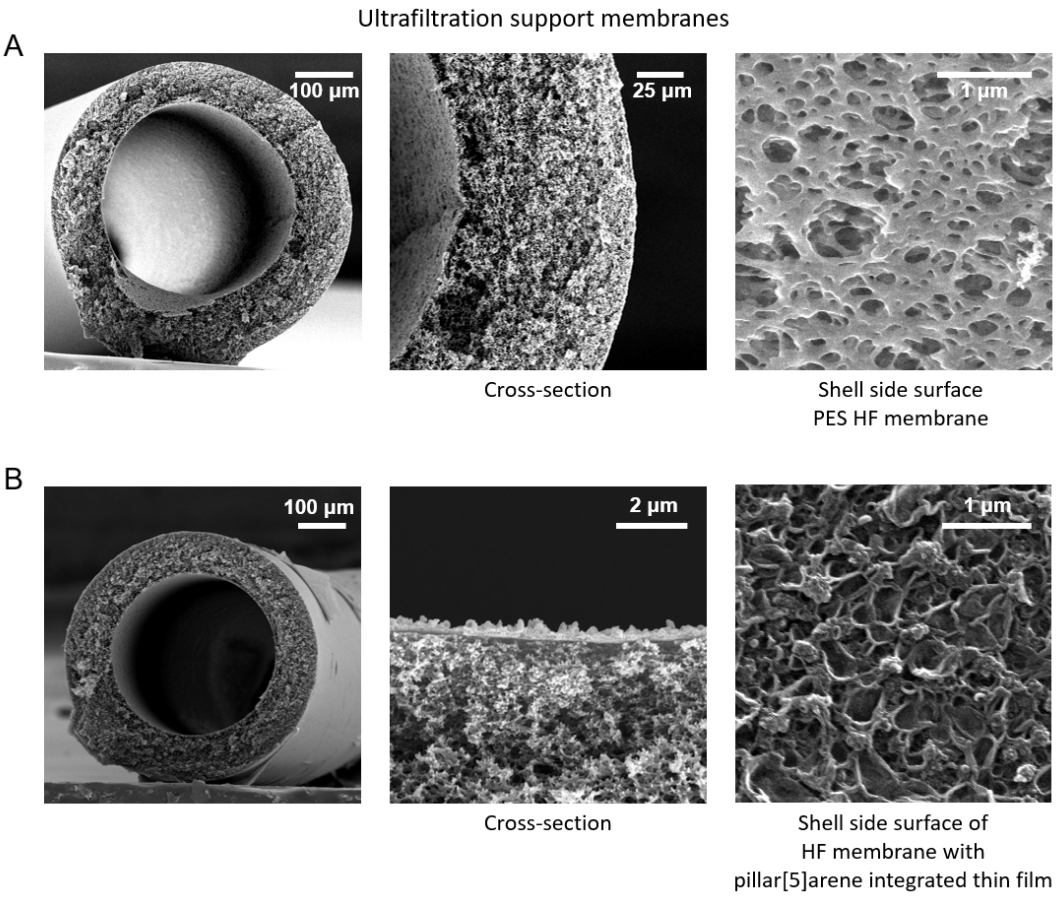

Figure 60. SEM images of hollow fiber (HF) membranes (A) before and (B) after interfacial polymerization on the shell-side surface of HF membranes with pillar[5]arenes. The films were successfully formed with pillar[5]arene macrocycles.

REFERENCES

[1] Shen, Y.-x., Si, W., Erbakan, M., Decker, K., De Zorzi, R., Saboe, P.O., Kang, Y.J., Majd, S., Butler, P.J., Walz, T., Aksimentiev, A., Hou, J.-l., Kumar, M., Highly permeable artificial water channels that can self-assemble into two-dimensional arrays, Proceedings of the National Academy of Sciences, USA 112(32) (2015) 9810-9815.

[2] Shen, Y.-x., Song, W., Barden, D.R., Ren, T., Lang, C., Feroz, H., Henderson, C.B., Saboe, P.O., Tsai, D., Yan, H., Butler, P.J., Bazan, G.C., Phillip, W.A., Hickey, R.J., Cremer, P.S., Vashisth, H., Kumar, M., Achieving high permeability and enhanced selectivity for Angstrom-scale separations using artificial water channel membranes, Nature Communications 9(1) (2018) 2294.

[3] Culp, T.E., Khara, B., Brickey, K.P., Geitner, M., Zimudzi, T.J., Wilbur, J.D., Jons, S.D., Roy, A., Paul, M., Ganapathysubramanian, B., Zydney, A.L., Kumar, M., Gomez, E.D., Nanoscale control of internal inhomogeneity enhances water transport in desalination membranes, Science 371(6524) (2021) 72-75.

[4] Culp, T.E., Shen, Y.-x., Geitner, M., Paul, M., Roy, A., Behr, M.J., Rosenberg, S., Gu, J., Kumar, M., Gomez, E.D., Electron tomography reveals details of the internal microstructure of desalination membranes, Proceedings of the National Academy of Sciences 115(35) (2018) 8694-8699.

[5] Abbott, L.J., Hart, K.E., Colina, C.M., Polymatic: a generalized simulated polymerization algorithm for amorphous polymers, Theoretical Chemistry Accounts 132(3) (2013) 1334.

[6] Dubbeldam, D., Calero, S., Ellis, D.E., Snurr, R.Q., RASPA: molecular simulation software for adsorption and diffusion in flexible nanoporous materials, Molecular Simulation 42(2) (2016) 81-101.

[7] Jordan, S.M., Koros, W.J., Permeability of pure and mixed gases in silicone rubber at elevated pressures, Journal of Polymer Science Part B: Polymer Physics 28(6) (1990) 795-809.

[8] Scholes, C.A., Jin, J., Stevens, G.W., Kentish, S.E., Competitive permeation of gas and water vapour in high free volume polymeric membranes, Journal of Polymer Science Part B: Polymer Physics 53(10) (2015) 719-728.

[9] Scholes, C.A., Jin, J., Stevens, G.W., Kentish, S.E., Hydrocarbon solubility, permeability, and competitive sorption effects in polymer of intrinsic microporosity (PIM-1) membranes, Journal of Polymer Science Part B: Polymer Physics 54(3) (2016) 397-404.

[10] Galizia, M., Chi, W.S., Smith, Z.P., Merkel, T.C., Baker, R.W., Freeman, B.D., 50th Anniversary Perspective: Polymers and Mixed Matrix Membranes for Gas and Vapor Separation: A Review and Prospective Opportunities, Macromolecules 50(20) (2017) 7809-7843.

[11] Baker, R.W., Low, B.T., Gas Separation Membrane Materials: A Perspective, Macromolecules 47(20) (2014) 6999-7013.

[12] Baker, R.W., Future Directions of Membrane Gas Separation Technology, Industrial & Engineering Chemistry Research 41(6) (2002) 1393-1411.

APPENDICES

Appendix A: Supporting Information of SECTION 1[5]

This appendix provides the supporting information for the PAH[4] artificial water channels discussed in SECTION 1.

[5]This appendix has been adapted from:
Song, W. Joshi, H. Chowdhury, R. Najem, J.S. Shen, Y.-x. Lang, C. Henderson, C.B. Tu, Y.-M. Farell, M. Pitz, M.E. Maranas, C.D. Cremer, P.S. Hickey, R.J. Sarles, S.A. Hou, J.-l. Aksimentiev, A. and Kumar, M. Artificial water channels enable fast and selective water permeation through water-wire networks *Nature Nanotechnology* 15, 73-79 (2020).

Woochul Song (W.S.) conceived and designed the research. W.S. performed the experiments of water and ion transport through the PAH[4] channels. W.S. analyzed the data. W.S. wrote the paper.

IN-SILICO EXPERIMENTS: GENERATION OF REPRESENTATIVE PAH[4] CLUSTER CONFIGURATIONS

A PAH[4] monomeric channel was built by *in silico* sculpting eight triPhe chains to the crystal structure of hybrid[4]arene, crystallized by Boinski *et al*. [1]. The PAH[4] channel was CHARMM minimized after building appropriate force-field parameter and topology files. Additional solvation parameters were also added to facilitate the incorporation of an implicit solvation term (using generalized Born solvation) along with van der Waals, and electrostatic energies for the channel. To discern thermodynamically stable dimeric geometries, we performed a simulated-annealing based lateral docking of one monomer against another similar or a flipped monomer and explored six possible configurations (Figure A.1) [2]. Based on the free energies of dimerization, which were computed using the 'interaction-energy' plugin developed in a previous work that reflect the sum of free energies associated with van der Waals, electrostatics, and solvation terms computed at the binding interface [2], only three configurations were identified to have negative free energies and hence stable. We call these three geometries as (a) lateral – where the ~3 Å side of two dimers are next to each other, (b) inverted – where the ~3 Å side of one normal and one flipped monomer are next to each other, and (c) orthogonal – where the ~5 Å side of two channels are juxtaposed (Figure A.1 and Figure A.2). A phosphatidyl choline (POPC)-based membrane patch was used to immobilize 25 such dimers of each type in three independent molecular dynamics (MD) simulation setups. Each of these 400 ns simulations (with Na^+ and Cl^- ions) provided vital insights about water permeation rates and ion rejection (Figure A.3). Results from MD revealed much lower water permeation rates than observed in experiments at high channel density region (Figure 16B). We hypothesized that possible oligomerization of these dimers facilitates high water transport based on their tendency to aggregate as seen from the last 30 ns of the MD

simulations as well as from the experiments (FRAP, AFM, and enhancing permeability at high channel density) (Figure 11, Figure 12, and Figure 16B). Out of the 25 dimers from each of the three setups, we isolated the one which exhibited the highest water transport rates during the course of MD trajectory. Thereafter, we used these three structures to obtain three separate CHARMM-minimized oligomeric cluster (or bouquet) configurations (Figure A.1 and Figure A.2). The bouquet-generation protocol involved iterative docking of PAH[4] dimers onto a growing cluster followed by subsequent short energy minimization run (1000 CHARMM iterations) of the new cluster. This yielded three thermodynamically stable clusters, one for each dimer geometry. Each of the three stable configurations comprised 11 lateral, inverted, and orthogonal dimers respectively. Structural inspection of the cluster structures revealed that the inverted and orthogonal geometries had room for conformational flexibility at the four corners of the clusters, which could lead to defects (pinholes) at the cluster-membrane interface (Figure A.1). If these defects are comparable or bigger than the size of a water molecule, they would render the assessment of water permeation rates inaccurate. To mitigate this, we added one monomer of the respective type at each corner that were able to stabilize them. We further performed detailed energy-minimization (of 100,000 CHARMM iterations) with first 5000 steps of gradient descent followed by 95,000 adoptive-bases Newton Raphson minimization steps on these clusters that yielded stable elliptical geometries, which are easy to embed in membranes without leaving any defects. Thus, each of the three resulting cluster configurations were constituted of 11 dimers of the respective type, and four extra monomers for the inverted and orthogonal cases. The oligomerized clusters now presented the water permeating paths cooperatively interconnected between channels. Nonetheless, to ensure an identical MD analysis of water permeation through these clusters, we replaced the four monomers in the two aforementioned geometries with the amphiphilic membrane

patch to eliminate pinholes. Thus, all three resultant clusters had exactly 11 dimers. A 400 ns all-atom MD simulation was performed using the cluster-membrane assembly and the water permeation rates and ion rejection performances were determined.

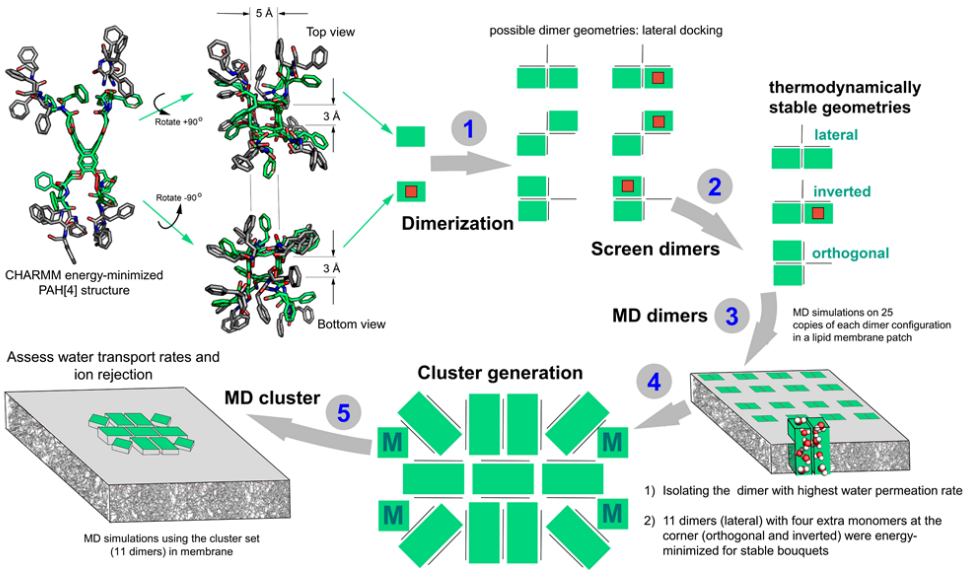

Figure A.1. Overview of the *in silico* procedure for generating PAH[4] cluster configurations to model oligomeric PAH[4] cluster geometry in lipid bilayer membranes.

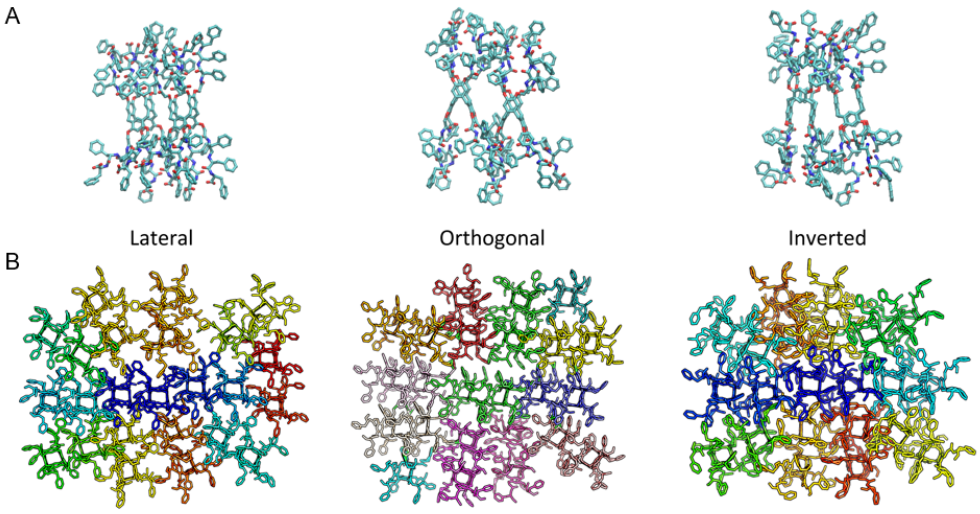

Figure A.2. Three representative lateral, orthogonal, and inverted molecular configurations of (A) dimeric (side-view) and (B) cluster (top-view) PAH[4]s generated *in silico.*

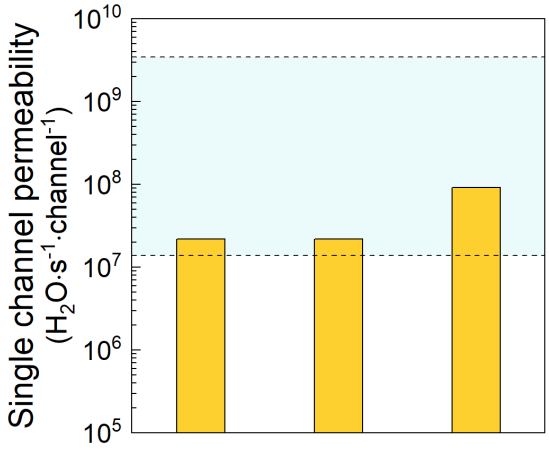

Figure A.3. Average water permeability per PAH[4] channel in MD simulation of a lipid bilayer membrane containing an array of PAH[4] monomers and most conductive dimers and 22-mer clusters. Data were averaged over MD trajectories spanning ~400 ns. The shaded area represents the PAH[4] permeability range measured by experiments.

SUPPLEMENTARY METHODS OF MD SIMULATIONS

To elucidate the microscopic mechanism of transmembrane water permeation through the PAH[4] channels, we have performed atomistic molecular dynamics (MD) simulations. Using a design method similar to that previously applied to PAP[5] channels, we built an atomistic model of the PAH[4] channel. To characterize their nanoscale structure and dynamics, we created the all-atom models of PAH[4] channels in various conformations (monomer, dimer and 11-dimer cluster), embedded them into a patch of pre-equilibrated 1-palmitoyl-2-oleoyl-sn-glycero-3-phosphatidylcholine (POPC) lipid bilayer membrane and solvated in 0.6 M NaCl solution.

First, we simulated a system of 25 PAH[4] monomers arranged as a regular array in the lipid bilayer membrane (Figure A.4A and Figure A.4B). We constrained the non-hydrogen atoms of the PAH[4] to their initial potions for the first 5 ns of the MD simulation and subsequently carried out approximately 310 ns long equilibrium MD simulation without any constraints. The visualization of the simulation snapshots (Figure A.4C) and trajectory of the system suggests that the PAH[4] channels diffuse within the membrane and aggregate into larger clusters. The average root mean square deviation (RMSD) of the individual PAH[4] channel settles around 6 ± 1 Å. The available surface area per PAH[4] channel was 2.38 ± .08 nm^2 towards the end of the MD simulation (Figure A.4D). As the simulation progressed, the water molecules permeated across the membrane through the PAH[4] channels. Figure A.5 shows the pathways of water slipping across the membrane through a PAH[4] channel. We find that the average number of water molecules located within the central 1 nm-width region of the membrane is 51 ± 8, or approximately 2 water molecules per channel (Figure A.4E). The average number of permeated water molecules per channel increases linearly with the simulation time (Figure A.4F) and reaches 8 molecules per channel at the end of the 320 ns run.

To determine the effect of aggregation on the water permeability of the channels, we combined two units of PAH[4] channels to create a PAH[4] dimer (Figure A.1 and Figure A.2) in three different conformations (lateral, orthogonal, and inverted) as described above. Additionally, we also built one more system where the channels of the inverted conformation were filled with water at the beginning of the simulation. Following the similar simulation protocol used for the monomer array system, we simulated an array of 25 dimers of each conformation for 300 - 400 ns. The simulation snapshots of the system (Figure A.6, A - C) show that the PAH[4] dimers tend to assemble in to bigger clusters. Average RMSD of the individual dimer with respect to its initial structure converges to 6 ±1 Å. Average area per dimer reaches approximately 4.3 ± 0.1 nm^2 for all the conformations (Figure A.6D). The number of water molecules in the center region of the membrane increases to 6 - 8 water molecules per dimer depending on the conformation. In the system that was filled with water at the beginning of the simulation, the number of water molecules decreases and reaches 6 - 8 at the end of the simulation (Figure A.6E) The total number of water molecules permeated across the membrane ranges between 12 and 15 per dimer at the end of the simulations. Despite having the least number of water molecules in the channels, as compared to other configuration, the simulations shows that the PAH[4] orthogonal dimer is the most conductive. Transmembrane water permeation through the dimer happens via a continuous water wire guided by the triPhe side chains of PAH[4] (Figure A.5), which is not seen in the monomer structure.

Monomer and dimer array simulations suggest that the aggregation of PAH[4] can produce water wires that span across the membrane region. The transmembrane water permeation also depends on the conformation of the PAH[4]. The histogram of the channel-wise permeated water molecules shows a wide range of the distribution in both monomer and dimers (Figure A.7). Encouraged by these results, we created three all-atom clusters

each containing eleven pre-aggregated dimeric unit of PAH[4], as described in the previous section. These lateral, orthogonal, and inverted cluster structures were embedded in the POPC lipid bilayer membrane. All atom MD simulation of these structures reveal increased water permeability per PAH[4] molecule. Figure A.8, A - C shows the simulation snapshots and trajectory, respectively, of the orthogonal cluster. Average surface area available per PAH[4] molecule from the last 200 ns equilibrium MD simulations is 2.06 ± 0.8 nm^2, 1.78 ± 0.7 nm^2, 2.24 ± 0.8 nm^2 for lateral, orthogonal and inverted clusters, respectively. The average number of water molecules in the central membrane region remain approximately 130 ± 10, 113 ± 10 and 128 ± 13 for lateral, orthogonal and inverted cluster structures, respectively. The number of water molecules that permeated across the membrane reached approximately 39 molecules per PAH[4] channel at the end of the 400 ns MD run of the lateral cluster structure, which we found to be the most conductive conformation. We observed water permeating across the membrane via several dynamic water-wire networks.

Plotting the total number of permeated water molecules as a function of the simulation time, we computed the average single PAH[4] channel water permeability to increase from 0.022 to 0.092 molecules per ns from monomer/dimer to cluster structures, (Figure A.3). Analysis of the MD simulation trajectories suggest that the slip and slide mechanism of water permeation observed in PAH[4] monomer and dimer array systems leads to continuous water wire networks in the PAH[4] cluster structures. These water channels are fundamentally different from the previously characterized transmembrane water channels. We did not observe any ions translocation across the membrane in our equilibrium MD simulation of PAH[4] channels in the monomer, dimer and cluster conformations. To probe the ion rejection efficiency of PAH[4] channel, we applied ± 1 V transmembrane bias in most conductive bouquet structure. Staring with snapshot of the system at the end of 400 ns free equilibration, we carried out additional 100 ns MD

simulation with ± 1 V applied bias. Neither Na^+ nor Cl^- ion translocated through any of these channels in the applied bias simulation. Overall, all-atom MD simulation suggests that the aggregation of PAH[4] give rise to enhanced transmembrane water permeability via water-wire networks and that these channels do not facilitate ion transport.

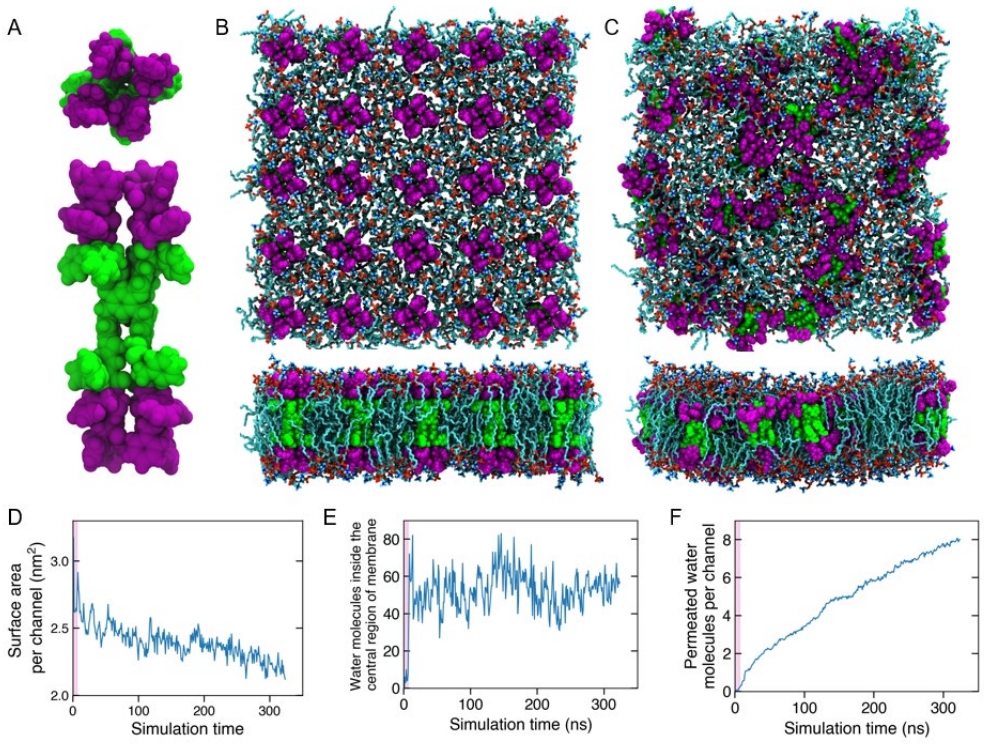

Figure A.4. Explicit-solvent MD simulation of PAH[4] monomer array. (A) The all-atom model of PAH[4] channel in van der Wall (vdW) representation. The hybrid[4]arene macromolecule and the nearest phenylalanine is shown in green and the remaining phenylalanine arms are shown in purple. (B) Instantaneous snapshot of an array of 25 PAH[4] embedded in pre-equilibrated POPC lipid bilayer membrane (14.4 × 14.4) nm at beginning of the MD simulation. (C) Snapshot of the system at the end of 320 ns of equilibrium MD simulation. In the panels of a - c, the top and bottom panel show the top and side view of the system respectively. Lipid molecules are shown as cyan molecular bonds. Water and ions are not shown for clarity. (D) The average surface area occupied by a channel as a function of simulation time. (E) The number of water molecules present in the central 1 nm wide region of the membrane as a function of simulation time. (F) The cumulative number of permeated water molecules with respect to the simulation time. In panels D – F, the shaded region indicates the first 5 ns of the equilibration simulation performed having all non-hydrogen atoms of the PAH[4] molecules harmonically restrained to their initial coordinates.

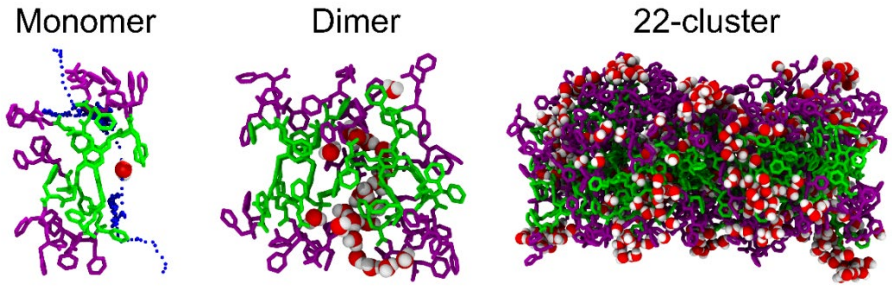

Figure A.5. Instantaneous MD snapshots of representative monomer, dimer and cluster configurations showing water permeation. Blue points in monomer structure show the path of water slipping through triPhe side chains, which was not continuous.

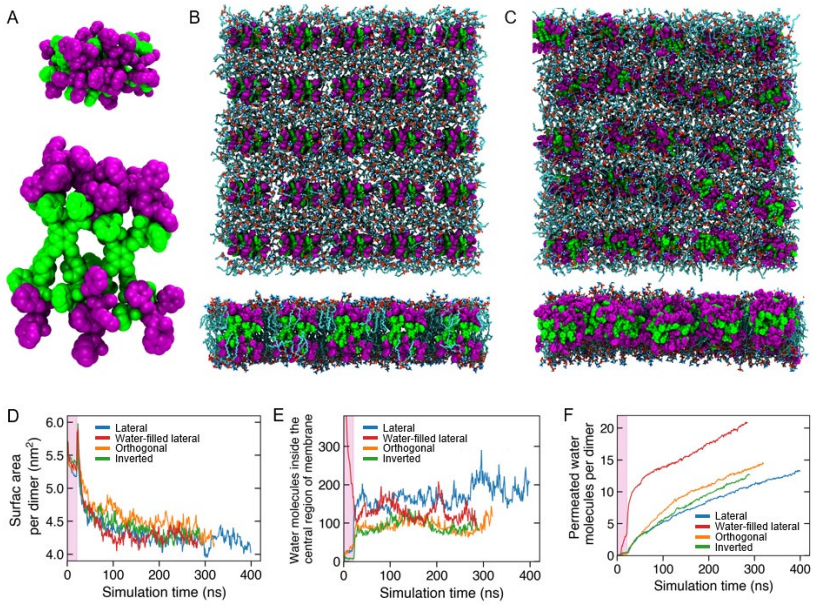

Figure A.6. Explicit-solvent MD simulation of PAH[4] dimer arrays. (A) The all-atom model of orthogonal PAH[4] dimer in vdW representation. (B) A snapshot of 25 PAH[4] dimers embedded into POPC lipid bilayer membrane at the beginning of the MD simulation. (C) Representative snapshot of the system (orthogonal dimer) at the end of 300 ns of equilibrium MD simulation. In the panels of a - c, the top and bottom panel show the top and side view of the system respectively. Water and ions are not shown for clarity. (D) The average surface area occupied by a dimer as a function of simulation time. (E) The number of water molecules present in the central 1 nm wide region of the membrane as a function of simulation time. (F) The cumulative number of permeated water molecules with respect to the simulation time. In panels D - F, the shaded region indicates the first 20 ns of the equilibration simulation performed having all non-hydrogen atoms of the PAH[4] molecules harmonically restrained to their initial coordinates.

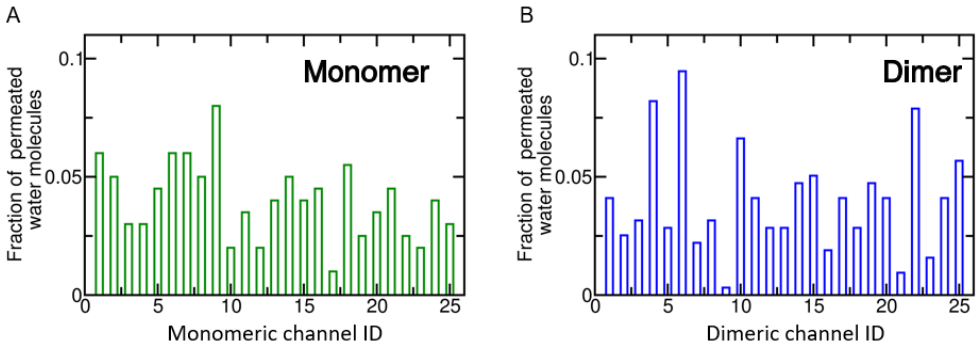

Figure A.7. Contribution of individual channels (A) or dimers (B) to total simulated water conductance. The histograms show the fraction of water molecules permeated through individual PAH[4] channels (A) or dimers (B); the dimers had orthogonal conformation.

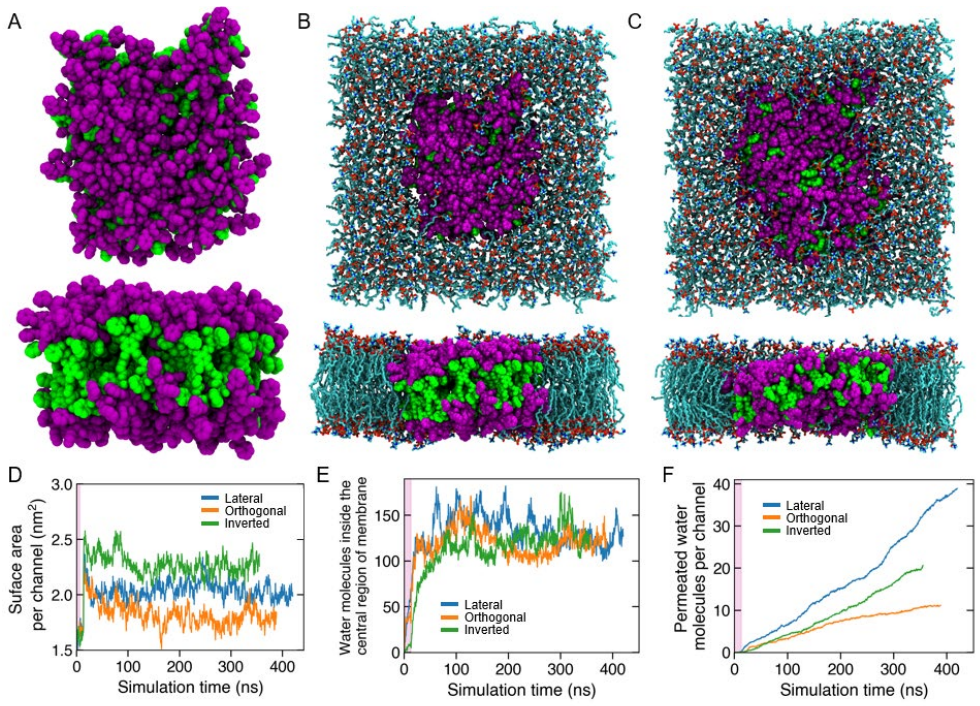

Figure A.8. Explicit-solvent MD simulation of pre-assembled PAH[4] clusters in a lipid bilayer membrane. (A) The all-atom model of pre-assembled PAH[4] cluster forming a "bouquet" like structure. (B) A snapshot of lateral PAH[4] clusters embedded into a pre-equilibrated POPC lipid bilayer membrane at the beginning of the MD simulation. (C) Representative snapshot of the system (lateral cluster) at the end of 400 ns of equilibrium MD simulation. In the panels of a - c, the top and bottom panel show the top and side view of the system respectively. Water and ions are not shown for clarity. (D) The average surface area occupied by a PAH[4] channel in a cluster as a function of simulation time. (E) The number of water molecules present in the central 1 nm wide region of the membrane with respect to the simulations time. (F) The cumulative number of permeated water molecules increases with respect to the simulation time. In panels d - f, the shaded region indicates the first 12 ns of the equilibration simulation performed having all non-hydrogen atoms of the PAH[4] molecules harmonically restrained to their initial coordinates.

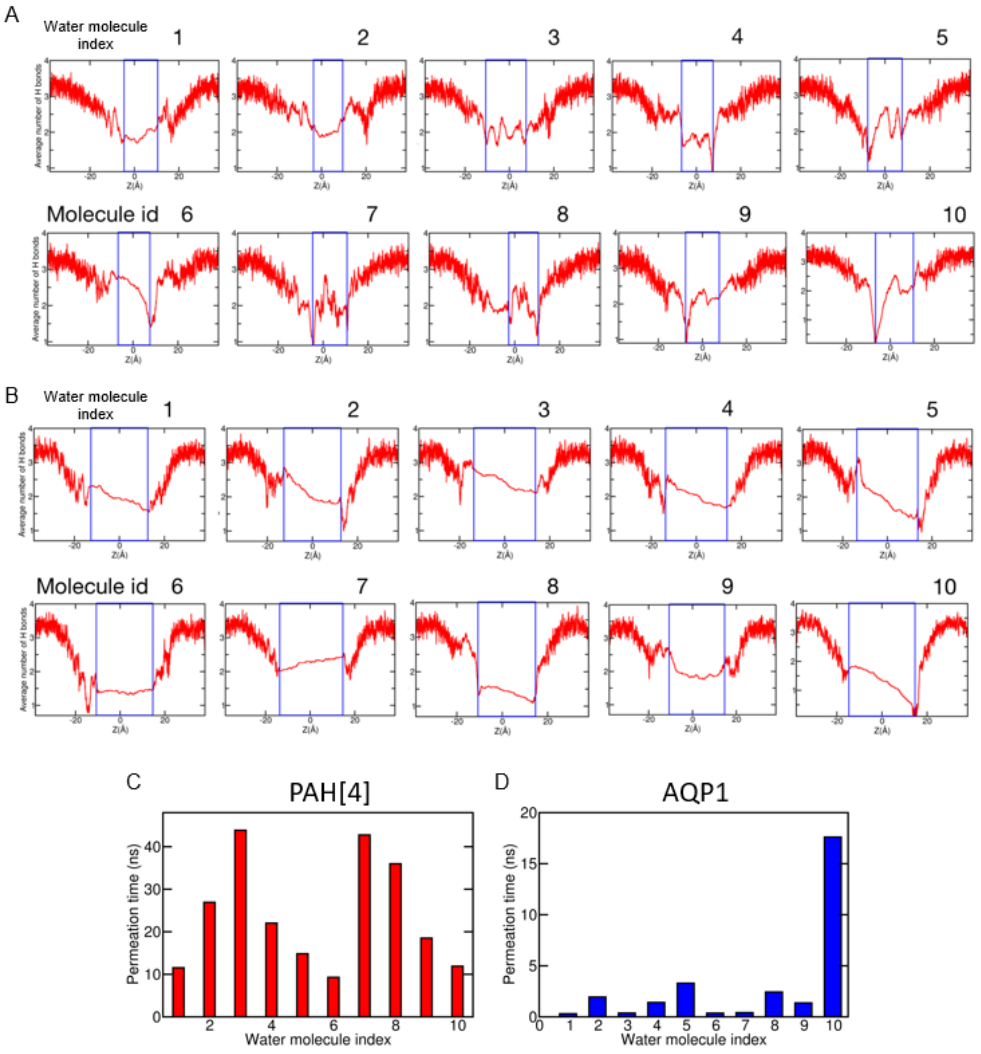

Figure A.9. The number of H-bonds formed by ten water molecules as a function of their Z coordinate that permeated through a PAH[4] cluster (A) or AQP1 tetramer (B). These water molecules were chosen randomly from a set of ~700 and 400 water molecules permeated through PAH[4] and AQP1, respectively. The blue box specifies the constriction region used to perform the calculation of the permeation time and the permeation path length. Panels C and D specify the permeation time for each water molecules.

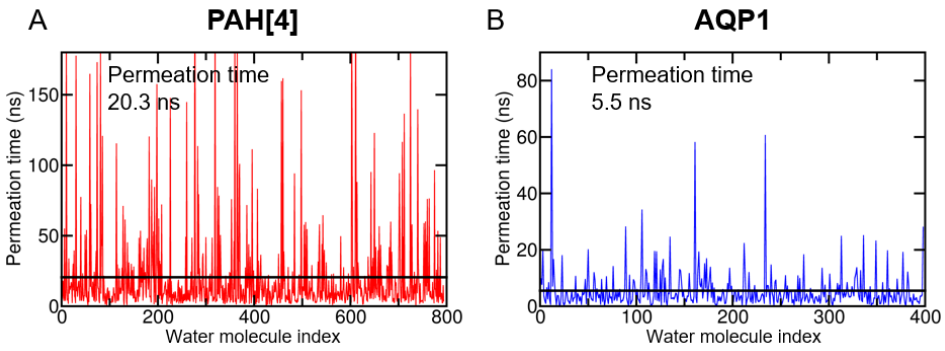

Figure A.10. The time taken by each water molecule to pass through the constriction of the (A) PAH[4] cluster and of (B) the AQP1 tetramer. The channel's constrictions were defined according to the average number of H-bonds plot within 9 and 14 Å of the membrane's midplane for PAH[4] and AQP1, respectively.

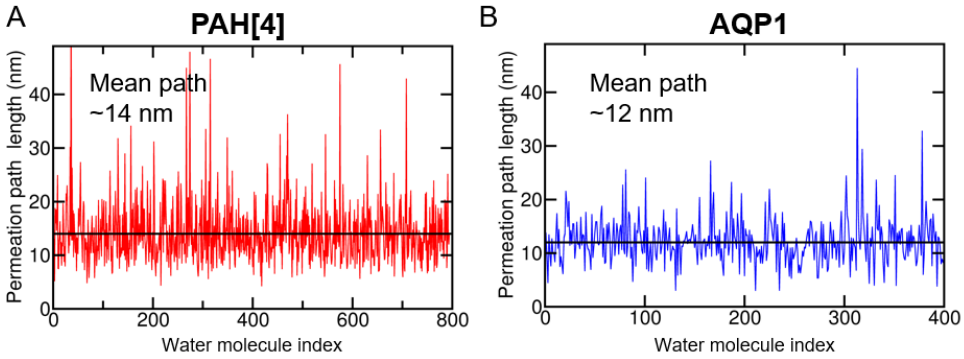

Figure A.11. The length of the path travelled by each water molecule through the constriction of (A) the PAH[4] and of (B) the AQP1 channels. To compute the average distance travelled by a water molecule, we first determined the average X and Y coordinates of each water molecule along the Z axis in 1Å bins and summed up the distance between the average water coordinates in the nearest bins (18 bins for PAH[4] and 28 bins for AQP1).

Appendix B: Supporting Information of SECTION 2[6]

This appendix provides the supporting information (calculation) for the PAP[5] channel based membranes discussed in SECTION 2.

[6] This appendix has been adapted from:
Song, W. Shen, Y.-x. Lang, C. Saha, P. Zenyuk, I.V. Hickey, R.J. and Kumar, M. Unique selectivity trends of highly permeable PAP[5] water channel membranes *Faraday Discussions* 209, 193-204 (2018).

Woochul Song (W.S.) conceived and designed the research. W.S. performed the experiments of channel-based membrane fabrication and transport study. W.S. analyzed the data. W.S. wrote the paper.

DEBYE LENGTH (λ_D) CALCULATION

The Debye length (λ_D , nm) of various ionic solutions is calculated by the Equation (B.1).

$$\lambda_D = \sqrt{\frac{\varepsilon_0 \varepsilon_r k_B T}{2 N_A e^2 I}} \tag{B.1}$$

where ε_0 and ε_r are vacuum and relative permittivity, k_B is the Boltzmann constant, T is the absolute temperature (K), N_A is the Avogadro's number, e is the elementary charge and I is the ionic strength of the solution [3]. The ionic strength of the solution is defined as Equation (B.2)

$$I = \frac{1}{2} \sum c_i {z_i}^2 \tag{B.2}$$

where c_i and z_i are molar concentration (M) and valence number of charged ions, respectively [4]. For the methyl blue dye rejection test, the ionic strength of the solutions was adjusted using NaCl.

DONNAN REJECTION CALCULATION

Theoretical Donnan rejections for various ionic solutes in Figure 45A were calculated by following Equation (B.3).

$$R = 1 - \left(\frac{|z_i| c_i}{|z_i| {c_i}^m + {c_x}^m} \right)^{|z_i / z_j|} \tag{B.3}$$

where c_i and ${c_i}^m$ are co-ion (same charge ions with membrane) concentrations of feed solution and membrane, ${c_x}^m$ is the charge concentration of the membrane, i and

j represents the opposite charge signs, and z is the ionic valence number. ${c_i}^m$ is generally adapted as the co-ion concentration of the permeate solution [5]. ${c_x}^m$ is obtained by fitting the experimental rejection value of $Ru(bipy)_3Cl_2$ (91.56 %) into Equation (B.3), as shown in the following calculation.

$$
\begin{aligned}
{c_x}^m &= \frac{|z_i|c_i}{(1-R)^{|z_j/z_i|}} - |z_i|{c_i}^m = \frac{|z_i|c_i}{(1-R)^{|z_j/z_i|}} - |z_i|\big(c_i \times (1-R)\big) \\
&= \frac{|2|(0.5\ mM)}{(1-0.9156)^{|1/2|}} - |2|\big(0.5\ mM \times (1-0.9156)\big) = 3.5mM
\end{aligned}
$$

CRITICAL FLUX (J_c) CALCULATION

The critical flux of the PAP[5] membranes were calculated by the Equation (B.4).

$$J_c = \frac{\varepsilon k_B T}{\eta {R_p}^2} \tag{B.4}$$

where ε is the porosity of the ML-PAP[5] membrane, η is the viscosity of the solution and R_p is the pore radius of the membrane. For the PAP[5] membranes, within a $1\ \mu m \times 1\ \mu m$ unit area, the actual channel number is $\sim 4.2 \times 10^5$ and the pore radius was adapted from the radius of confined pillar[5]arene of the PAP[5] channels (0.25 nm) [6]. Therefore, the ε is calculated as Equation (B.5)

$$\varepsilon = \frac{4.2\times10^5 \times \pi r^2}{1\ \mu m \times 1\ \mu m} = 0.0824 \tag{B.5}$$

and the J_c is calculated as Equation (B.6)

$$J_c = \frac{0.0824\times1.38\times10^{-23} m^2 kg s^{-2} K^{-1} \times 293K}{(0.25\times10^{-9} nm)^2 \times 0.001 kg m^{-1} s^{-1}} \times \frac{mol\ H_2O}{0.000018\ m^3} = 296{,}000\ {}^{mol}/_{m^2 s} \tag{B.6}$$

Appendix C: Supporting Information of SECTION 3

This appendix provides the supporting information of TFC membrane developments discussed in SECTION 3.

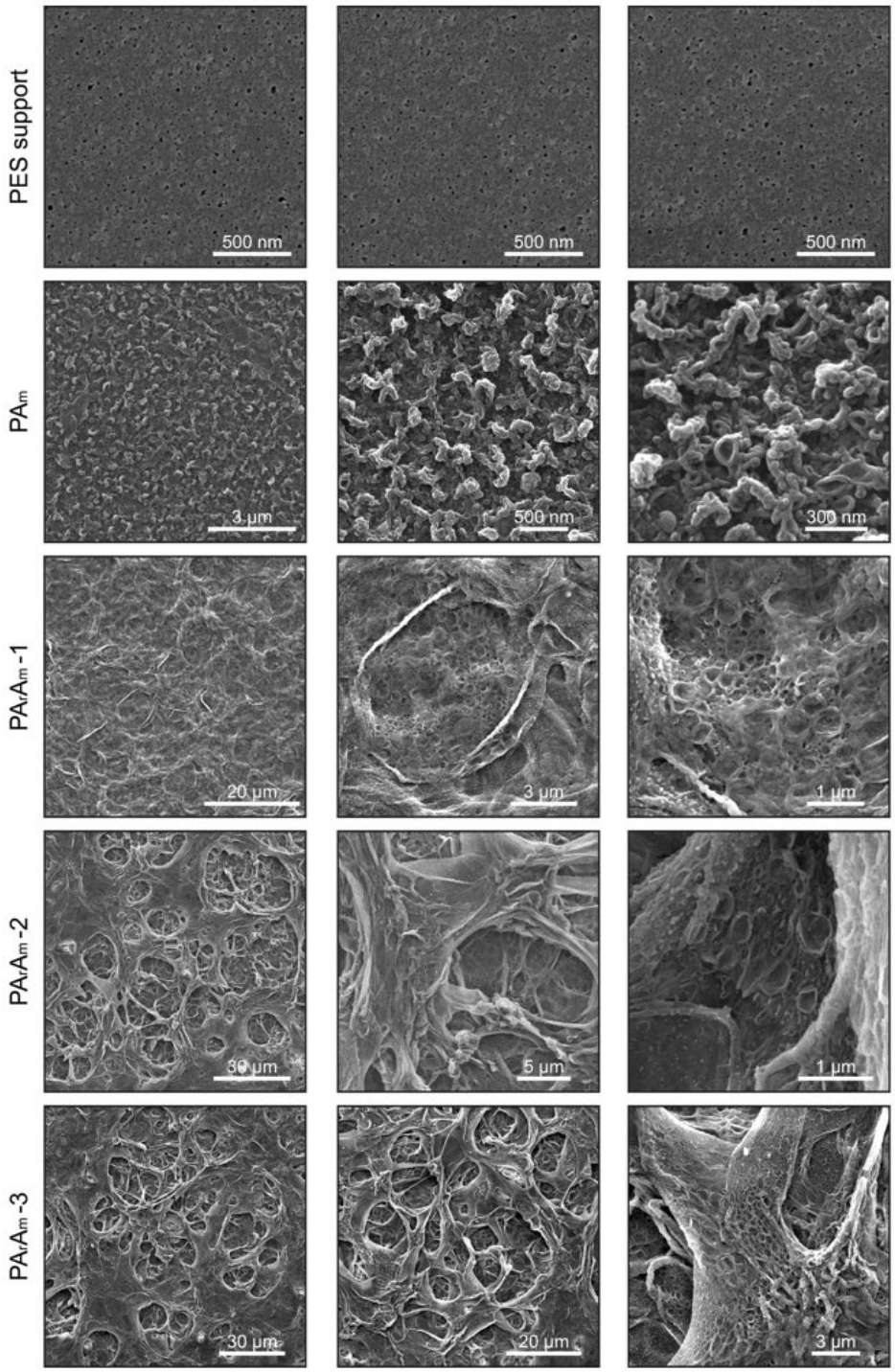

Figure C.1. Top-view SEM images of PES support, PA_m, PA_rA_m-1, PA_rA_m-2, and PA_rA_m-3 membranes.

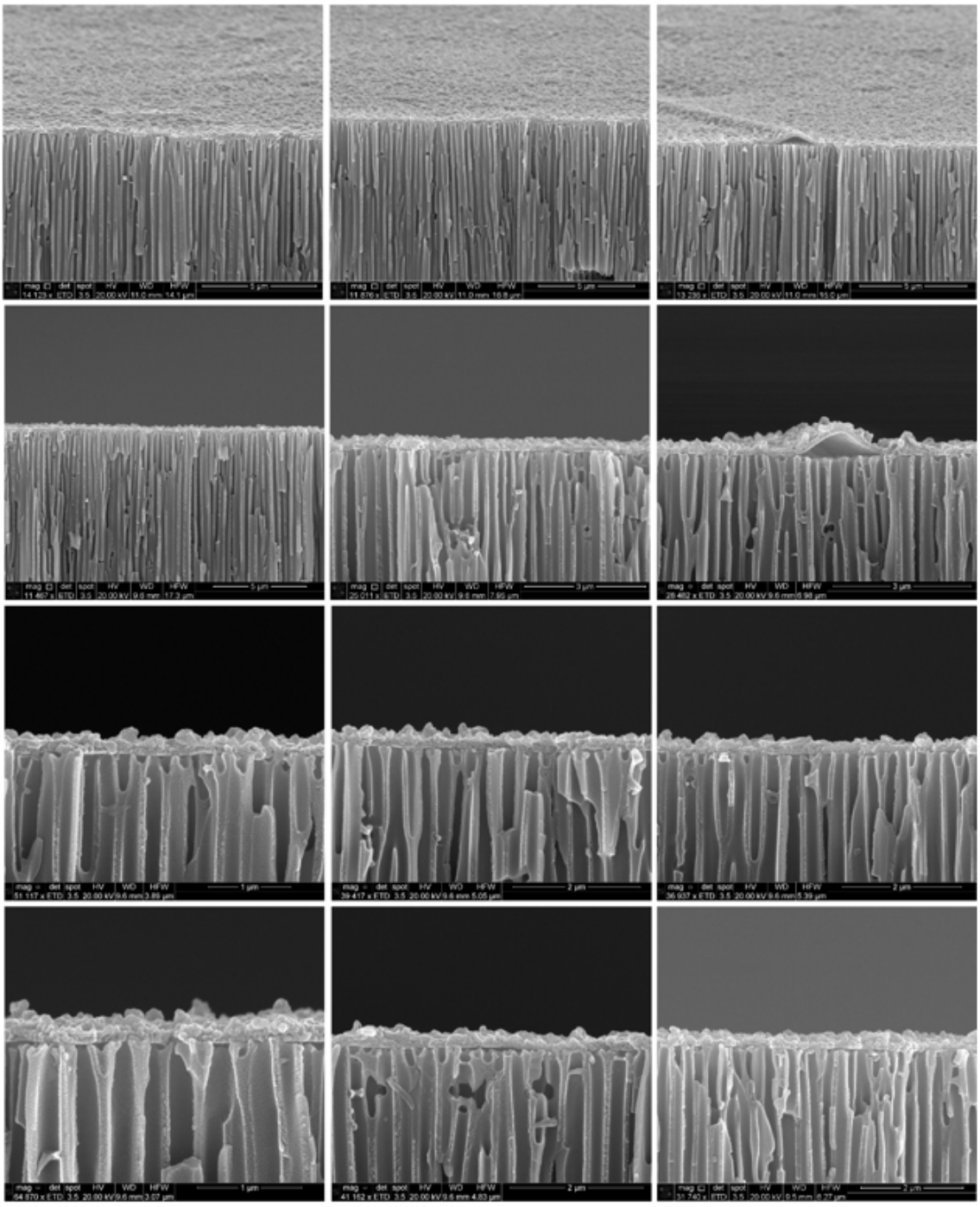

Figure C.2. Cross-sectional SEM images of AO-supported PA_m polymer films.

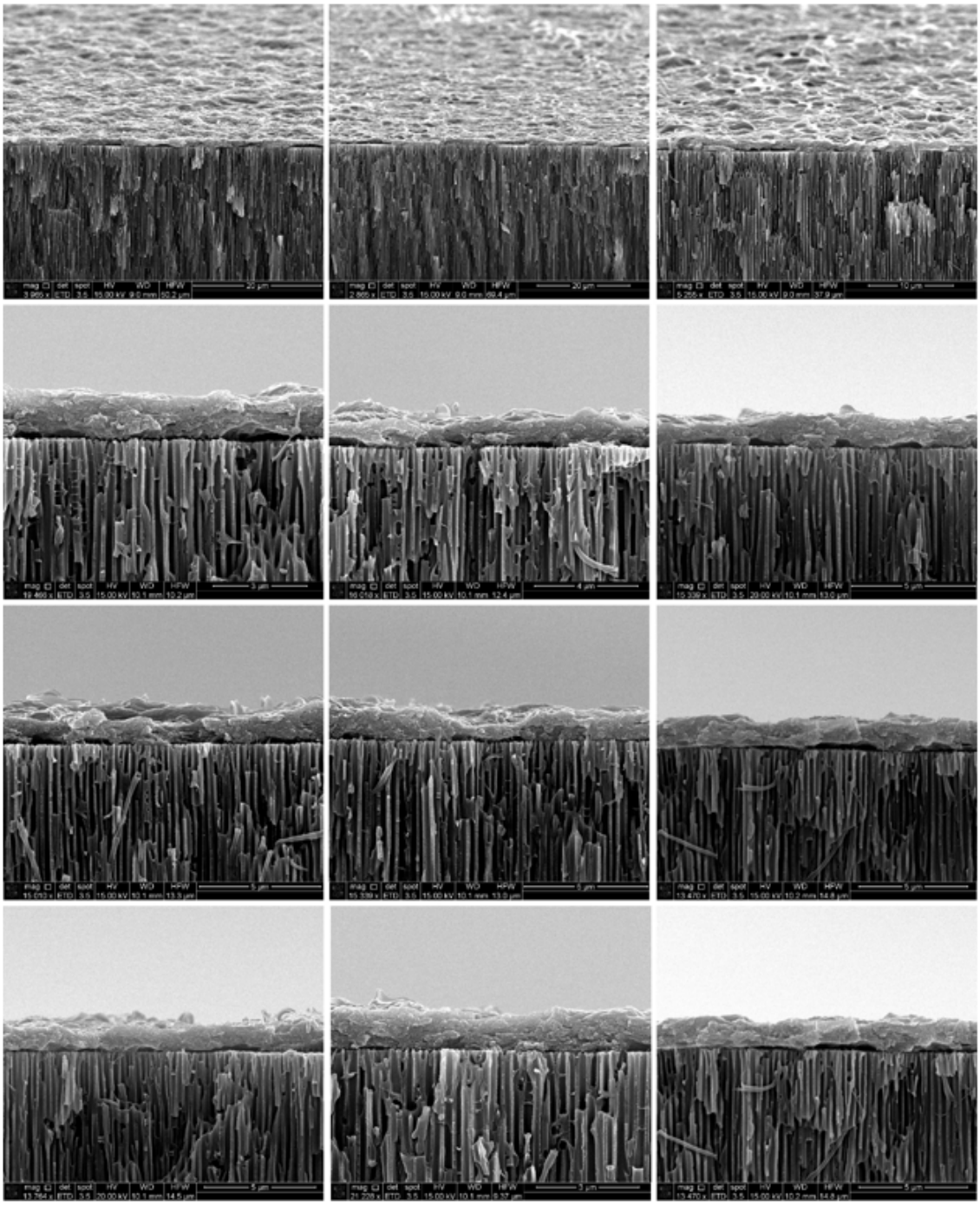

Figure C.3. Cross-sectional SEM images of AO-supported PA_rA_m-1 polymer films.

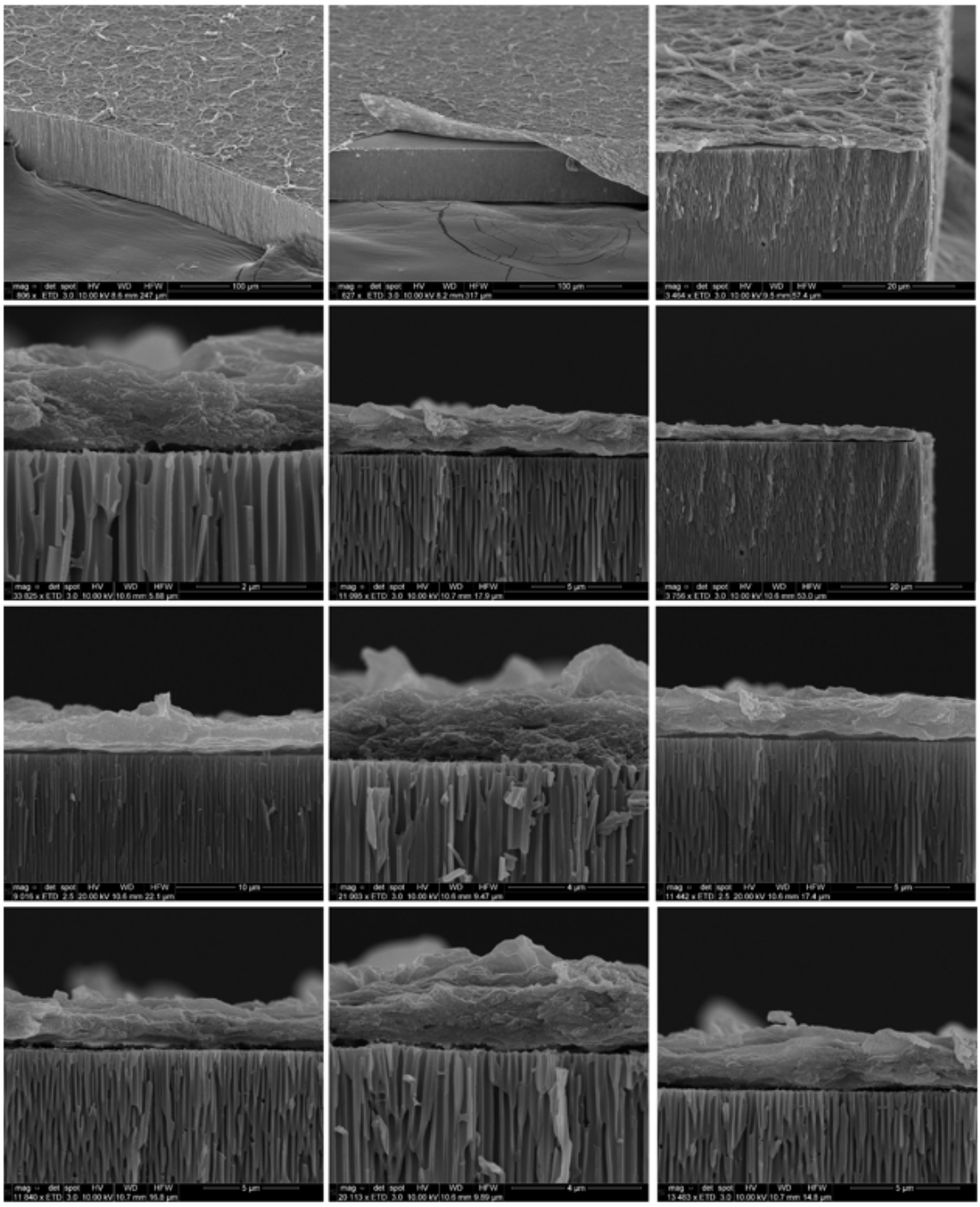

Figure C.4. Tilted and cross-sectional SEM images of AO-supported PA_rA_m-2 polymer films.

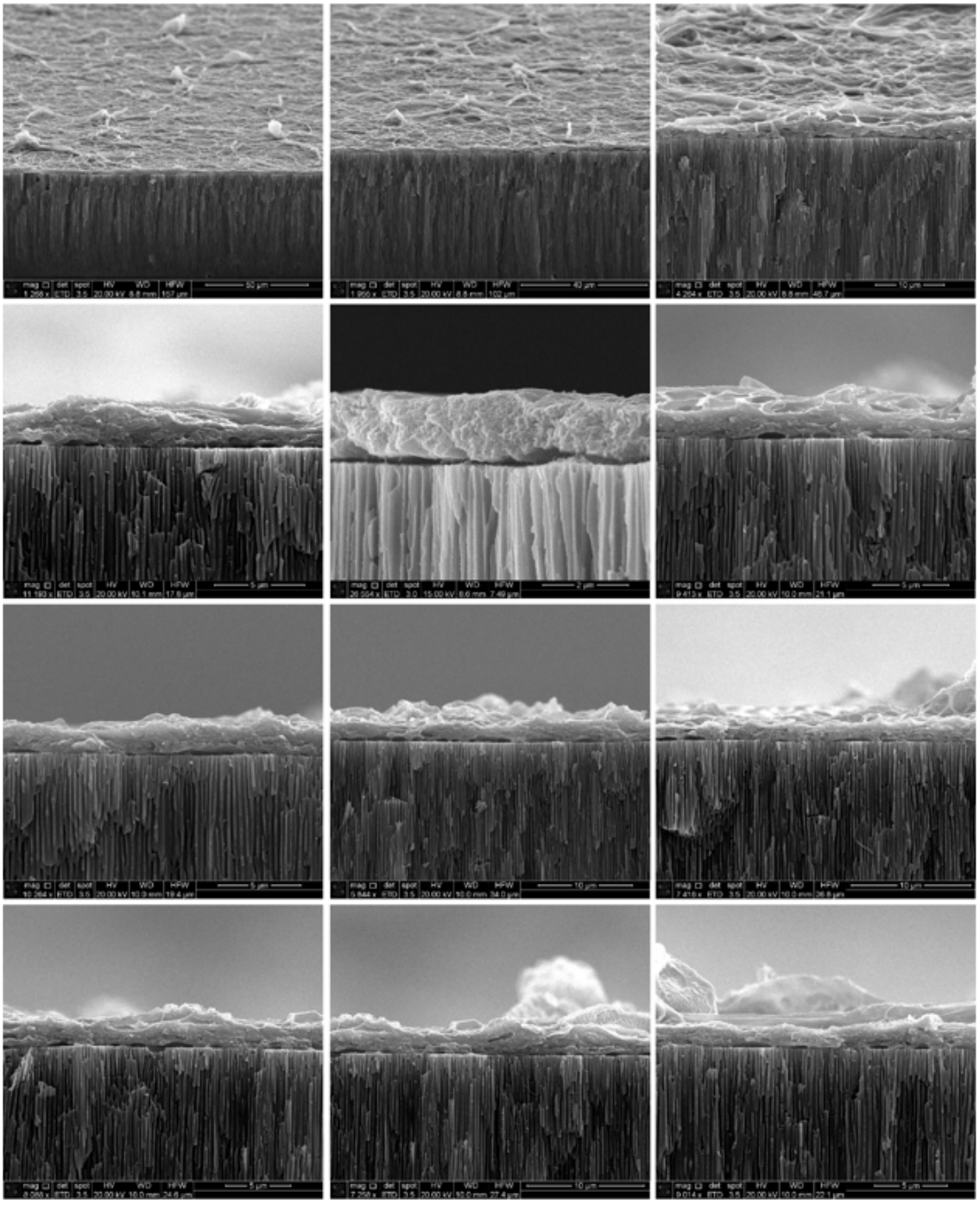

Figure C.5. Tilted and cross-sectional SEM images of AO-supported PA_rA_m-3 polymer films.

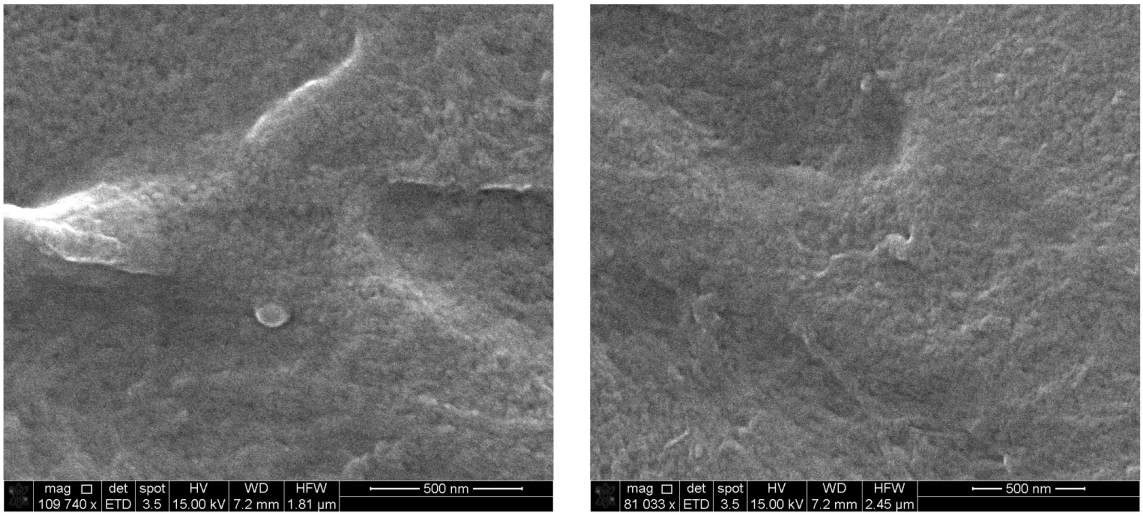

Figure C.6. Top-view SEM images of PA_r TFC membranes which show the continuous film formation by interfacial polymerization of P[5]s and TMCs without MPDs.

REFERENCES

[1] Boinski, T., Cieszkowski, A., Rosa, B., Szumna, A., Hybrid [n]Arenes through Thermodynamically Driven Macrocyclization Reactions, The Journal of Organic Chemistry 80(7) (2015) 3488-3495.

[2] Chowdhury, R., Ren, T., Shankla, M., Decker, K., Grisewood, M., Prabhakar, J., Baker, C., Golbeck, J.H., Aksimentiev, A., Kumar, M., Maranas, C.D., PoreDesigner for tuning solute selectivity in a robust and highly permeable outer membrane pore, Nature Communications 9(1) (2018) 3661.

[3] Fornasiero, F., Park, H.G., Holt, J.K., Stadermann, M., Grigoropoulos, C.P., Noy, A., Bakajin, O., Ion exclusion by sub-2-nm carbon nanotube pores, Proceedings of the National Academy of Sciences 105(45) (2008) 17250-17255.

[4] Annual Index for Volume 78, 2001, Journal of Chemical Education 78(12) (2001) 1713.

[5] Latulippe, D.R., Ager, K., Zydney, A.L., Flux-dependent transmission of supercoiled plasmid DNA through ultrafiltration membranes, Journal of Membrane Science 294(1) (2007) 169-177.

[6] Shen, Y.-x., Si, W., Erbakan, M., Decker, K., De Zorzi, R., Saboe, P.O., Kang, Y.J., Majd, S., Butler, P.J., Walz, T., Aksimentiev, A., Hou, J.-l., Kumar, M., Highly permeable artificial water channels that can self-assemble into two-dimensional arrays, Proceedings of the National Academy of Sciences, USA 112(32) (2015) 9810-9815.

Bibliography

Abbott, L.J., Hart, K.E., Colina, C.M., Polymatic: a generalized simulated polymerization algorithm for amorphous polymers, Theoretical Chemistry Accounts 132(3) (2013) 1334.

Abraham, J., Vasu, K.S., Williams, C.D., Gopinadhan, K., Su, Y., Cherian, C.T., Dix, J., Prestat, E., Haigh, S.J., Grigorieva, I.V., Carbone, P., Geim, A.K., Nair, R.R., Tunable sieving of ions using graphene oxide membranes, Nature Nanotechnology 12(6) (2017) 546-550.

Ali, Z., Ghanem, B.S., Wang, Y., Pacheco, F., Ogieglo, W., Vovusha, H., Genduso, G., Schwingenschlögl, U., Han, Y., Pinnau, I., Finely Tuned Submicroporous Thin-Film Molecular Sieve Membranes for Highly Efficient Fluid Separations, Advanced Materials 32(22) (2020) 2001132.

Ali, Z., Pacheco, F., Litwiller, E., Wang, Y., Han, Y., Pinnau, I., Ultra-selective defect-free interfacially polymerized molecular sieve thin-film composite membranes for H2 purification, Journal of Materials Chemistry A 6(1) (2018) 30-35.

Ali, Z., Wang, Y., Ogieglo, W., Pacheco, F., Vovusha, H., Han, Y., Pinnau, I., Gas separation and water desalination performance of defect-free interfacially polymerized para-linked polyamide thin-film composite membranes, Journal of Membrane Science 618 (2021) 118572.

Andersen, H.C., Rattle: A "velocity" version of the shake algorithm for molecular dynamics calculations, Journal of Computational Physics 52(1) (1983) 24-34.

Baaden, M., Barboiu, M., Bill, R.M., Casanova, S., Chen, C.-L., Conner, M., Freger, V., Gong, B., Góra, A., Hinds, B., Horner, A., Hummer, G., Kumar, M., Lokesh, M., Mitra, S., Noy, A., Pohl, P., Sadet, A., Sansom, M., Törnroth-Horsefield, S., Vashisth, H., Structure and function of natural proteins for water transport: general discussion, Faraday Discussions 209(0) (2018) 83-95.

Baaden, M., Barboiu, M., Bill, R.M., Chen, C.-L., Davis, J., Di Vincenzo, M., Freger, V., Fröba, M., Gale, P.A., Gong, B., Hélix-Nielsen, C., Hickey, R., Hinds, B., Hou, J.-L., Hummer, G., Kumar, M., Legrand, Y.-M., Lokesh, M., Mi, B., Murail, S., Pohl, P., Sansom, M., Song, Q., Song, W., Törnroth-Horsefield, S., Vashisth, H., Vögele, M., Biomimetic water channels: general discussion, Faraday Discussions 209(0) (2018) 205-229.

Baker, R.W., Future Directions of Membrane Gas Separation Technology, Industrial & Engineering Chemistry Research 41(6) (2002) 1393-1411.

Baker, R.W., Low, B.T., Gas Separation Membrane Materials: A Perspective, Macromolecules 47(20) (2014) 6999-7013.

Barboiu, M., Artificial Water Channels, Angewandte Chemie International Edition 51(47) (2012) 11674-11676.

Barboiu, M., Artificial water channels – incipient innovative developments, Chemical Communications 52(33) (2016) 5657-5665.

Barboiu, M., Gilles, A., From Natural to Bioassisted and Biomimetic Artificial Water Channel Systems, Accounts of Chemical Research 46(12) (2013) 2814-2823.

Barboiu, M., Le Duc, Y., Gilles, A., Cazade, P.-A., Michau, M., Marie Legrand, Y., van der Lee, A., Coasne, B., Parvizi, P., Post, J., Fyles, T., An artificial primitive mimic of the Gramicidin-A channel, Nature Communications 5(1) (2014) 4142.

Berezhkovskii, A., Hummer, G., Single-File Transport of Water Molecules through a Carbon Nanotube, Physical Review Letters 89(6) (2002) 064503.

Best, R.B., Zhu, X., Shim, J., Lopes, P.E., Mittal, J., Feig, M., MacKerell Jr, A.D., Optimization of the additive CHARMM all-atom protein force field targeting improved sampling of the backbone ϕ, ψ and side-chain $\chi 1$ and $\chi 2$ dihedral angles, Journal of Chemical Theory and Computation 8(9) (2012) 3257-3273.

Biwersi, J., Tulk, B., Verkman, A.S., Long-Wavelength Chloride-Sensitive Fluorescent Indicators, Analytical Biochemistry 219(1) (1994) 139-143.

Boinski, T., Cieszkowski, A., Rosa, B., Szumna, A., Hybrid [n]Arenes through Thermodynamically Driven Macrocyclization Reactions, The Journal of Organic Chemistry 80(7) (2015) 3488-3495.

Borgnia, M.J., Kozono, D., Calamita, G., Maloney, P.C., Agre, P., Functional reconstitution and characterization of AqpZ, the E. coli water channel protein11Edited by W. Baumeister, Journal of Molecular Biology 291(5) (1999) 1169-1179.

Boussu, K., Van der Bruggen, B., Volodin, A., Van Haesendonck, C., Delcour, J.A., Van der Meeren, P., Vandecasteele, C., Characterization of commercial nanofiltration membranes and comparison with self-made polyethersulfone membranes, Desalination 191(1) (2006) 245-253.

Chen, D., Werber, J.R., Zhao, X., Elimelech, M., A facile method to quantify the carboxyl group areal density in the active layer of polyamide thin-film composite membranes, Journal of Membrane Science 534 (2017) 100-108.

Chen, L., Si, W., Zhang, L., Tang, G., Li, Z.-T., Hou, J.-L., Chiral Selective Transmembrane Transport of Amino Acids through Artificial Channels, Journal of the American Chemical Society 135(6) (2013) 2152-2155.

Chowdhury, R., Ren, T., Shankla, M., Decker, K., Grisewood, M., Prabhakar, J., Baker, C., Golbeck, J.H., Aksimentiev, A., Kumar, M., Maranas, C.D., PoreDesigner for tuning solute selectivity in a robust and highly permeable outer membrane pore, Nature Communications 9(1) (2018) 3661.

Chui, J.K.W., Fyles, T.M., Ionic conductance of synthetic channels: analysis, lessons, and recommendations, Chemical Society Reviews 41(1) (2012) 148-175.

Colton, C.K., Smith, K.A., Mass transfer to a rotating fluid. Part II. Transport from the base of an agitated cylindrical tank, AIChE Journal 18(5) (1972) 958-967.

Conway, B.E., Ionic hydration in chemistry and biophysics, Elsevier Scientific Pub. Co.1981.

Coronell, O., Mariñas, B.J., Cahill, D.G., Accessibility and Ion Exchange Stoichiometry of Ionized Carboxylic Groups in the Active Layer of FT30 Reverse Osmosis Membrane, Environmental Science & Technology 43(13) (2009) 5042-5048.

Coronell, O., Mariñas, B.J., Zhang, X., Cahill, D.G., Quantification of Functional Groups and Modeling of Their Ionization Behavior in the Active Layer of FT30 Reverse Osmosis Membrane, Environmental Science & Technology 42(14) (2008) 5260-5266.

Culp, T.E., Khara, B., Brickey, K.P., Geitner, M., Zimudzi, T.J., Wilbur, J.D., Jons, S.D., Roy, A., Paul, M., Ganapathysubramanian, B., Zydney, A.L., Kumar, M., Gomez, E.D., Nanoscale control of internal inhomogeneity enhances water transport in desalination membranes, Science 371(6524) (2021) 72-75.

Culp, T.E., Shen, Y.-x., Geitner, M., Paul, M., Roy, A., Behr, M.J., Rosenberg, S., Gu, J., Kumar, M., Gomez, E.D., Electron tomography reveals details of the internal microstructure of desalination membranes, Proceedings of the National Academy of Sciences 115(35) (2018) 8694-8699.

Daoudi, S., Brochard, F., Flows of Flexible Polymer Solutions in Pores, Macromolecules 11(4) (1978) 751-758.

De Cola, C., Licen, S., Comegna, D., Cafaro, E., Bifulco, G., Izzo, I., Tecilla, P., De Riccardis, F., Size-dependent cation transport by cyclic α-peptoid ion carriers, Organic & Biomolecular Chemistry 7(14) (2009) 2851-2854.

Deamer, D.W., Bramhall, J., Permeability of lipid bilayers to water and ionic solutes, Chemistry and Physics of Lipids 40(2) (1986) 167-188.

Dean, D.C., O'Muircheartaigh, J., Dirks, H., Waskiewicz, N., Lehman, K., Walker, L., Han, M., Deoni, S.C.L., Modeling healthy male white matter and myelin development: 3 through 60months of age, NeuroImage 84 (2014) 742-752.

Decker, K., Page, M., Boyd, A., MacAllister, I., Ginsberg, M., Aksimentiev, A., Selective Permeability of Truncated Aquaporin 1 in Silico, ACS Biomaterials Science & Engineering 3(3) (2017) 342-348.

Disalvo, E.A., Simon, S.A., Permeability and Stability of Lipid Bilayers, Taylor & Francis1995.

Discher, D.E., Eisenberg, A., Polymer Vesicles, Science 297(5583) (2002) 967-973.

Donnan, F.G., The Theory of Membrane Equilibria, Chemical Reviews 1(1) (1924) 73-90.

Dubbeldam, D., Calero, S., Ellis, D.E., Snurr, R.Q., RASPA: molecular simulation software for adsorption and diffusion in flexible nanoporous materials, Molecular Simulation 42(2) (2016) 81-101.

Elimelech, M., Phillip, W.A., The Future of Seawater Desalination: Energy, Technology, and the Environment, Science 333(6043) (2011) 712-717.

Entzminger, K.C., Hyun, J.-m., Pantazes, R.J., Patterson-Orazem, A.C., Qerqez, A.N., Frye, Z.P., Hughes, R.A., Ellington, A.D., Lieberman, R.L., Maranas, C.D., Maynard, J.A., De novo design of antibody complementarity determining regions binding a FLAG tetra-peptide, Scientific Reports 7(1) (2017) 10295.

Erbakan, M., Shen, Y.-x., Grzelakowski, M., Butler, P.J., Kumar, M., Curtis, W.R., Molecular Cloning, Overexpression and Characterization of a Novel Water Channel Protein from Rhodobacter sphaeroides, PLOS ONE 9(1) (2014) e86830.

Erickson, H.P., Size and Shape of Protein Molecules at the Nanometer Level Determined by Sedimentation, Gel Filtration, and Electron Microscopy, Biological Procedures Online 11(1) (2009) 32.

Feller, S.E., Zhang, Y., Pastor, R.W., Brooks, B.R., Constant pressure molecular dynamics simulation: the Langevin piston method, Journal of Chemical Physics 103(11) (1995) 4613-4621.

Feng, W.-X., Sun, Z., Barboiu, M., Pillar[n]arenes for Construction of Artificial Transmembrane Channels, Israel Journal of Chemistry 58(11) (2018) 1209-1218.

Feroz, H., Vandervelden, C., Ikwuagwu, B., Ferlez, B., Baker, C.S., Lugar, D.J., Grzelakowski, M., Golbeck, J.H., Zydney, A.L., Kumar, M., Concentrating membrane proteins using ultrafiltration without concentrating detergents, Biotechnology and Bioengineering 113(10) (2016) 2122-2130.

Fornasiero, F., Park, H.G., Holt, J.K., Stadermann, M., Grigoropoulos, C.P., Noy, A., Bakajin, O., Ion exclusion by sub-2-nm carbon nanotube pores, Proceedings of the National Academy of Sciences 105(45) (2008) 17250-17255.

Galizia, M., Chi, W.S., Smith, Z.P., Merkel, T.C., Baker, R.W., Freeman, B.D., 50th Anniversary Perspective: Polymers and Mixed Matrix Membranes for Gas and Vapor Separation: A Review and Prospective Opportunities, Macromolecules 50(20) (2017) 7809-7843.

Geise, G.M., Why polyamide reverse-osmosis membranes work so well, Science 371(6524) (2021) 31-32.

Geise, G.M., Park, H.B., Sagle, A.C., Freeman, B.D., McGrath, J.E., Water permeability and water/salt selectivity tradeoff in polymers for desalination, Journal of Membrane Science 369(1) (2011) 130-138.

Gravelle, S., Joly, L., Detcheverry, F., Ybert, C., Cottin-Bizonne, C., Bocquet, L., Optimizing water permeability through the hourglass shape of aquaporins, Proceedings of the National Academy of Sciences 110(41) (2013) 16367-16372.

Hancher, C.W., Ryon, A.D., Evaluation of ultrafiltration membranes with biological macromolecules, Biotechnology and Bioengineering 15(4) (1973) 677-692.

Hannesschläger, C., Barta, T., Siligan, C., Horner, A., Quantification of Water Flux in Vesicular Systems, Scientific Reports 8(1) (2018) 8516.

Higuchi, A., Kato, K., Hara, M., Sato, T., Ishikawa, G., Nakano, H., Satoh, S., Manabe, S.-i., Rejection of single stranded and double stranded DNA by porous hollow fiber membranes, Journal of Membrane Science 116(2) (1996) 191-197.

Hinch, E.J., Mechanical models of dilute polymer solutions in strong flows, The Physics of Fluids 20(10) (1977) S22-S30.

Hirasaki, T., Sato, T., Tsuboi, T., Nakano, H., Noda, T., Kono, A., Yamaguchi, K., Imada, K., Yamamoto, N., Murakami, H., Manabe, S.-i., Permeation mechanism of DNA molecules in solution through cuprammonium regenerated cellulose hollow fiber (BMMtm), Journal of Membrane Science 106(1) (1995) 123-129.

Holt, J.K., Park, H.G., Wang, Y., Stadermann, M., Artyukhin, A.B., Grigoropoulos, C.P., Noy, A., Bakajin, O., Fast Mass Transport Through Sub-2-Nanometer Carbon Nanotubes, Science 312(5776) (2006) 1034-1037.

Horner, A., Pohl, P., Comment on "Enhanced water permeability and tunable ion selectivity in subnanometer carbon nanotube porins", Science 359(6383) (2018).

Horner, A., Pohl, P., Single-file transport of water through membrane channels, Faraday Discussions 209(0) (2018) 9-33.

Horner, A., Zocher, F., Preiner, J., Ollinger, N., Siligan, C., Akimov, S.A., Pohl, P., The mobility of single-file water molecules is governed by the number of H-bonds they may form with channel-lining residues, Science Advances 1(2) (2015).

Hu, X.-B., Chen, Z., Tang, G., Hou, J.-L., Li, Z.-T., Single-Molecular Artificial Transmembrane Water Channels, Journal of the American Chemical Society 134(20) (2012) 8384-8387.

Hummer, G., Rasaiah, J.C., Noworyta, J.P., Water conduction through the hydrophobic channel of a carbon nanotube, Nature 414(6860) (2001) 188-190.

Humphrey, J.L., Keller, G.E., Separation process technology, (1997).

Humphrey, W., Dalke, A., Schulten, K., VMD: Visual molecular dynamics, Journal of Molecular Graphics and Modelling 14(1) (1996) 33-38.

Jimenez-Solomon, M.F., Song, Q., Jelfs, K.E., Munoz-Ibanez, M., Livingston, A.G., Polymer nanofilms with enhanced microporosity by interfacial polymerization, Nature Materials 15(7) (2016) 760-767.

Jo, S., Kim, T., Iyer, V.G., Im, W., CHARMM-GUI: a web-based graphical user interface for CHARMM, Journal of Computational Chemistry 29(11) (2008) 1859-1865.

Jordan, S.M., Koros, W.J., Permeability of pure and mixed gases in silicone rubber at elevated pressures, Journal of Polymer Science Part B: Polymer Physics 28(6) (1990) 795-809.

Jorgensen, W.L., Chandrasekhar, J., Madura, J.D., Impey, R.W., Klein, M.L., Comparison of simple potential function for simulating liquid water, Journal of Chemical Physics 79(2) (1983) 926-935.

Kahn, D.W., Butler, M.D., Cohen, D.L., Gordon, M., Kahn, J.W., Winkler, M.E., Purification of plasmid DNA by tangential flow filtration, Biotechnology and Bioengineering 69(1) (2000) 101-106.

Kaucher, M.S., Peterca, M., Dulcey, A.E., Kim, A.J., Vinogradov, S.A., Hammer, D.A., Heiney, P.A., Percec, V., Selective Transport of Water Mediated by Porous Dendritic Dipeptides, Journal of the American Chemical Society 129(38) (2007) 11698-11699.

Ke, J., Zhang, Y., Zhang, X., Liu, Y., Ji, Y., Chen, J., Novel chiral composite membrane prepared via the interfacial polymerization of diethylamino-beta-cyclodextrin for the enantioseparation of chiral drugs, Journal of Membrane Science 597 (2020) 117635.

Khodabakhshi, M., Moosavi, A., Unidirectional Transport of Water through an Asymmetrically Charged Rotating Carbon Nanotube, The Journal of Physical Chemistry C 121(42) (2017) 23649-23658.

Kim, S., Lee, J., Jo, S., Brooks III, C.L., Lee, H.S., Im, W., CHARMM-GUI ligand reader and modeler for CHARMM force field generation of small molecules, Journal of Computational Chemistry 38(21) (2017) 1879-1886.

Klara, S.S., Saboe, P.O., Sines, I.T., Babaei, M., Chiu, P.-L., DeZorzi, R., Dayal, K., Walz, T., Kumar, M., Mauter, M.S., Magnetically Directed Two-Dimensional Crystallization of OmpF Membrane Proteins in Block Copolymers, Journal of the American Chemical Society 138(1) (2016) 28-31.

Klauda, J.B., Venable, R.M., Freites, J.A., O'Connor, J.W., Tobias, D.J., Mondragon-Ramirez, C., Vorobyov, I., MacKerell Jr, A.D., Pastor, R.W., Update of the CHARMM all-atom additive force field for lipids: validation on six lipid types, Journal of Physical Chemistry B 114(23) (2010) 7830-7843.

Koros, W.J., Zhang, C., Materials for next-generation molecularly selective synthetic membranes, Nature Materials 16(3) (2017) 289-297.

Kosinov, N., Gascon, J., Kapteijn, F., Hensen, E.J.M., Recent developments in zeolite membranes for gas separation, Journal of Membrane Science 499 (2016) 65-79.

Koutsou, C.P., Karabelas, A.J., Shear stresses and mass transfer at the base of a stirred filtration cell and corresponding conditions in narrow channels with spacers, Journal of Membrane Science 399-400 (2012) 60-72.

Kremer, K., Binder, K., Dynamics of polymer chains confined into tubes: Scaling theory and Monte Carlo simulations, The Journal of Chemical Physics 81(12) (1984) 6381-6394.

Kumar, M., Habel, J.E.O., Shen, Y.-x., Meier, W.P., Walz, T., High-Density Reconstitution of Functional Water Channels into Vesicular and Planar Block

Copolymer Membranes, Journal of the American Chemical Society 134(45) (2012) 18631-18637.

Lang, C., Li, W., Dong, Z., Zhang, X., Yang, F., Yang, B., Deng, X., Zhang, C., Xu, J., Liu, J., Biomimetic Transmembrane Channels with High Stability and Transporting Efficiency from Helically Folded Macromolecules, Angewandte Chemie International Edition 55(33) (2016) 9723-9727.

Latimer, P., Pyle, B.E., Light Scattering at Various Angles: Theoretical Predictions of the Effects of Particle Volume Changes, Biophysical journal 12(7) (1972) 764-773.

Latulippe, D.R., Ager, K., Zydney, A.L., Flux-dependent transmission of supercoiled plasmid DNA through ultrafiltration membranes, Journal of Membrane Science 294(1) (2007) 169-177.

Latulippe, D.R., Zydney, A.L., Elongational flow model for transmission of supercoiled plasmid DNA during membrane ultrafiltration, Journal of Membrane Science 329(1) (2009) 201-208.

Le Duc, Y., Michau, M., Gilles, A., Gence, V., Legrand, Y.-M., van der Lee, A., Tingry, S., Barboiu, M., Imidazole-Quartet Water and Proton Dipolar Channels, Angewandte Chemie International Edition 50(48) (2011) 11366-11372.

Licsandru, E., Kocsis, I., Shen, Y.-x., Murail, S., Legrand, Y.-M., van der Lee, A., Tsai, D., Baaden, M., Kumar, M., Barboiu, M., Salt-Excluding Artificial Water Channels Exhibiting Enhanced Dipolar Water and Proton Translocation, Journal of the American Chemical Society 138(16) (2016) 5403-5409.

Long, T.D., Anderson, J.L., Flow-dependent rejection of polystyrene from microporous membranes, Journal of Polymer Science: Polymer Physics Edition 22(7) (1984) 1261-1281.

Louie, J.S., Pinnau, I., Reinhard, M., Gas and liquid permeation properties of modified interfacial composite reverse osmosis membranes, Journal of Membrane Science 325(2) (2008) 793-800.

Mai, Y., Eisenberg, A., Self-assembly of block copolymers, Chemical Society Reviews 41(18) (2012) 5969-5985.

Majumder, M., Chopra, N., Andrews, R., Hinds, B.J., Enhanced flow in carbon nanotubes, Nature 438(7064) (2005) 44-44.

Marchetti, P., Jimenez Solomon, M.F., Szekely, G., Livingston, A.G., Molecular Separation with Organic Solvent Nanofiltration: A Critical Review, Chemical Reviews 114(21) (2014) 10735-10806.

Martyna, G.J., Tobias, D.J., Klein, M.L., Constant pressure molecular dynamics algorithms, Journal of Chemical Physics 101(5) (1994) 4177-4189.

Mills, R., Self-diffusion in normal and heavy water in the range 1-45.deg, The Journal of Physical Chemistry 77(5) (1973) 685-688.

Miyamoto, S., Kollman, P.A., Settle: An analytical version of the SHAKE and RATTLE algorithm for rigid water models, Journal of Computational Chemistry 13(8) (1992) 952-962.

Mo, Y., Zhao, X., Shen, Y.-x., Cation-dependent structural instability of graphene oxide membranes and its effect on membrane separation performance, Desalination 399 (2016) 40-46.

Mohammadi, A.T., Matsuura, T., Sourirajan, S., Gas separation by silicone-coated dry asymmetric aromatic polyamide membranes, Gas Separation & Purification 9(3) (1995) 181-187.

Murata, K., Mitsuoka, K., Hirai, T., Walz, T., Agre, P., Heymann, J.B., Engel, A., Fujiyoshi, Y., Structural determinants of water permeation through aquaporin-1, Nature 407(6804) (2000) 599-605.

Najem, J.S., Taylor, G.J., Weiss, R.J., Hasan, M.S., Rose, G., Schuman, C.D., Belianinov, A., Collier, C.P., Sarles, S.A., Memristive Ion Channel-Doped Biomembranes as Synaptic Mimics, ACS Nano 12(5) (2018) 4702-4711.

Nguyen, Q.T., Neel, J., Characterization of ultrafiltration membranes.: Part IV. Influence of the deformation of macromolecular solutes on the transport through ultrafiltration membranes, Journal of Membrane Science 14(2) (1983) 111-127.

Ohshima, H., Ohki, S., Donnan potential and surface potential of a charged membrane, Biophysical journal 47(5) (1985) 673-678.

Park, H.B., Kamcev, J., Robeson, L.M., Elimelech, M., Freeman, B.D., Maximizing the right stuff: The trade-off between membrane permeability and selectivity, Science 356(6343) (2017).

Park, J., Yoon, H.W., Paul, D.R., Freeman, B.D., Gas transport properties of PDMS-coated reverse osmosis membranes, Journal of Membrane Science 604 (2020) 118009.

Percec, V., Dulcey, A.E., Balagurusamy, V.S.K., Miura, Y., Smidrkal, J., Peterca, M., Nummelin, S., Edlund, U., Hudson, S.D., Heiney, P.A., Duan, H., Magonov, S.N., Vinogradov, S.A., Self-assembly of amphiphilic dendritic dipeptides into helical pores, Nature 430(7001) (2004) 764-768.

Petrov, E.P., Schwille, P., Translational Diffusion in Lipid Membranes beyond the Saffman-Delbrück Approximation, Biophysical journal 94(5) (2008) L41-L43.

Petrov, Eugene P., Schwille, P., Correction, Biophysical journal 103(2) (2012) 375.

Phillips, J.C., Braun, R., Wang, W., Gumbart, J., Tajkhorshid, E., Villa, E., Chipot, C., Skeel, R.D., Kale, L., Schulten, K., Scalable molecular dynamics with NAMD, Journal of Computational Chemistry 26(16) (2005) 1781-1802.

Pohl, P., Saparov, S.M., Borgnia, M.J., Agre, P., Highly selective water channel activity measured by voltage clamp: Analysis of planar lipid bilayers reconstituted with purified AqpZ, Proceedings of the National Academy of Sciences, USA 98(17) (2001) 9624-9629.

Qian, Q., Asinger, P.A., Lee, M.J., Han, G., Mizrahi Rodriguez, K., Lin, S., Benedetti, F.M., Wu, A.X., Chi, W.S., Smith, Z.P., MOF-Based Membranes for Gas Separations, Chemical Reviews 120(16) (2020) 8161-8266.

Rajesh, S., Yan, Y., Chang, H.-C., Gao, H., Phillip, W.A., Mixed Mosaic Membranes Prepared by Layer-by-Layer Assembly for Ionic Separations, ACS Nano 8(12) (2014) 12338-12345.

Rakhmatullina, E., Meier, W., Solid-Supported Block Copolymer Membranes through Interfacial Adsorption of Charged Block Copolymer Vesicles, Langmuir 24(12) (2008) 6254-6261.

Rathee, V.S., Qu, S., Phillip, W.A., Whitmer, J.K., A coarse-grained thermodynamic model for the predictive engineering of valence-selective membranes, Molecular Systems Design & Engineering 1(3) (2016) 301-312.

Ren, C., Zeng, F., Shen, J., Chen, F., Roy, A., Zhou, S., Ren, H., Zeng, H., Pore-Forming Monopeptides as Exceptionally Active Anion Channels, Journal of the American Chemical Society 140(28) (2018) 8817-8826.

Robeson, L.M., The upper bound revisited, Journal of Membrane Science 320(1) (2008) 390-400.

Roe, D.R., Cheatham, T.E., III, PTRAJ and CPPTRAJ: Software for Processing and Analysis of Molecular Dynamics Trajectory Data, Journal of Chemical Theory and Computation 9(7) (2013) 3084-3095.

Rohani, R., Hyland, M., Patterson, D., A refined one-filtration method for aqueous based nanofiltration and ultrafiltration membrane molecular weight cut-off determination using polyethylene glycols, Journal of Membrane Science 382(1) (2011) 278-290.

Saffman, P.G., Delbrück, M., Brownian motion in biological membranes, Proceedings of the National Academy of Sciences, USA 72(8) (1975) 3111-3113.

Saparov, S.M., Pfeifer, J.R., Al-Momani, L., Portella, G., de Groot, B.L., Koert, U., Pohl, P., Mobility of a One-Dimensional Confined File of Water Molecules as a Function of File Length, Physical Review Letters 96(14) (2006) 148101.

Schaep, J., Van der Bruggen, B., Vandecasteele, C., Wilms, D., Influence of ion size and charge in nanofiltration, Separation and Purification Technology 14(1) (1998) 155-162.

Schneider, S., Licsandru, E.-D., Kocsis, I., Gilles, A., Dumitru, F., Moulin, E., Tan, J., Lehn, J.-M., Giuseppone, N., Barboiu, M., Columnar Self-Assemblies of Triarylamines as Scaffolds for Artificial Biomimetic Channels for Ion and for Water Transport, Journal of the American Chemical Society 139(10) (2017) 3721-3727.

Scholes, C.A., Jin, J., Stevens, G.W., Kentish, S.E., Competitive permeation of gas and water vapour in high free volume polymeric membranes, Journal of Polymer Science Part B: Polymer Physics 53(10) (2015) 719-728.

Scholes, C.A., Jin, J., Stevens, G.W., Kentish, S.E., Hydrocarbon solubility, permeability, and competitive sorption effects in polymer of intrinsic microporosity (PIM-1) membranes, Journal of Polymer Science Part B: Polymer Physics 54(3) (2016) 397-404.

Secchi, E., Marbach, S., Niguès, A., Stein, D., Siria, A., Bocquet, L., Massive radius-dependent flow slippage in carbon nanotubes, Nature 537(7619) (2016) 210-213.

Shen, Y.-x., Saboe, P.O., Sines, I.T., Erbakan, M., Kumar, M., Biomimetic membranes: A review, Journal of Membrane Science 454 (2014) 359-381.

Shen, Y.-x., Si, W., Erbakan, M., Decker, K., De Zorzi, R., Saboe, P.O., Kang, Y.J., Majd, S., Butler, P.J., Walz, T., Aksimentiev, A., Hou, J.-l., Kumar, M., Highly permeable artificial water channels that can self-assemble into two-dimensional arrays, Proceedings of the National Academy of Sciences, USA 112(32) (2015) 9810-9815.

Shen, Y.-x., Song, W., Barden, D.R., Ren, T., Lang, C., Feroz, H., Henderson, C.B., Saboe, P.O., Tsai, D., Yan, H., Butler, P.J., Bazan, G.C., Phillip, W.A., Hickey, R.J., Cremer, P.S., Vashisth, H., Kumar, M., Achieving high permeability and enhanced selectivity for Angstrom-scale separations using artificial water channel membranes, Nature Communications 9(1) (2018) 2294.

Sholl, D.S., Lively, R.P., Seven chemical separations to change the world, Nature 532 (2016) 435-437.

Si, W., Chen, L., Hu, X.-B., Tang, G., Chen, Z., Hou, J.-L., Li, Z.-T., Selective Artificial Transmembrane Channels for Protons by Formation of Water Wires, Angewandte Chemie International Edition 50(52) (2011) 12564-12568.

Si, W., Hu, X.-B., Liu, X.-H., Fan, R., Chen, Z., Weng, L., Hou, J.-L., Self-assembly and proton conductance of organic nanotubes from pillar[5]arenes, Tetrahedron Letters 52(19) (2011) 2484-2487.

Sindhikara, D.J., Kim, S., Voter, A.F., Roitberg, A.E., Bad seeds sprout perilous dynamics: Stochastic thermostat induced trajectory synchronization in biomolecules, Journal of Chemical Theory and Computation 5(6) (2009) 1624-1631.

Singh, A., Koros, W.J., Significance of Entropic Selectivity for Advanced Gas Separation Membranes, Industrial & Engineering Chemistry Research 35(4) (1996) 1231-1234.

Song, W., Joshi, H., Chowdhury, R., Najem, J.S., Shen, Y.-x., Lang, C., Henderson, C.B., Tu, Y.-M., Farell, M., Pitz, M.E., Maranas, C.D., Cremer, P.S., Hickey, R.J., Sarles, S.A., Hou, J.-l., Aksimentiev, A., Kumar, M., Artificial water channels enable fast and selective water permeation through water-wire networks, Nature Nanotechnology 15(1) (2020) 73-79.

Song, W., Kumar, M., Artificial water channels: toward and beyond desalination, Current Opinion in Chemical Engineering 25 (2019) 9-17.

Song, W., Lang, C., Shen, Y.-x., Kumar, M., Design Considerations for Artificial Water Channel–Based Membranes, Annual Review of Materials Research 48(1) (2018) 57-82.

Song, W., Shen, Y.-x., Lang, C., Saha, P., Zenyuk, Iryna V., Hickey, R.J., Kumar, M., Unique selectivity trends of highly permeable PAP[5] water channel membranes, Faraday Discussions 209(0) (2018) 193-204.

Song, W., Tu, Y.-M., Oh, H., Samineni, L., Kumar, M., Hierarchical Optimization of High-Performance Biomimetic and Bioinspired Membranes, Langmuir 35(3) (2019) 589-607.

Sridhar, S., Smitha, B., Mayor, S., Prathab, B., Aminabhavi, T.M., Gas permeation properties of polyamide membrane prepared by interfacial polymerization, Journal of Materials Science 42(22) (2007) 9392-9401.

Sui, H., Han, B.-G., Lee, J.K., Walian, P., Jap, B.K., Structural basis of water-specific transport through the AQP1 water channel, Nature 414 (2001) 872.

Tajkhorshid, E., Nollert, P., Jensen, M.Ø., Miercke, L.J.W., O'Connell, J., Stroud, R.M., Schulten, K., Control of the Selectivity of the Aquaporin Water Channel Family by Global Orientational Tuning, Science 296(5567) (2002) 525-530.

Tan, Z., Chen, S., Peng, X., Zhang, L., Gao, C., Polyamide membranes with nanoscale Turing structures for water purification, Science 360(6388) (2018) 518-521.

Tang, H., Ji, S., Gong, L., Guo, H., Zhang, G., Tubular ceramic-based multilayer separation membranes using spray layer-by-layer assembly, Polymer Chemistry 4(23) (2013) 5621-5628.

Taylor, G.J., Venkatesan, G.A., Collier, C.P., Sarles, S.A., Direct in situ measurement of specific capacitance, monolayer tension, and bilayer tension in a droplet interface bilayer, Soft Matter 11(38) (2015) 7592-7605.

Thornton, A.W., Freeman, B.D., Polymer Gas Separation Membrane Database. http://membrane-australasia.org/.

Tong, J., Canty, J.T., Briggs, M.M., McIntosh, T.J., The water permeability of lens aquaporin-0 depends on its lipid bilayer environment, Experimental Eye Research 113 (2013) 32-40.

Toyoshima, Y., Thompson, T.E., Chloride flux in bilayer membranes. Chloride permeability in aqueous dispersions of single-walled, bilayer vesicles, Biochemistry 14(7) (1975) 1525-1531.

Tunuguntla, R.H., Henley, R.Y., Yao, Y.-C., Pham, T.A., Wanunu, M., Noy, A., Enhanced water permeability and tunable ion selectivity in subnanometer carbon nanotube porins, Science 357(6353) (2017) 792-796.

Vanommeslaeghe, K., Hatcher, E., Acharya, C., Kundu, S., Zhong, S., Shim, J., Darian, E., Guvench, O., Lopes, P., Vorobyov, I., CHARMM general force field: A force field for drug-like molecules compatible with the CHARMM all-atom additive biological force fields, Journal of Computational Chemistry 31(4) (2010) 671-690.

Verkman, A.S., Development and biological applications of chloride-sensitive fluorescent indicators, American Journal of Physiology-Cell Physiology 259(3) (1990) C375-C388.

Villalobos, L.F., Huang, T., Peinemann, K.-V., Cyclodextrin Films with Fast Solvent Transport and Shape-Selective Permeability, Advanced Materials 29(26) (2017) 1606641.

Werber, J.R., Elimelech, M., Permselectivity limits of biomimetic desalination membranes, Science Advances 4(6) (2018) eaar8266.

White, L.S., Blinka, T.A., Kloczewski, H.A., Wang, I.f., Properties of a polyimide gas separation membrane in natural gas streams, Journal of Membrane Science 103(1) (1995) 73-82.

Woodle, M.C., Papahadjopoulos, D., [9] Liposome preparation and size characterization, Methods in Enzymology, Academic Press1989, pp. 193-217.

Xie, W., Geise, G.M., Freeman, B.D., Lee, H.-S., Byun, G., McGrath, J.E., Polyamide interfacial composite membranes prepared from m-phenylene diamine, trimesoyl chloride and a new disulfonated diamine, Journal of Membrane Science 403-404 (2012) 152-161.

Xu, L., Shahid, S., Shen, J., Emanuelsson, E.A.C., Patterson, D.A., A wide range and high resolution one-filtration molecular weight cut-off method for aqueous based nanofiltration and ultrafiltration membranes, Journal of Membrane Science 525 (2017) 304-311.

Xue, M., Yang, Y., Chi, X., Zhang, Z., Huang, F., Pillararenes, A New Class of Macrocycles for Supramolecular Chemistry, Accounts of Chemical Research 45(8) (2012) 1294-1308.

Yoo, J., Aksimentiev, A., Improved parametrization of Li+, Na+, K+, and Mg2+ ions for all-atom molecular dynamics simulations of nucleic acid systems, Journal of Physical Chemistry Letters 3(1) (2012) 45-50.

Yoo, J., Aksimentiev, A., Improved parameterization of amine–carboxylate and amine–phosphate interactions for molecular dynamics simulations using the CHARMM and AMBER force fields, Journal of Chemical Theory and Computation 12(1) (2015) 430-443.

Yoo, J., Aksimentiev, A., Refined Parameterization of Nonbonded Interactions Improves Conformational Sampling and Kinetics of Protein Folding Simulations, Journal of Physical Chemistry Letters 7(19) (2016) 3812-3818.

Yoo, J., Aksimentiev, A., New tricks for old dogs: improving the accuracy of biomolecular force fields by pair-specific corrections to non-bonded interactions, Physical Chemistry Chemical Physics 20(13) (2018) 8432-8449.

Zhao, H., Ong, W.Q., Fang, X., Zhou, F., Hii, M.N., Li, S.F.Y., Su, H., Zeng, H., Synthesis, structural investigation and computational modelling of water-binding aquafoldamers, Organic & Biomolecular Chemistry 10(6) (2012) 1172-1180.

Zhao, H., Sheng, S., Hong, Y., Zeng, H., Proton Gradient-Induced Water Transport Mediated by Water Wires Inside Narrow Aquapores of Aquafoldamer Molecules, Journal of the American Chemical Society 136(40) (2014) 14270-14276.

Zhao, Q., Liu, Y., Macrocycle crosslinked mesoporous polymers for ultrafast separation of organic dyes, Chemical Communications 54(53) (2018) 7362-7365.

Zhao, X., Bu, X., Wu, T., Zheng, S.-T., Wang, L., Feng, P., Selective anion exchange with nanogated isoreticular positive metal-organic frameworks, Nature Communications 4(1) (2013) 2344.

Zhou, X., Liu, G., Yamato, K., Shen, Y., Cheng, R., Wei, X., Bai, W., Gao, Y., Li, H., Liu, Y., Liu, F., Czajkowsky, D.M., Wang, J., Dabney, M.J., Cai, Z., Hu, J., Bright, F.V., He, L., Zeng, X.C., Shao, Z., Gong, B., Self-assembling subnanometer pores with unusual mass-transport properties, Nature Communications 3(1) (2012) 949.

Zhu, F., Tajkhorshid, E., Schulten, K., Collective Diffusion Model for Water Permeation through Microscopic Channels, Physical Review Letters 93(22) (2004) 224501.

Zydney, A.L., Stagnant film model for concentration polarization in membrane systems, Journal of Membrane Science 130(1) (1997) 275-281.